QUANTITATIVE IMAGING OF GOLD NANOPARTICLE DISTRIBUTION FOR PRECLINICAL STUDIES OF GOLD NANOPARTICLE-AIDED RADIATION THERAPY

A Dissertation
Presented to
The Academic Faculty

by

Nivedh H. Manohar

In Partial Fulfillment
of the Requirements for the Degree
Doctor of Philosophy in Nuclear Engineering in the
George W. Woodruff School of Mechanical Engineering

Georgia Institute of Technology

May 2015

QUANTITATIVE IMAGING OF GOLD NANOPARTICLE DISTRIBUTION FOR PRECLINICAL STUDIES OF GOLD NANOPARTICLE-AIDED RADIATION THERAPY

Approved by:

Dr. Sang Hyun Cho, Advisor
School of Mechanical Engineering,
NRE/MP Department
Georgia Institute of Technology

Dr. C.-K. Chris Wang, Co-Advisor
School of Mechanical Engineering,
NRE/MP Department
Georgia Institute of Technology

Dr. Eric S. Elder
Department of Radiation Oncology
Emory University School of Medicine

Dr. Chaitanya S. Deo
School of Mechanical Engineering,
NRE/MP Department
Georgia Institute of Technology

Dr. John N. Oshinski
School of Biomedical Engineering
Georgia Institute of Technology

Date Approved: March 27, 2015

ACKNOWLEDGEMENTS

I would like to extend my deepest gratitude to my advisor, Dr. Sang Hyun Cho, for the past seven years of mentorship, ever since graciously allowing me to join his research group during my undergraduate studies. He has been instrumental in shaping my intellectual development and the path of my professional career via abundant opportunities. I am indebted to all of the previous members of the lab group, especially Dr. Seong-Kyun Cheong and Dr. Bernard “Tripp” Jones, for their hard work and expertise. A special acknowledgement goes to Dr. Francisco Reynoso for his friendship and for always challenging and holding me to the highest standard. His rigorous analysis and thought-provoking critique were essential for many of the achievements in this work. I am very appreciative of my co-advisor, Dr. C.-K. Chris Wang, and the members of my reading committee, Dr. Eric S. Elder, Dr. Chaitanya S. Deo, and Dr. John N. Oshinski for sharing their knowledge and experience and for volunteering their time and suggestions.

The constant encouragement, reassurance, and affection from the soon-to-be Dr. Jenny Lin, as well as her intelligence and work ethic, were immeasurably inspirational. In conjunction, the frequent interrogation from my sister, Nishrutha Manohar, regarding my lengthy tenure in college provided the motivation needed to complete this work. Last but not least, I owe it all to my mother, Rajalakshmi Ramachandran, and my father, Dr. Rajappa Manohar, for their all of their sacrifices, enduring love, support, and especially for instilling in me from an early age an insatiable curiosity and wonder towards science.

Investigations were supported in part by National Institutes of Health (NIH) / National Cancer Institute (NCI) Grant No. R01CA155446 and the National Science Foundation (NSF) Graduate Research Fellowship DGE-1148903.

TABLE OF CONTENTS

LIST OF TABLES

LIST OF FIGURES

LIST OF ABBREVIATIONS

2D	Two-dimensional
3D	Three-dimensional
CSDA	Continuous slowing down approximation
CT	Computed tomography
DPK	Dose-point kernel
EGS	Electron gamma shower
FNST	Fluorescence-normalized scan time
FSDR	Fluorescence signal-to-dose ratio
FWHM	Full width at half maximum
Geant4	Geometry and tracking toolkit, version 4
GNP	Gold nanoparticle
GNR	Gold nanorod
GNRT	Gold nanoparticle-aided radiation therapy
HOPG	Highly-ordered pyrolytic graphite
MATLAB	Matrix Laboratory
MC	Monte Carlo
MCNP5	Monte Carlo N-Particle code, version 5
nDEF	Nanoscopic dose enhancement factor
NOREC	New Oak Ridge electron transport code
PMMA	Polymethyl methacrylate
ppm	Parts-per-million
ROI	Region of interest
SDD	Silicon drift detector
TEM	Transmission electron microscopy
WNP	Water nanoparticle
XFCT	X-ray fluorescence computed tomography
XRF	X-ray fluorescence

LIST OF SYMBOLS

%	Percentage
σ_b	Noise of background
τ	Photoelectric cross section
°	Degree
µg	Microgram
µm	Micrometer
a.u.	Arbitrary units
Al	Aluminum
Be	Beryllium
CdTe	Cadmium-telluride
cm	Centimeter
cm^3	Cubic centimeter
E	Energy
eV	Electronvolt
keV	Kiloelectronvolt
kVp	Peak kilovoltage
kW	Kilowatt
mA	Milliampere
MeV	Megaelectronvolt
mg	Milligram
mm	Millimeter
MV	Megavoltage
nm	Nanometer
Pb	Lead
r	Pearson product-moment correlation coefficient
s	Second
Si	Silicon

Sn	Tin
wt. %	Weight percentage
Yb	Ytterbium
Z	Atomic number

SUMMARY

Gold nanoparticles (GNPs) have recently attracted considerable interest for use in radiation therapy due to their unique physical and biological properties. Of interest, GNPs (and other high-atomic-number materials) have been used to enhance radiation dose in tumors by taking advantage of increased photoelectric absorption. This physical phenomenon is well-understood on a macroscopic scale. However, biological outcomes often depend on the intratumoral and even intracellular distribution of GNPs, among other factors. Therefore, there exists a need to precisely visualize and accurately quantify GNP distributions. By virtue of the photoelectric effect, x-ray fluorescence (XRF) photons (characteristic x-rays) from gold can be induced and detected, not only allowing the distribution of GNPs within biological samples to be determined but also providing a unique molecular imaging option in conjunction with bioconjugated GNPs. This work proposes the use of this imaging modality, known as XRF imaging, to develop experimental imaging techniques for detecting and quantifying sparse distributions of GNPs in preclinical settings, such as within small-animal-sized objects, tissue samples, and superficial tumors. By imaging realistic GNP distributions, computational methods can then be used to understand radiation dose enhancement on an intratumoral scale and perhaps even down to the nanoscopic, subcellular realm, elucidating observed biological outcomes (e.g., radiosensitization of tumors) from the bottom-up. Ultimately, this work will result in experimental and computational tools for developing a better understanding of GNP-mediated dose enhancement and associated radiosensitization within the scope of GNP-aided radiation therapy.

CHAPTER 1
INTRODUCTION

1.1 Relevant Applications of the Photoelectric Effect

Considering all the mechanisms by which photons can interact with matter, the photoelectric effect is arguably one of the most important physical phenomena in the fields of photon-based imaging and therapy. The probability of a photon interacting via the photoelectric effect (τ) is a function of the atomic number (Z) of the interacting material and the energy (E) of the photon: it is, on average, proportional to Z^3/E^3.

This differential attenuation for various materials is the basis for radiography and its derivatives such as computed tomography (CT). A closer look at the photoelectric effect and its quantum mechanical nature elucidates the basis for another imaging modality. When an atom undergoes the photoelectric effect, the energy from an incident photon is transferred to an atomic electron. The electron is ejected with kinetic energy equal to the difference between the incident photon energy and the binding energy of the electron. In the case that an inner-shell electron is ejected, the vacancy will be filled by another orbital electron. This transition between quantized energy levels releases energy in the form of x-rays. Therefore, for a given element, these x-rays have a characteristic energy; hence, these x-rays are aptly named “characteristic x-rays” and are also known as fluorescence x-rays. Typically, the transitions of electrons to the innermost orbital (*K*-shell) and the next orbital (*L*-shell) result in the highest fluorescence yield. By detecting x-ray fluorescence (XRF), the amount and distribution of individual elements within objects can be imaged. This method, known as XRF analysis, has a long history in the physical sciences. It is a well-established non-destructive quantitative elemental analysis technique that has the ability to accurately probe most heavy elements. This methodology was first used in medicine in the 1950s and 1960s for elemental analysis in animal bones and a variety of biological tissues [1-3].

The photoelectric effect has benefits for radiotherapy as well. Due to the fact that high-*Z* materials absorb photons more efficiently and produce large numbers of secondary electrons (which are ultimately responsible for energy deposition), tumors can be infused with high-*Z* materials to preferentially increase the energy delivered (dose) during radiotherapy [4-7].

1.2 Gold Nanoparticles and Radiation Dose Enhancement

One such high-*Z* element of interest is gold, especially in the form of gold nanoparticles (GNPs). GNPs are particularly well-suited for use in imaging and therapy, not only because of the high atomic number of gold (Z=79) but also due to their biological compatibility and high tumor specificity (both passively, via extravasation by virtue of the enhanced permeability and retention effect, and actively, using conjugation with antibodies against tumor-specific biomarkers) [8-12]. An approach known as gold nanoparticle-aided radiation therapy (GNRT) [13] is a very promising new modality for use in cancer treatment because it has the ability to concentrate the radiation dose where needed and thereby radiosensitizes the tumor, while sparing normal tissues from receiving unnecessary dose [14, 15]. Some studies have indicated that, macroscopically, the tumor dose from x-rays can be enhanced by a factor of at least two and even more during GNRT treatments, depending on the concentration of gold within tumors and the energy spectra of photon sources used [16]. Curiously, however, there is poor correlation between macroscopic dose enhancement and biological outcomes.

1.3 Imaging of Gold Nanoparticles

It is believed that the spatial distribution and amount of radiosensitizers (e.g., GNPs or other high-*Z* materials) on intratumoral, and possibly even subcellular and nanoscale realms, is responsible for this disparity between macroscopic dose enhancement and biological outcomes. This can potentially be reconciled by high-resolution imaging in addition to understanding the dose enhancement patterns on such small scales. In this context, GNPs can be used as unique molecular imaging agents by inducing and detecting the XRF photons from gold. The sensitivity and specificity allowed by XRF analysis has recently allowed its use for *in vivo* quantification of elements such as lead (Pb) [17] and iron [18] using *L*-shell XRF photons and also of iodine [19] using *K*-shell XRF photons, with detection limits typically on the order of parts-per-million (ppm) when using a synchrotron as the excitation source.

1.4 Overview of the Research

This dissertation describes the development of techniques for XRF imaging of GNPs for preclinical GNRT studies using two fundamentally distinct methods: detection of *K*-shell XRF photons from gold (~67.0 and ~68.8 keV) and detection of *L*-shell XRF photons from gold (~9.71 and ~11.4 keV). Owing to higher photon energy and consequently, better penetration depth of the XRF photons, the *K*-shell method is better suited for imaging of larger objects and can be used for two-dimensional (2D) or three-dimensional (3D) tomographic reconstruction while the *L*-shell method is useful for direct 2D imaging of small samples. Concurrently, computational models for dose enhancement were developed to elucidate the nanoscopic dose enhancement characteristics around realistically-sized GNPs. These models can be applied to intratumoral (or even more detailed) GNP distributions gleaned from XRF-based and other imaging techniques to estimate dose enhancement on small scales and potentially explain the effects of GNP-mediated radiosensitization from a physical point-of-view.

1.4.1 X-ray Fluorescence Computed Tomography

In recent years, a traditionally synchrotron-based technique known as x-ray fluorescence computed tomography (XFCT) [20-27] has emerged as a valuable quantitative imaging tool which can be used to determine the biodistribution of high-*Z* elements such as iodine, gadolinium, platinum, and gold. While monochromatic x-rays are considered ideal [28] for XFCT, the impracticality of using synchrotrons in typical biomedical laboratory settings, especially for *in vivo* imaging of small animals, has motivated the implementation of XFCT on a benchtop setting using a polychromatic diagnostic energy-range x-ray source (*viz.*, “benchtop XFCT”). Through a series of studies [29-31], it has been shown that benchtop XFCT is capable of localizing GNPs inside small-animal-sized objects by detecting *K*-shell XRF photons from gold. Especially, in a recent experimental study [31], the capability of performing benchtop

XFCT of GNP-loaded objects using polychromatic cone-beams has been demonstrated, paving the way to build a practical benchtop XFCT system. Additionally, other researchers have applied similar techniques to image various other metal probes (e.g., platinum) within small-animal-sized phantoms [32-34], suggesting the possibility of extending benchtop XFCT techniques beyond GNP applications. Following up on the studies mentioned, research efforts are currently underway to build a benchtop XFCT system for routine pre-clinical *in vivo* imaging with GNPs and/or other high-Z metal/non-metal probes. These efforts require further development and optimization of the existing experimental setup, especially in terms of maximizing the production/detection of gold XRF photons under the given physical limitations. While it could be done entirely by an experimental approach, Monte Carlo (MC) methods are particularly well-suited for simulating spectroscopic XRF imaging [35], capable of producing accurate results even with polychromatic x-ray spectra and heterogeneous geometries [36], and would be useful for streamlining further optimization efforts. For example, a well-validated computational model of the experimental XFCT setup would enable proper tailoring (or quasi-monochromatization) of the incident polychromatic x-ray spectrum, one of the major challenges associated with benchtop XFCT, in a much more efficient manner [37]. Also, it could be applied to various optimization tasks ranging from source/detector collimator design to overall benchtop XFCT system configuration. Several computational investigations of the prototype XFCT system and subsequent experimental work are reported in Chapter 2.

1.4.2 Direct X-ray Fluorescence Imaging

While most of the recent investigations on non-synchrotron XFCT [29-34] based on gold focus on utilizing the higher energy *K*-shell XRF, there is still a chance to perform either XFCT or direct XRF imaging of biological samples with the lower energy *L*-shell XRF photons. Despite their short penetration depth in water/tissue (e.g., ~0.2 cm of mean free path at these energies), these photons can still be detected after traversing several mean free paths and can be used for XRF imaging. Although its utility is limited to fairly "small" biological samples (< ~1 cm in diameter or thickness), *L*-shell XRF-based imaging technique, compared to its *K*-shell counterpart, offers some distinct merits in many aspects, especially in terms of improving the image resolution and the detection limit. For example, *L*-shell XRF photons from GNPs are easily produced in abundance using a relatively low power/tube voltage (e.g., less than 100 W and 30-70 kVp) source. Once produced, they can be detected with almost 100% efficiency using readily-available semiconductor detectors. Moreover, the scatter background for *L*-shell XRF photon signal is typically much lower than that for *K*-shell XRF signal. Consequently, as demonstrated in recent studies [38, 39], GNPs presented within small samples on the order of ppm can be detected with *L*-shell XRF analysis in conjunction with benchtop polychromatic x-ray sources. This is in sharp contrast to using *K*-shell XRF photons from GNPs for quantification, which has resulted in a significantly inferior detection limit than the approaches using *L*-shell XRF photons by as much as two orders of magnitude [31, 40]. In contrast to *K*-shell XFCT, imaging based on *L*-shell XRF would be more suited to direct imaging (2D planar imaging), rather than tomography, of small objects due to the lower energy of *L*-shell XRF photons. Its utility would be found in imaging small biological samples such as *ex vivo* tissues and, potentially, superficial tumors with higher resolution and more sensitivity than *K*-shell-based imaging. In Chapter 3, the development of an experimental *L*-shell XRF detection system capable of direct 2D imaging of GNPs and the re-configuration of the system for use with a high-power x-ray source are detailed.

1.4.3 Nanoscopic Dose Enhancement around GNPs

Conventional radiation dose response schemes fail when applied to GNRT considering nanoscale effects and therefore, it is important to characterize how exactly this dose enhancement occurs on such a small scale. By performing this research, a framework can be developed to explain the effects of GNP-mediated radiosensitization from a physical point-of-view. The quantification of nanoscopic dose enhancement could ultimately help explain GNP-mediated radiosensitization when combined with proper biological models. Although the XRF-based imaging methods of GNPs do not currently allow nanoscopic spatial resolution, the dose enhancement around GNPs imaged using other modalities (e.g., electron microscopy) can provide useful information. Chapter 4 describes computational investigations of the nanoscopic dose distribution around GNPs and the application of the results to calculate intracellular dose enhancement using an image of a cell.

CHAPTER 2
MONTE CARLO AND EXPERIMENTAL INVESTIGATIONS OF *K*-SHELL XFCT SYSTEM

2.1 Background and Objective

This work was built upon a previously-developed experimental cone-beam XFCT system that is capable of producing tomographic images of GNPs within small-animal-sized objects [29, 31]. The system featured a compact polychromatic cone-beam x-ray source and cadmium-telluride (CdTe) x-ray detector used to image the amount and spatial distribution of GNPs inside small-animal-sized objects by detecting the *K*-shell XRF photons induced from GNPs.

A low-power (~50 W), tungsten-target microfocus x-ray source (L9631, Hamamatsu Photonics K.K.), operated at 105 kVp and 0.45 mA of current, was used as the excitation source for XFCT. The x-ray beam from the source was collimated using a Pb block, 20 cm in width/height and a thickness in the beam direction of 5 cm. The block featured a conical (11.4º) opening with diameters of 1 cm and 2 cm along the beam direction. Either a 1-mm-thick Pb filter or a 0.9-mm-thick tin (Sn) filter was placed after the collimator to attenuate low energy photons below the *K*-edge of gold (80.7 keV) which are not capable of generating gold *K*-shell XRF photons; essentially, the intention was to shape the incident x-ray spectrum to maximize XRF production while minimizing scattered photons and reducing unwanted dose. Pb and Sn were chosen not only because of their high photoelectric absorption cross sections at energies below the *K*-edge of gold but also because of their ubiquitous availability. The divergence of the beam after the collimator allowed it to cover the entire phantom, a surrogate for a small animal, which was placed 8 cm away.

The phantom was made of polymethyl methacrylate (PMMA), a tissue-equivalent plastic. The irradiated portion of the cylindrical phantom had a diameter and height of 3 cm and was molded on top of a cylindrical base, 4.5 cm in diameter and 2 cm in height. The irradiated portion had three equally spaced, 1.5-cm-deep, 6-mm-diameter holes drilled with their centers located 1 cm from the center of the phantom. Tapered imaging inserts of slightly smaller diameter and height were accommodated by these holes. The inserts could be loaded with saline solution or water, mixed with GNPs at various concentrations, typically below 20 mg/cm^3 (2 wt. %).

A commercially-available, thermoelectrically-cooled CdTe x-ray detector (XR100-T-CdTe, Amptek Inc.) was placed at 90° with respect to the beam direction and 0.75 cm behind a 4-cm-thick Pb pinhole collimator with aperture diameter of 2.5 mm. The 90° detection geometry allowed good avoidance of the primary beam and simplified image reconstruction. Briefly, a combination of phantom rotations and detector translations were utilized to acquire XRF signal data from multiple lines, which were then used for reconstructing an axial XFCT image of the phantom.

2.2 Monte Carlo Model of Experimental XFCT System

An accurate and comprehensive MC model of the experimental benchtop XFCT system was created using the Monte Carlo N-Particle transport code, version 5 (MCNP5) [41]. In this section, the modeling approach of each component will be described. The current MC model (**Figure 2.2.1**) was based on one particular detector position and phantom orientation of the experimental XFCT system in order to facilitate direct comparison with experimental measurements taken under the same conditions.

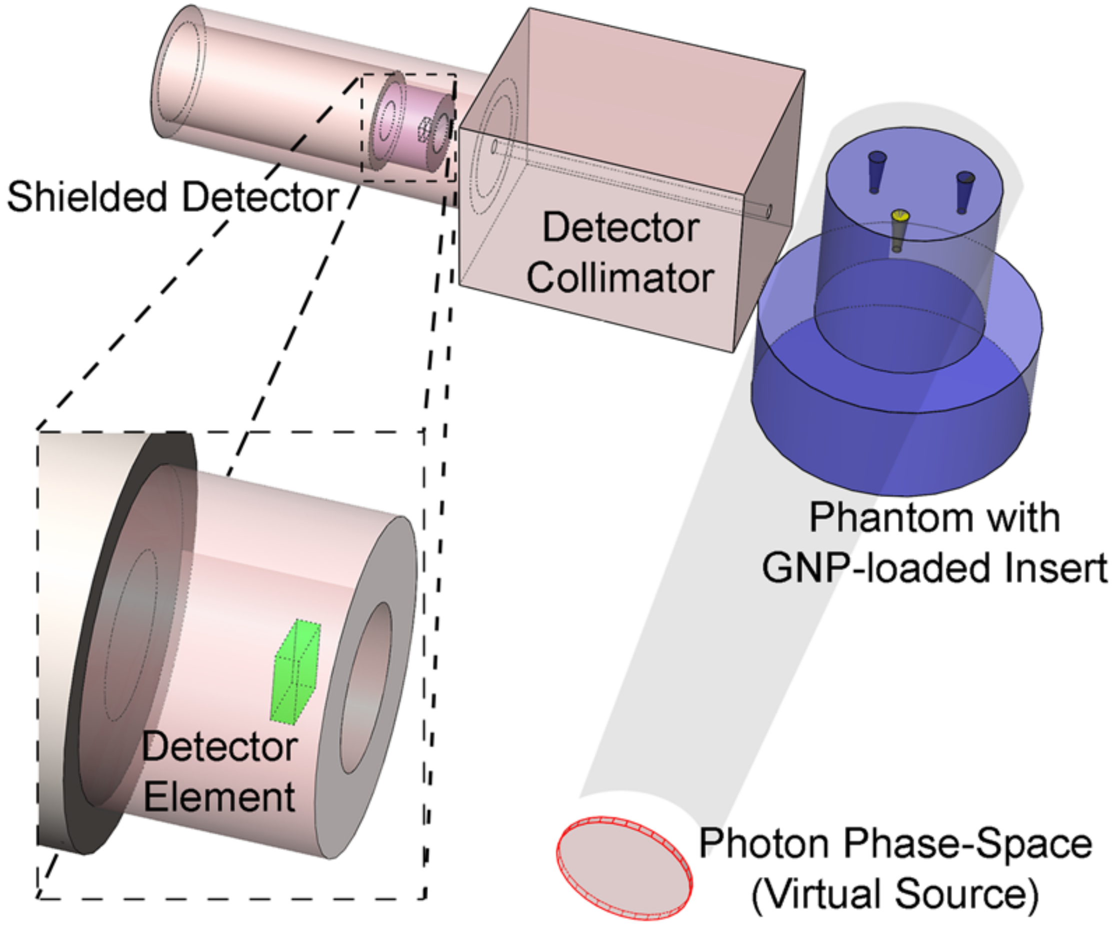

Figure 2.2.1 Components of MC model simulating the experimental *K*-shell XFCT system. The PMMA phantom with GNP-loaded insert was irradiated by a virtual cone-beam source with configurable photon spectra. The XRF and scattered x-rays (at 90° with respect to the incident beam) from the GNP-loaded insert and phantom were collimated and detected by a shielded CdTe detector. Note that the incident beam collimator and filter were replaced by a virtual photon phase-space source. (inset) detail of detector element located inside the detector housing.

2.2.1 X-ray Source, Collimation, and Filtration

Instead of a computationally-inefficient direct modeling of the beam propagation from the x-ray source through the collimator and filter, the current MC model implemented a diverging 2-cm-diameter disk source (i.e., cone-beam source) located immediately after the location of the filter to represent the phase-space of x-rays with the appropriately filtered energy spectrum (**Figure 2.2.2**). This virtual source approach, validated in a previous investigation [42], provided the two following advantages: first, it was possible to perform a straightforward experimental measurement of the x-ray spectra after collimation and filtration of the source x-ray beam, yielding more realistic spectra which could then be used for MC simulations; second, by not having to repeatedly simulate the transport of photons from the x-ray source through the collimator and filter, computational time was shortened dramatically.

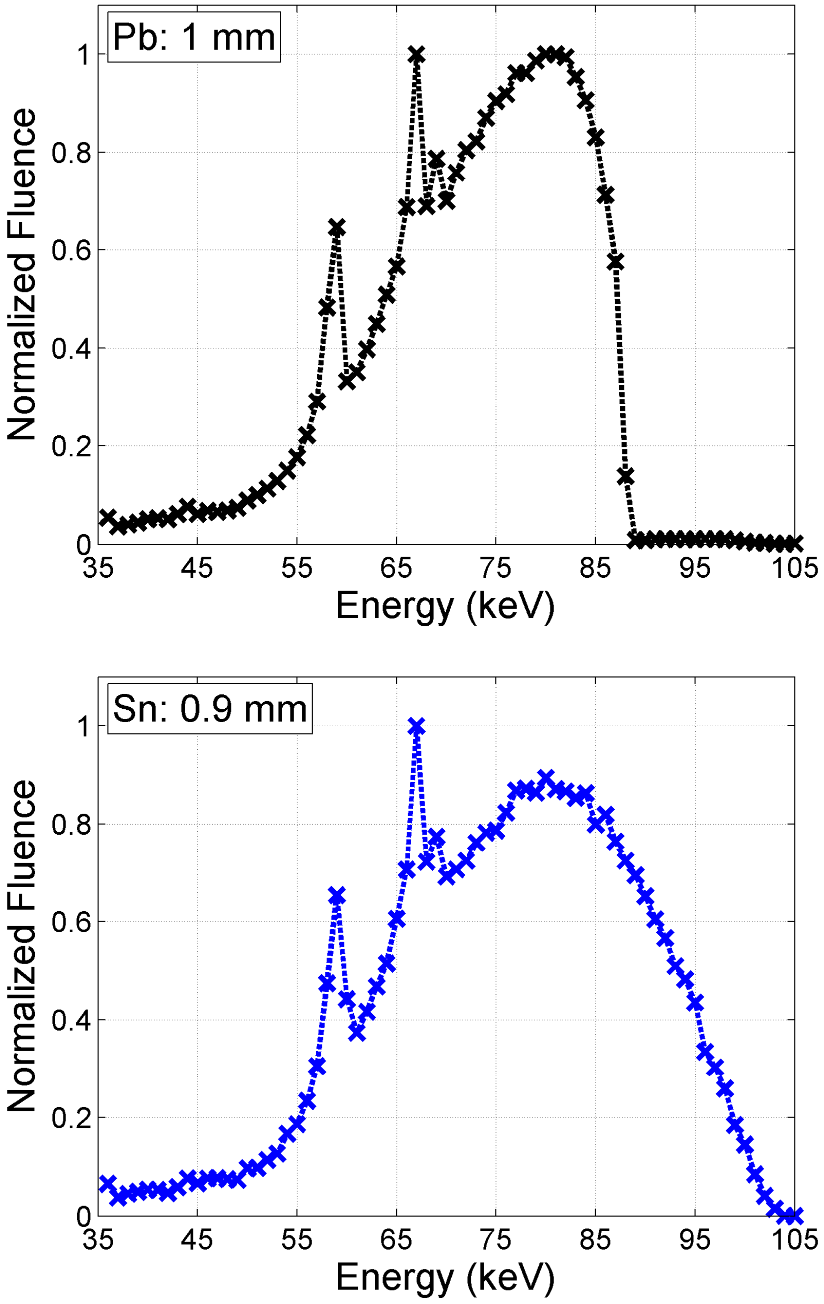

Figure 2.2.2 Experimentally measured x-ray spectra obtained after filtration of 105 kVp x-ray beam using Pb and Sn. (top) 1-mm Pb filter and (bottom) 0.9-mm Sn filter. Fluence has been normalized to aid visual comparison (see **Figure 2.3.1** for relative fluence comparison). These spectra were used as incident spectra in the MC model to generate XRF/scatter spectra, which in turn were compared with measured spectra for validating the model.

2.2.2 Phantom with GNP-Loaded Inserts

The cylindrical PMMA phantom was modeled to the exact specifications described earlier. The phantom was oriented as shown in **Figure 2.2.1** and the insert closest to the x-ray source was modeled as a solution of water and uniformly distributed GNPs at a concentration of 20 mg/cm^3 (2 wt. %) while the other two inserts contained water only.

2.2.3 XRF Detector and Collimation

Relevant components of the x-ray detector were modeled accurately. These included its beryllium (Be) window of 100 μm thickness and 3 mm × 3 mm × 1 mm CdTe crystal serving as the active area of the detector, located 1.27 mm behind the window. The detector housing was also modeled; it was comprised of the head, a 0.25-mm-thick, 1.4-cm-diameter nickel cover, and a 1.5-mm-thick base made of Kovar steel (a nickel-cobalt ferrous alloy). Also, a cylindrical 2-mm-thick Pb shield was placed around the detector housing. The detector collimator was modeled based on the specifications described previously and placed in front of the detector. The whole assembly was located such that the collimator aperture and detector crystal were aligned with the center of the GNP-loaded imaging insert at 90° with respect to the beam direction.

2.2.4 Monte Carlo Simulation Parameters

The MCNP5 input deck was configured to track photons, with an energy-specific flux (F4) tally over the detector crystal to score XRF and scattered photons reaching it

(90° XRF/scatter spectra). Default physics options were used for photon transport, including treatment of bremsstrahlung, coherent scattering, and Doppler broadening. No variance reduction methods, biasing, or forced transport were used in order to avoid skewing the results. The energy-bin width was set to be 0.5 keV in order to discern spectral features such as the gold XRF peaks of interest (i.e., K_{α} peaks at ~67.0 and ~68.8 keV) while still approximating the actual energy resolution of the detector. Although the less-prominent K_{β} peak (~78 keV) was visible in some of the results, it was not considered for analysis due to its lower fluorescence yield. In addition, the average dose to the center of the phantom was scored using an energy-deposition (F6) tally. For each set of simulation corresponding to the testing of one source spectrum, 80×10^9 individual particle histories were run in order to obtain results with average statistical uncertainty below 3%.

2.2.5 Validation of Monte Carlo Model

The MC model first needed to be validated as an accurate representation of the experimental setup so that it could be used as a tool for further, purely computational investigation. Mirroring the experimental setup, the validation was done by using the 1-mm Pb-filtered and 0.9-mm Sn-filtered spectra for the virtual cone-beam source, presented previously in **Figure 2.2.2**. The XRF/scatter spectra from the MCNP5 simulations were compared with experimentally-obtained data under the same conditions. The measured and simulated XRF/scatter spectra are shown in **Figure 2.2.3**.

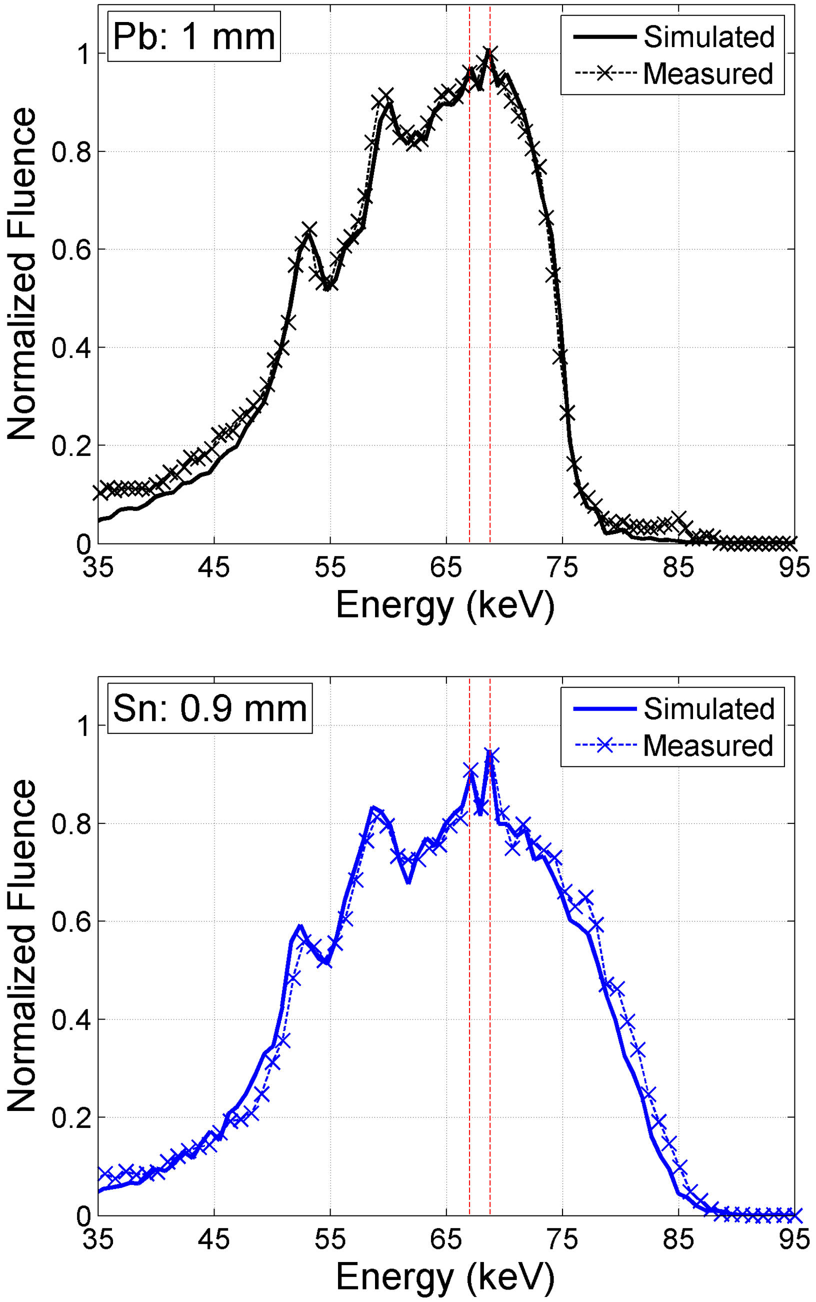

Figure 2.2.3 Comparison between measured and simulated XRF/scatter spectra used for validating the MC model. These spectra resulted from the following incident x-ray spectra: (top) 1-mm Pb-filtered spectrum and (bottom) 0.9-mm Sn-filtered spectrum. The gold XRF peaks of interest (K_α) are located at ~67.0 and ~68.8 keV (vertical dotted red lines). Fluence has been normalized to aid qualitative assessment; linear scale.

The simulated results were validated against experimental measurements by computing their similarity, given by the sample Pearson product-moment correlation coefficient (*r*):

$$r = \frac{1}{n-1}\sum_{i=1}^{n}\left(\frac{M_i - \bar{M}}{\sigma_M}\right)\left(\frac{S_i - \bar{S}}{\sigma_S}\right)$$

where n is the number of energy bins, M_i is the measured fluence in bin i, $\bar{M}$ is the sample mean of the measured fluence, σ_M is the sample standard deviation of the measured fluence. The terms are defined equivalently for *S*, the simulated results. A correlation coefficient value of unity implies a perfect, positive correlation. The *r* value between the simulated and measured XRF/scatter spectra showed excellent agreement for both cases (1-mm Pb-filtered: $r = 0.997$; 0.9-mm Sn-filtered: $r = 0.996$).

2.3 Effects of Incident X-ray Spectra on XRF

After validation, the MC model was utilized to investigate the effects of varying the incident x-ray spectrum to potentially improve production/detection of XRF photons from GNPs. Incident spectra with additional filtration (computationally generated) and hypothetical quasi-monochromatic incident spectra were used for the virtual cone-beam source to generate XRF/scatter spectra for assessing the effects of filter material and thickness on the production/detection of gold XRF photons.

2.3.1 Generation of Additionally-Filtered Incident Spectra

First, the experimentally-measured 1-mm Pb-filtered and 0.9-mm Sn-filtered incident beam spectra were used as input data for the MC model to computationally generate supplementary spectra with additional filtration. Specifically, for each case, a filter of appropriate thickness (Pb: 1 and 2 mm, Sn: 0.1, 1.1, and 2.1 mm) was placed immediately after the virtual cone-beam source, resulting in these spectra (Pb: 2 and 3 mm, Sn: 1, 2, and 3 mm of total filtration). With further filtration, it was important to consider not only the alteration of incident x-ray spectra but also the decrease in overall photon fluence in the incident beam. Thus, investigation was limited to the consideration of relatively thin filters.

Figure 2.3.1 displays, in addition to the measured spectra (1-mm Pb-filtered and 0.9-mm Sn-filtered), the computationally generated spectra from additional filtration: three Sn-filtered spectra (1, 2, and 3 mm) and two Pb-filtered spectra (2 and 3 mm). The overall incident x-ray photon fluence for each case, relative to the 0.9-mm Sn filter, is also shown. As expected, increasing filtration hardened the incident spectra and also exponentially decreased the photon fluence available for irradiation.

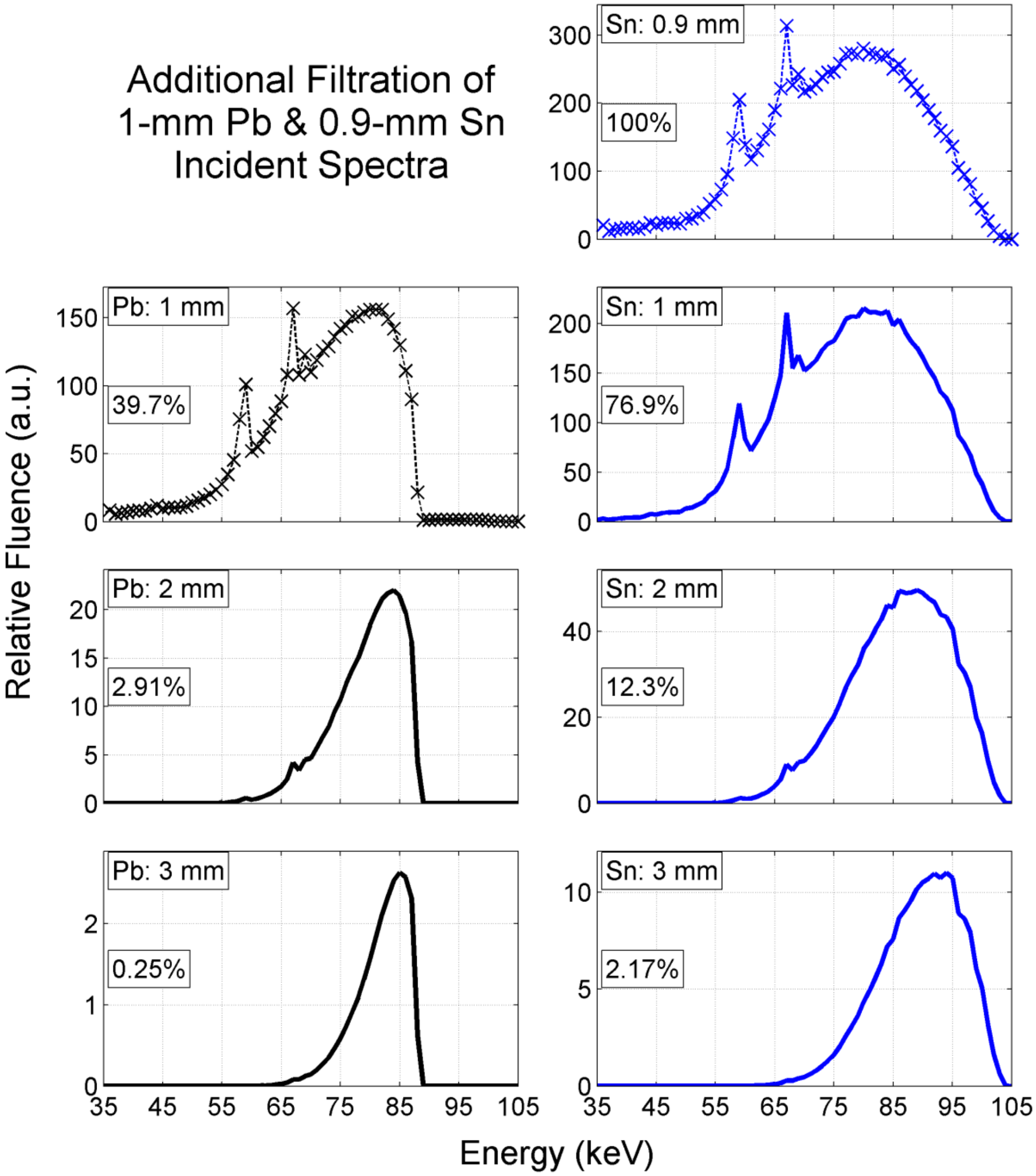

Figure 2.3.1 Computationally-generated spectra after additional filtration with Pb and Sn. These spectra (solid lines) were generated from the experimentally-measured 1-mm Pb-filtered and 0.9-mm Sn-filtered incident spectra (cross markers and dotted lines). The overall fluence available for irradiation (%), relative to the 0.9-mm Sn filter (set to 100%), is displayed within each subplot. Fluence is defined in arbitrary units, but can be compared directly between subplots and with **Figure 2.3.2**.

2.3.2 Quasi-Monochromatic Incident Spectra

One of the major technical concerns regarding benchtop XFCT is that the detection of XRF photons could be overshadowed by Compton-scattered photons with the same energies. To best allow discrimination of XRF photons from scattered photons, the Compton scatter peak and XRF peaks appearing in the XRF/scatter spectra should be separated well and the XRF peaks should be located on a plateau region of the scatter background. Although not readily obtainable with conventional filtration of polychromatic x-rays, quasi-monochromatic x-ray spectra with sufficient intensity could, in principle, be obtained using Bragg diffraction with crystals such as highly oriented pyrolitic graphite (HOPG) [43]. In a previous study [44], this possibility was also investigated specifically for the purpose of benchtop XFCT, resulting in a positive preliminary outlook about the approach that warrants further research and development efforts despite a few technical issues (e.g., requirement of very shallow beam incident angles to produce x-rays with energy above the *K*-edge of gold).

Therefore, quasi-monochromatic x-ray spectra were studied in order to determine the minimum/ideal energy needed to approximately discriminate the gold XRF peaks from the Compton scatter background. The energy ranged from just above the *K*-edge of gold to just below the maximum photon energy of the x-ray source (i.e., 81, 85, 90, 95, 100 keV). Since measured spectra were not readily available at the time of this study, all quasi-monochromatic incident beam spectra were assumed to have undefined, but identical, photon fluence. Considering past experience in quasi-monochromatization of polychromatic x-rays [44], the energy spectrum of each source was assumed to have a Gaussian spread of 10 keV full width at half maximum (FWHM).

2.3.3 Metrics for Analysis of Results

Two metrics were devised to quantitatively analyze the results: the fluorescence signal-to-dose ratio (FSDR) and the fluorescence-normalized scan time (FNST).

The net signal from the gold K_{α} XRF peaks was first extracted for each XRF/scatter spectrum, after necessary corrections, using a background subtraction algorithm [29]. Subsequently, the ratio of the net XRF signal to the dose to the center of the phantom was calculated for each case; this ratio, for both the results from the Pb- and Sn-filtered incident spectra and the quasi-monochromatic incident spectra, was then normalized relative to a reference case (1-mm Pb filter results, which had the lowest signal-to-dose ratio) to obtain a unitless quantity, the FSDR. The reciprocal of the FSDR can also be interpreted as a comparative measure of the dose required to obtain a set amount of XRF signal with each filter.

As the FSDR is independent of incident beam fluence, the FNST was defined as an additional metric. In general, an incident beam spectrum with additional filtration would have lower overall photon fluence and would ostensibly require a proportionally increased scan time to obtain the same net XRF signal. However, spectral differences (e.g., beam hardening) could partially offset this expected increase in scan time. Therefore, in order to take this factor into account, a quantity must be defined with respect to the net XRF signal attained, and not just by considering the overall fluence of the incident spectra. Therefore, the FNST was defined for the results from the Pb- and Sn-filtered incident spectra as the ratio of the net XRF signal from a reference case (0.9-

mm Sn filter results, which had the shortest scan time) to that obtained from each simulation. In other words, the FNST value computed for each spectrum represents the time needed to obtain a set amount of net XRF signal, relative to that obtained using the 0.9-mm Sn filter. As described previously, all the quasi-monochromatic incident beam spectra had undefined, but identical, fluence and thus, the FNST for these spectra could not be defined with respect to the 0.9-mm Sn-filter, and instead were defined relative to a different reference case (quasi-monochromatic 90-keV results, which had the shortest scan time).

2.3.4 XRF/Scatter for Pb and Sn Filtration

Figure 2.3.2 shows the corresponding XRF/scatter spectra for the Pb-filtered and Sn-filtered incident spectra. Qualitatively, the latter had generally higher overall fluence as well as more prominent gold XRF peaks than the former. Using Sn for filtration also favorably shifted the Compton scatter peak to higher energy, further away from the XRF peaks.

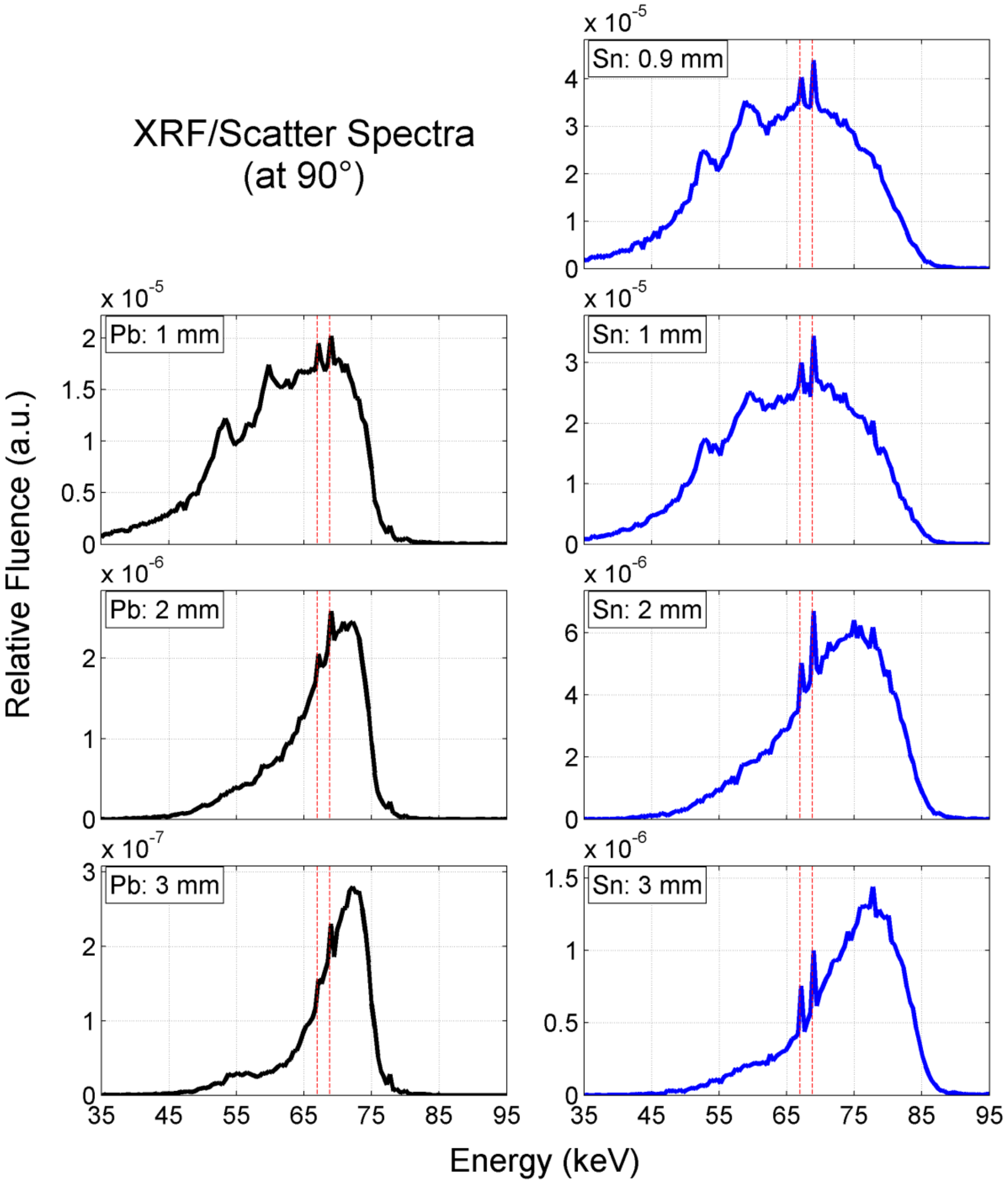

Figure 2.3.2 Corresponding XRF/scatter spectra (at 90°) obtained from MC simulations for Pb-filtered and Sn-filtered incident spectra. The gold XRF peaks of interest (K_α) are located at ~67.0 and ~68.8 keV (vertical dotted red lines). Fluence can be compared directly between subplots and with **Figure 2.3.1**.

For the tested thicknesses of both filter materials, **Figure 2.3.3** shows the FSDR (relative to the 1-mm Pb filter; linear scale) and the FNST (relative to the 0.9-mm Sn filter; log scale); the results are also tabulated in **Table 2.3.1**. Quantitatively, the FSDR values increased with increasing filter thicknesses for both filter materials. The 0.9-mm Sn filter and 1-mm Pb filter, as used experimentally, had comparable FSDR values. However, the FNST for the 1-mm Pb filter was almost 3 times as much as that for the 0.9-mm Sn filter, a fact that matched experimental observations [31], providing another strong support for the validity of the current MC model. For thicknesses above 2 mm, both the Sn and Pb filters resulted in similar FSDR values. However, filtration using Pb required considerably longer FNST compared to that using Sn. In general, for both filter materials, the FNST increased at a much higher rate for a given increase in FSDR. Using Sn for filtration, instead of Pb, is consistently advantageous in terms of both FSDR as well as FNST.

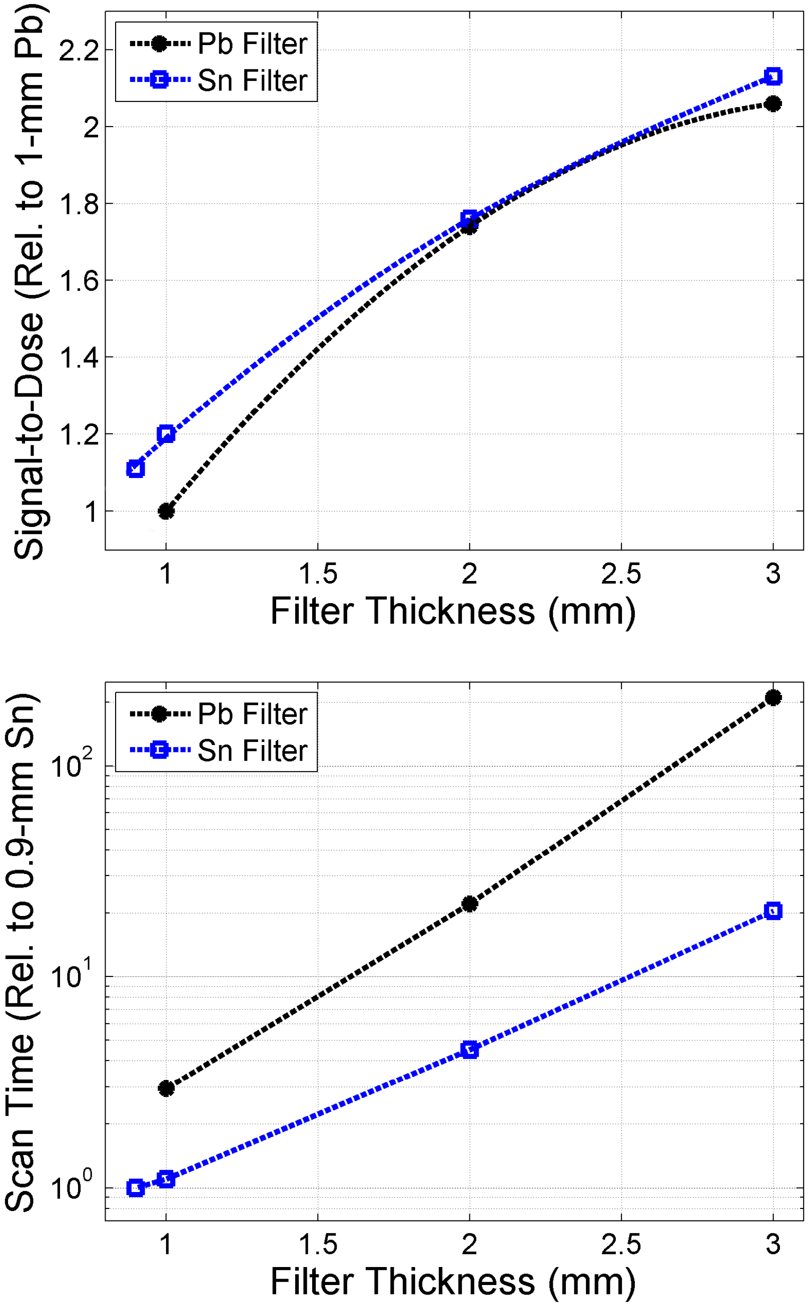

Figure 2.3.3 Metrics for analysis of XRF/scatter spectra resulting from Pb-filtered and Sn-filtered incident spectra as a function of filter thickness. (top) Fluorescence signal-to-dose ratio (FSDR, relative to 1-mm Pb filter results; linear scale). (bottom) Fluorescence-normalized scan time (FNST, relative to 0.9-mm Sn filter results; log scale).

Table 2.3.1 Fluorescence signal-to-dose ratio (FSDR) and fluorescence-normalized scan time (FNST) for XRF/scatter spectra resulting from Pb-filtered and Sn-filtered incident spectra. FSDR is relative to 1-mm Pb filter results while FNST is relative to 0.9-mm Sn filter results.

Incident Spectrum	Fluorescence Signal-to-Dose Ratio*	Fluorescence-Normalized Scan Time†
105 kVp, Lead (Pb) Filter		
1.0 mm	1.00	2.94
2.0 mm	1.74	22.1
3.0 mm	2.06	211
105 kVp, Tin (Sn) Filter		
0.9 mm	1.11	1.00
1.0 mm	1.20	1.10
2.0 mm	1.76	4.51
3.0 mm	2.13	20.4

***Relative to 1-mm Pb filter results**

†Relative to 0.9-mm Sn filter results

2.3.5 XRF/Scatter for Quasi-Monochromatic Spectra

The XRF/scatter spectra resulting from quasi-monochromatic incident beam spectra are displayed in **Figure 2.3.4**. Qualitatively, it can be seen that increasing the source energy shifted the scatter peak to higher energy, as expected, which allowed the XRF peaks to be more easily discerned (i.e., have a higher signal-to-background ratio). For the modeled configuration, quasi-monochromatic energy of at least 90 keV was required to clearly distinguish the gold XRF x-rays from the Compton scatter background. In theory, higher beam energy would be preferable since the scatter peak would not overshadow the gold XRF peaks. However, the specifics of a given XFCT configuration would determine the actual shape of the scatter spectra and its effect on the signal-to-background ratio of the XRF peaks.

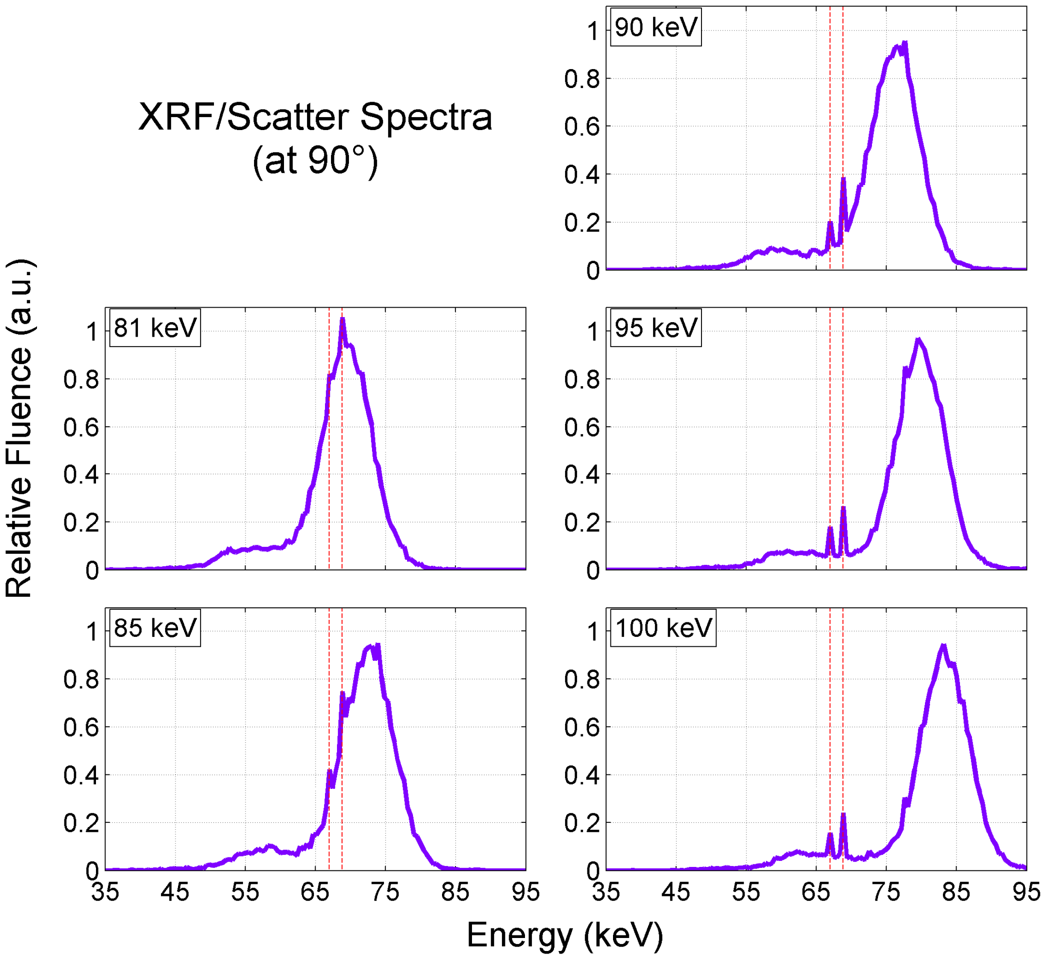

Figure 2.3.4 XRF/scatter spectra from quasi-monochromatic (10-keV FWHM) incident spectra. The gold XRF peaks of interest (K_α) are located at ~67.0 and ~68.8 keV (vertical dotted red lines). Qualitatively, as incident energy was increased and the 90° scatter became more energetic, the gold XRF peaks can be more easily discerned from background. Fluence is relative to this figure only and under the condition that all quasi-monochromatic incident spectra were assumed to have identical and arbitrary overall fluence.

Figure 2.3.5 shows the FSDR (relative to the 1-mm Pb filter, linear scale) and the FNST (relative to the 90-keV results, linear scale) for these quasi-monochromatic spectra; the results are also tabulated in **Table 2.3.2**. The FSDR increased linearly with increasing source energy in the range between 81 and 100 keV, with an expected improvement of up to a factor of almost 20 (compared to the 1-mm Pb filter) with a 100-keV incident beam. Although FNST could not be compared with the filtered incident spectra, for reasons explained previously, a comparison can be made within the quasi-monochromatic spectra results. Note that the FNST was a minimum for the 90-keV quasi-monochromatic incident spectrum. While the higher energies resulted in improved FSDR, this came at the expense of an increase in FNST. For example, comparing the results from the 90-keV and 100-keV beams, the FSDR increased by 13% while the FNST increased by 35%.

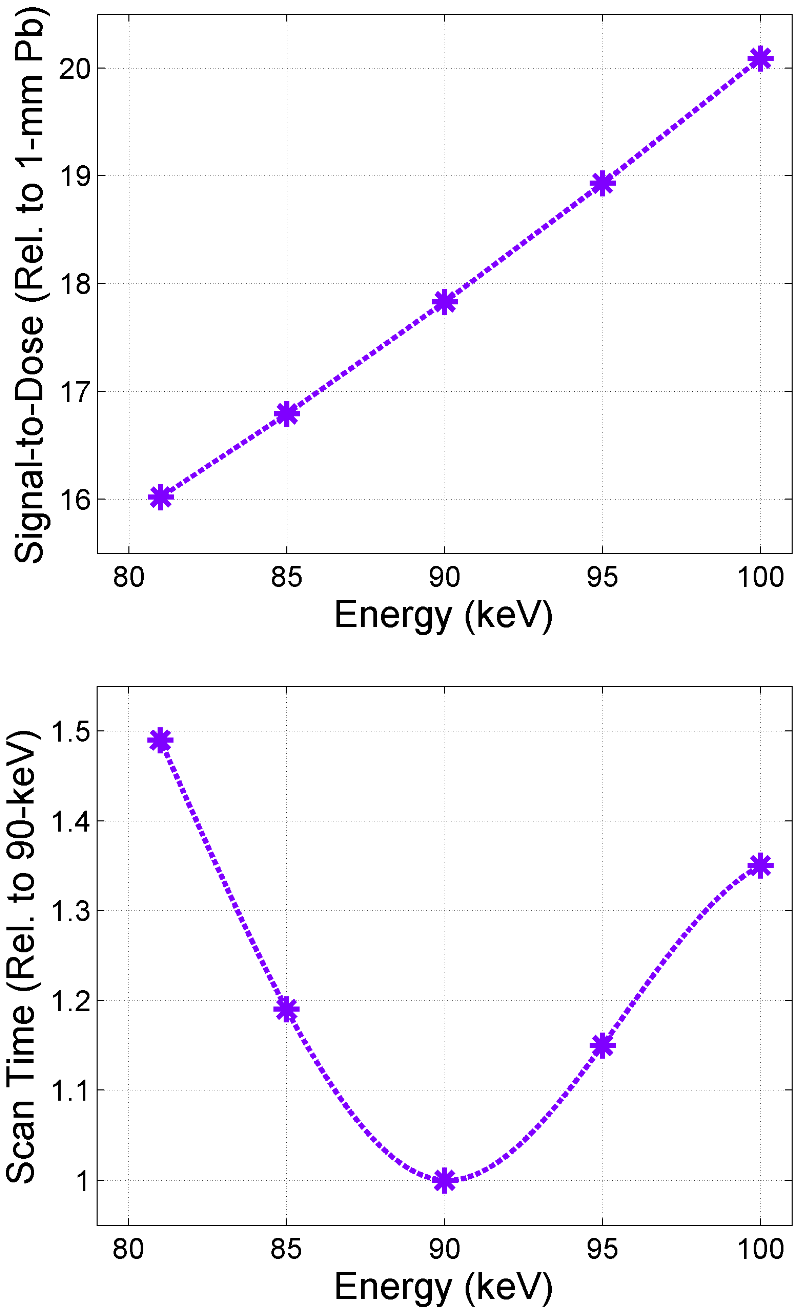

Figure 2.3.5 Metrics for analysis of XRF/scatter spectra resulting from quasi-monochromatic incident spectra (81, 85, 90, 95, and 100-keV with 10-keV FWHM). (top) Fluorescence signal-to-dose ratio (FSDR, relative to 1-mm Pb filter results; linear scale). (bottom) Fluorescence-normalized scan time (FNST, relative to 90-keV results; linear scale). Note that the FSDR can be compared with the filtered incident spectra results in **Figure 2.3.3(a)**, but the FNST reported here is for comparison within this figure only.

Table 2.3.2 Fluorescence signal-to-dose ratio (FSDR) and fluorescence-normalized scan time (FNST) for XRF/scatter spectra resulting from quasi-monochromatic incident spectra. FSDR is relative to 1-mm Pb filter results while FNST is relative to 90-keV results. Note that the FSDR can be compared with the filtered incident spectra results in **Table 2.3.1**, but the FNST reported here is for comparison within this table only.

Incident Spectrum	**Fluorescence Signal-to-Dose Ratio***	**Fluorescence-Normalized Scan Time‡**
Quasi-monochromatic		
81 keV	16.0	1.49
85 keV	16.8	1.19
90 keV	17.8	1.00
95 keV	18.9	1.15
100 keV	20.1	1.35

***Relative to 1-mm Pb filter results**

‡Relative to 90-keV results

2.4 Performance Increase of Experimental *K*-shell XFCT System

By taking the predictions from the computational work into consideration, an experimental study was performed to realize actual performance improvements of the XFCT system using a kilowatt-range x-ray source.

2.4.1 High-Power X-ray Source

With the originally-configured low-power (~50 W) x-ray source, operated at 105 kVp and 0.45 mA of current, excessively long scan time was debilitating in the context of using the system for practical imaging tasks. In order to reduce the scan time significantly, the XFCT system was retrofitted with a high-power (~3 kW) clinical orthovoltage x-ray unit (RT250, Philips Healthcare) as the excitation source. The filtration strategy was re-evaluated experimentally for 1-, 2-, and 3-mm-thick Sn filters in conjunction with two different accelerating potentials (100 and 125 kVp at 25 mA of current). The favorable spectrum and increased photon flux at 125 kVp and 25 mA allowed the use of a 2-mm-thick Sn filter, resulting in a hardened incident x-ray beam to optimize XRF production.

2.4.2 Detection Limit Determination

The material detection limit for GNPs was determined at the new settings (125 kVp, 25 mA, 2-mm Sn filter) using calibration phantoms with water and GNPs (Aurovist™, Nanoprobes Inc.) at 20, 10, 5, 1, and 0 mg/cm^3 (2, 1, 0.5, 0.1, and 0 wt. %). The net XRF signal from each phantom was obtained for an acquisition time of 15 s and corrected for efficiency and also attenuation using a Compton scatter-based normalization (the methodology will be described in detail in a subsequent Chapter in the context of L-shell XRF, but an equivalent procedure was applicable to K-shell XRF as well). The corrected fits were plotted as a function of GNP concentration. The detection limit was defined as a concentration below which the net XRF signals cannot be considered as true signals (at the 95% confidence level) above the noise of the background (σ_b).

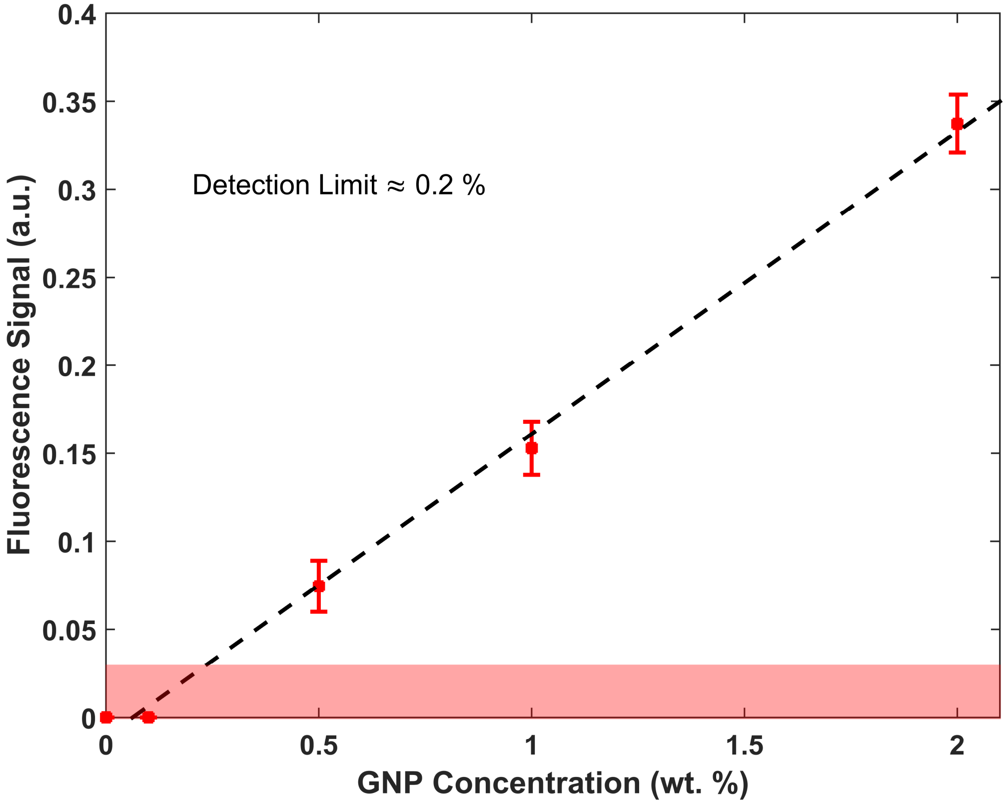

Figure 2.4.1 Calibration curve for determining detection limit of GNPs with the *K*-shell XFCT system and high-power x-ray source. The source was operated at 125 kVp, 25 mA with a 2-mm Sn filter. The acquisition time was 15 s for each data point. The GNP concentration corresponding to the intersection of the line of best-fit and the shaded region represents the detection limit: ~0.2 wt. % or ~2 mg/cm^3.

2.4.3 Imaging of Phantom

A full cone-beam XFCT of the 3-cm-diameter phantom was then performed, in an almost identical manner as previously, but with the new source (125 kVp, 25 mA, 2-mm Sn filter, compared to the previous conditions of 105 kVp, 0.45 mA, and 0.9-mm Sn filter) and with the phantom loaded with inserts containing lower concentrations of GNPs: 2, 5, and 10 mg/cm^3 (0.2, 0.5, and 1 wt. %) *vs*. 5, 10, and 20 mg/cm^3 (0.5, 1, and 2 wt. %). Furthermore, the previously-developed image reconstruction algorithm [31] was improved by using the Compton-scatter-based background fit for XRF signal extraction (more accurate) and also attenuation correction (requiring no *a priori* information).

The total scan time to image one slice of the 3-cm-diameter small-animal-sized PMMA phantom using the low-power source took approximately 6 hours to complete, with a single detector translated 11 times; the detection limit for GNPs was on the order of 5 mg/cm^3 (0.5 wt. %). In comparison, with the high-power source, the total scan time was decreased to approximately 1.5 hours (factor of 4 reduction in scan time). Simultaneously, the detection limit was lowered by a factor of 2.5, allowing GNP concentrations as low as 0.2 wt. % to be imaged. Decreasing the filter thickness, for example to 1 mm, would lower the scan time even further (to around 30 minutes) at the expense of image quality and detection limit. Comparisons of various source configurations are shown in **Table 2.4.1**. The reconstructed image (**Figure 2.4.2**) demonstrated accurate localization of all inserts, as evidenced by the clear demarcation of the locations and relative concentrations of the GNP-containing inserts, including the low concentration 0.2 wt. % insert. Implementation of additional/array detectors for parallel data acquisition would lower scan time proportional to the number of detector elements.

Table 2.4.1 Comparison of experimental *K*-shell XFCT scan time and detection limit for various source configurations. The total scan time per slice takes into account the overhead time needed for detector translations and phantom rotations.

	105 kVp, 0.45 mA (0.9-mm Sn filter)	**125 kVp, 25 mA (2-mm Sn filter)**	**125 kVp, 25 mA (1-mm Sn filter)**
Scan Time per Projection^	60 s	15 s	5 s
Total Scan Time per Slice*	~6 hours	~1.5 hours	~0.5 hours
GNP Detection Limit	0.5 wt. %	0.2 wt. %	~0.5 wt. %

^Assuming 30 projections over 360° of rotation

***When using one detector for 11 translations**

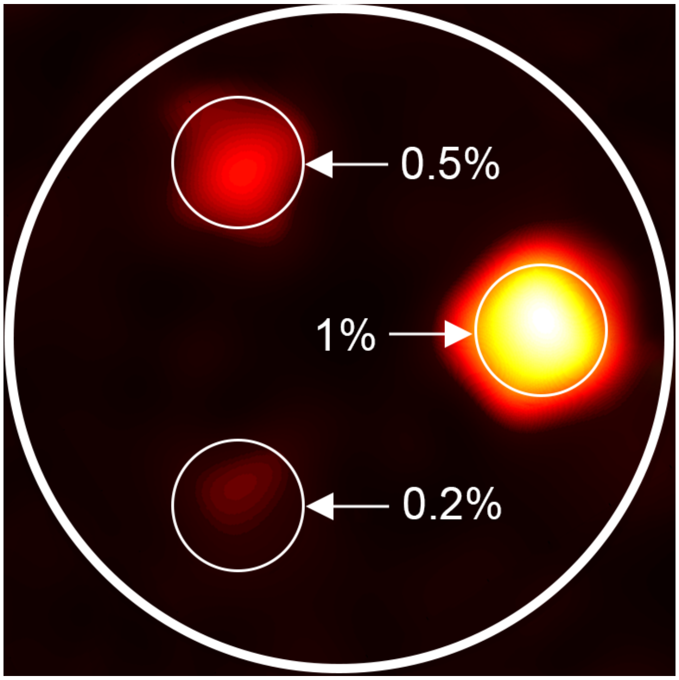

Figure 2.4.2 Reconstructed XFCT image of 3-cm-diameter PMMA phantom with GNP-loaded inserts (0.2, 0.5, and 1 wt. %). All imaging inserts were localized accurately.

2.5 Feasibility of Simultaneous Micro-CT Capability with XFCT

One of the exciting features of a benchtop XFCT system is the possibility of performing multimodal imaging through simultaneous micro-CT and XFCT in a single platform. In order to realize this possibility, however, a number of technical challenges must be successfully overcome. One key challenge requiring immediate attention is to establish the feasibility of performing micro-CT under conditions that are significantly different from those associated with typical micro-CT scanning. A consequence of tailoring the incident x-ray spectrum, as explored in the previous section, is the lack in lower energy photons which are crucial for contrast in micro-CT. Specifically, the filtration of the x-ray beam using Pb and Sn to optimize the incident beam spectra for XFCT (i.e., suppressing photons below the *K*-edge of gold) is detrimental to micro-CT as these higher energy photons penetrate low-*Z* materials like tissue very easily and therefore, do not produce enough contrast. This implies that compromises may have to be made when selecting an incident x-ray spectrum that is optimal for simultaneous micro-CT and XFCT. Therefore, the effects of using different incident x-ray spectra, some typically used for micro-CT and those optimized for XFCT, to irradiate a phantom containing GNPs were explored both computationally and experimentally.

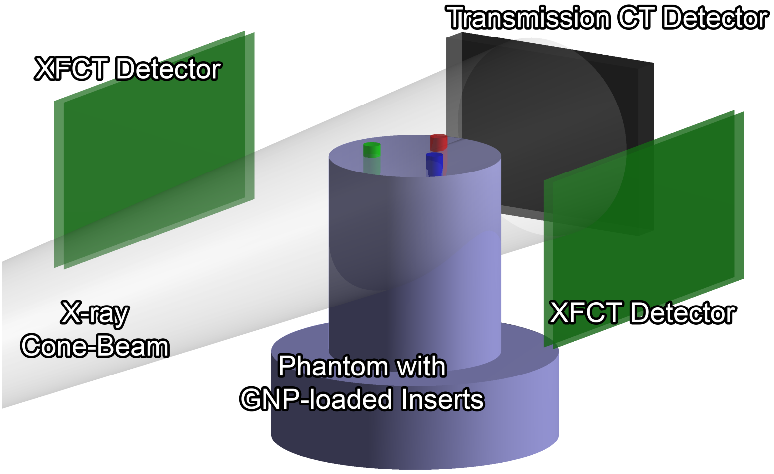

Figure 2.5.1 Schematic of a proposed multimodal imaging system capable of simultaneous micro-CT and XFCT. A phantom with GNP-loaded inserts, array detectors for XFCT, and transmission detector for micro-CT are shown. Irradiation can be accomplished using a polychromatic cone-beam x-ray source.

2.5.1 Simulation of Micro-CT of GNP-Loaded Phantom

The MC model of the XFCT system was employed once again to investigate the quality of micro-CT images obtainable with XFCT-optimized x-ray source spectra. Although a physical transmission detector had not been implemented into the experimental system, one was simulated in MCNP5 by modeling a planar radiograph flux image (FIR5) tally on the distal end of the phantom along the beam-line. Imaging inserts with GNP concentrations of 20, 10, and 5 mg/cm^3 (2, 1, and 0.5 wt. %) were placed in the phantom. The phantom was irradiated by the following incident x-ray spectra: 50 kVp filtered by 2 mm of aluminum (Al), 75 kVp filtered by 2 mm of Al, 105 kVp filtered by 1 mm Sn, and 125 kVp filtered by 2 mm of Sn. For consistency, these spectra (**Figure 2.5.2**) were generated using software (SpekCalc) [45], rather than using experimentally-measured spectra. Note that the 50 kVp and 75 kVp spectra cannot be used for inciting *K*-

shell XRF from gold as the maximum energy in either case is lower than the *K*-edge of gold.

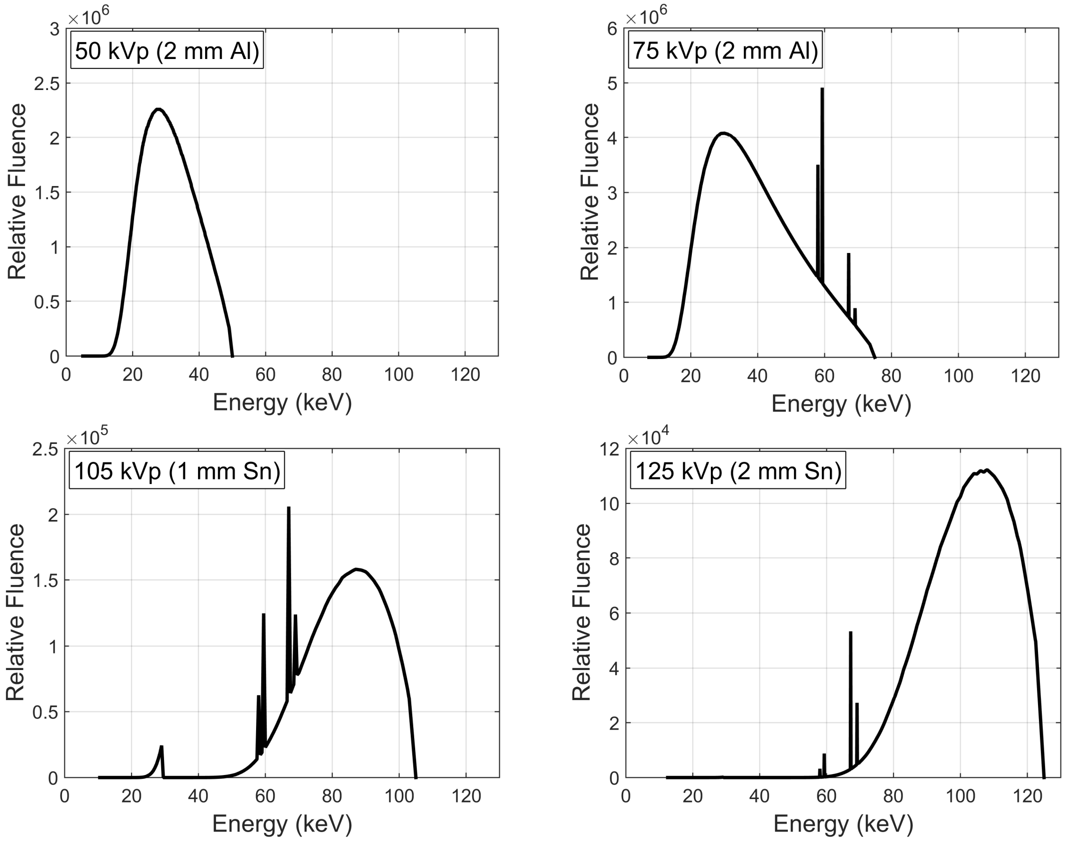

Figure 2.5.2 Incident x-ray spectra for micro-CT investigations. Spectra were characterized by tube potential (kVp) and filtration using Al or Sn: (top row) 50 kVp (2 mm Al) and 75 kVp (2 mm Al); (bottom row) 105 kVp (1 mm Sn) and 125 kVp (2 mm Sn).

The transmitted photons were scored using the radiography tally while the phantom was completely rotated in 1° increments to provide a total of 360 projections for image reconstructions. Using the projection data, a standard filtered back-projection fan-beam reconstruction algorithm was used to reconstruct an axial slice of the phantom (i.e., the slice aligned with the center of the beam) showing the three GNP-containing inserts (**Figure 2.5.3**).

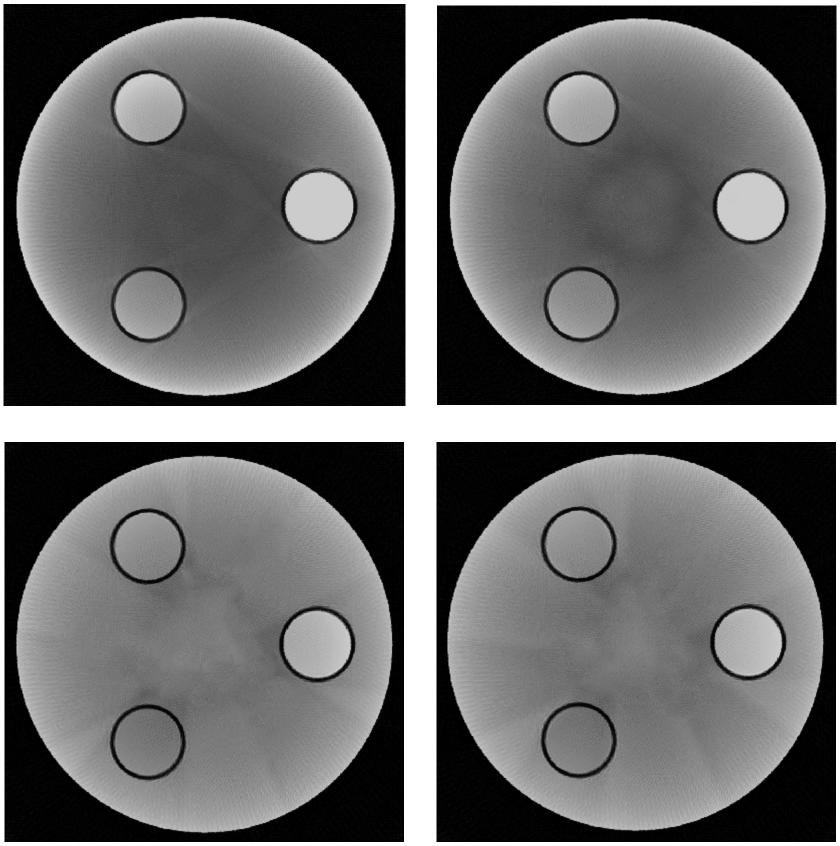

Figure 2.5.3 Micro-CT images from simulation for each incident x-ray spectrum. (top row) 50 kVp (2 mm Al) and 75 kVp (2 mm Al); (bottom row) 105 kVp (1 mm Sn) and 125 kVp (2 mm Sn).The GNP-containing inserts in each image were, in order from top-left and going clockwise: 10, 20, and 5 mg/cm^3 (1, 2, and 0.5 wt. %).

2.5.2 Experimental Micro-CT of GNP-Loaded Phantom

For comparison with MC simulations, micro-CT images of the physical GNP-loaded phantom were also obtained experimentally under conditions similar to those described in the previous section. This was accomplished using a commercial cabinet irradiation system (X-RAD 225Cx, Precision X-Ray Inc.). The same acquisition time was used for all scans. Manufacturer-provided software was used to reconstruct the images (**Figure 2.5.4**).

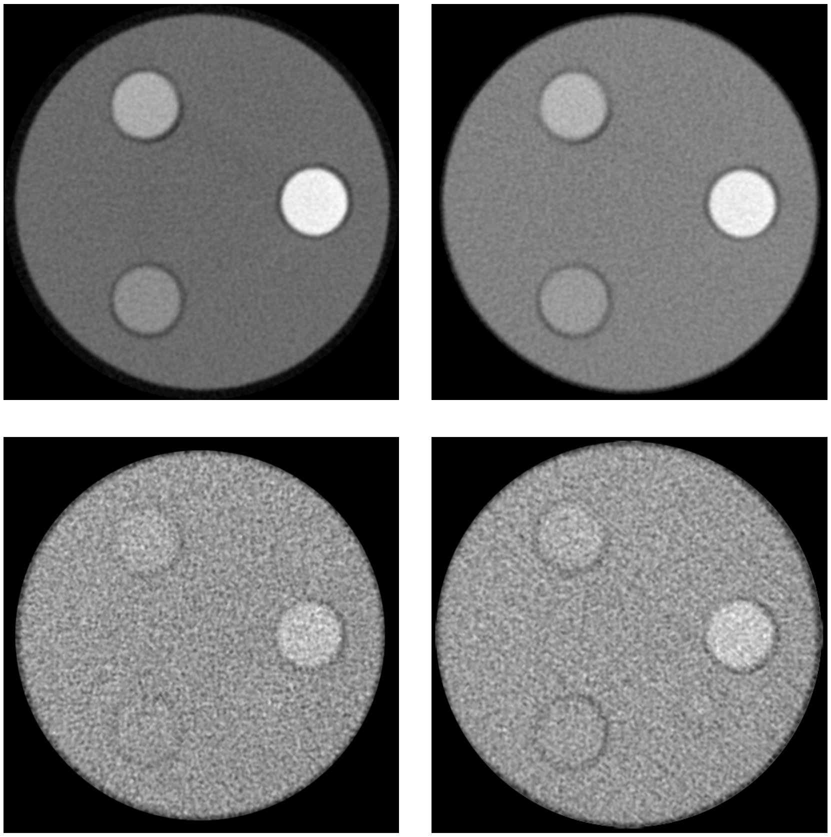

Figure 2.5.4 Micro-CT images from experiment for each incident x-ray spectrum. (top row) 50 kVp (2 mm Al) and 75 kVp (2 mm Al); (bottom row) 105 kVp (1 mm Sn) and 125 kVp (2 mm Sn). The GNP-containing inserts in each image were, in order from top-left and going clockwise: 10, 20, and 5 mg/cm^3 (1, 2, and 0.5 wt. %).

2.5.3 Quantification and Comparison of Results

The Michelson contrast [46] of each GNP-containing insert in the reconstructed images (8-bit grayscale) was computed. It was defined in terms of the average pixel intensity of each GNP-containing insert region (I) and that of the PMMA portion of the phantom (I_B), as in:

$$Contrast\ (\%) = \left(\frac{I - I_B}{I + I_B}\right) \times 100$$

A contrast of ±100% signifies the maximum contrast while 0% signifies that there is no difference between the pixel intensities of the GNP-containing insert in question and the PMMA region of the phantom. A negative value for the contrast of an insert implies that it is seemingly less attenuating than the PMMA portion of the phantom. This can be attributable to the detection of XRF which originated from that insert. For contrast less than approximately ±5%, the insert was assumed to be indistinguishable from the local background (i.e., PMMA region).

In comparing the simulated and experimental results, slight differences were found due to changes in the imaging geometry. However, the overall trend in image quality was consistent. The results suggested that all three GNP-containing inserts at the tested concentrations (20, 10, and 5 mg/cm^3) can be visualized with micro-CT using the 50 kVp (2 mm Al) and 75 kVp (2 mm Al) spectra. However, using the higher energy 105 kVp (1 mm Sn) and 125 kVp (2 mm Sn) spectra (i.e., the spectra typically used for XFCT), the two lower concentration inserts were indistinguishable from background. Generally, the contrast of the GNP-containing insert regions, tabulated in **Table 2.5.1**, decreased dramatically with increasing hardness in the incident x-ray spectrum. The only hint of the presence of the inserts in some images was due to the small annular air gap surrounding each one. Interestingly, when using the XFCT-optimized spectra, the XRF generated from the GNPs provided some negative contrast. This was evident in the simulations, possibly due to close proximity of the transmission detector with respect to the phantom. The experimental images did not show this effect as the imaging geometry may not have been conducive to detection of the XRF photons. Overall, the use of incident x-ray spectra optimized for XFCT resulted in degradation of micro-CT image quality and contrast.

Table 2.5.1 Contrast value (%) of each GNP-containing insert in simulated and experimental micro-CT images obtained using various incident x-ray spectra.

GNP Concentration	**50 kVp (2 mm Al)**	**75 kVp (2 mm Al)**	**105 kVp (1 mm Sn)**	**125 kVp (2 mm Sn)**
		Simulated Image Contrast (%)		
20 mg/cm^3 (2%)	30.8	29.1	15.5	16.3
10 mg/cm^3 (1%)	24.2	20.8	3.32	2.24
5 mg/cm^3 (0.5%)	14.6	10.8	-4.80	-5.22
		Experimental Image Contrast (%)		
20 mg/cm^3 (2%)	38.2	29.3	10.7	12.0
10 mg/cm^3 (1%)	23.3	16.1	5.03	4.94
5 mg/cm^3 (0.5%)	13.4	8.13	0.658	0.324

2.6 Discussion

The significance and usefulness of the current MC model are especially highlighted when considering the fact that each component of the experimental benchtop XFCT system has been modeled in detail. If created based on valid assumptions/approximations, a simplified MC model could still provide meaningful results in a computationally efficient manner. For example, simplified MC models [30, 44, 47] were instrumental in investigations of many critical issues including the effect of detection geometry on acquired XRF/scatter spectra, feasibility of cone-beam XFCT, and development of an effective reconstruction algorithm for XFCT images. Nevertheless, there had been an unmet need to develop a more comprehensive and robust MC model such as the current one, because simplified MC models might not always yield results accurate enough to guide further optimization efforts after initial experimental investigations, due to their inability to properly predict subtle influences of various components within the experimental setup on the production/detection of XRF and scattered photons. Thus, a successful experimental validation of the MC model as shown in this work can be attributed, at least in part, to the effort put into creating a model that is as detailed and realistic as possible. Once rigorously validated, a realistic MC model should also have predicting power. For example, besides the XRF/scatter spectra used for initial experimental validation, the FSDR and FNST results from the current MC simulations for additional thicknesses of Sn also matched experimental data available from a study [31] in which remarkable improvements (e.g., reduction of scan time by a factor of 3) were established in the performance of the benchtop XFCT system by implementing a 0.9-mm Sn filter instead of a 1-mm Pb filter.

The results from the exemplary applications of the current MC model provided valuable insight into further modification/optimization strategies of the experimental benchtop XFCT setup. Most notably, the current study quantified the degree of interplay between FSDR and FNST, dependent on the thickness of Sn- and Pb-filters. As a result, an optimum filter thickness can be determined, in consideration of this interplay as well as other constraints such as available x-ray tube power, acceptable scan time, and desired GNP detection limit.

Noting the reliability and predictive power of the MC model as demonstrated in this study, the aforementioned possibilities were deemed realistic and, in fact, confirmed with the high-power (~3 kW) source as evidenced by the lower detection limit of 2 mg/cm^3 (0.2 wt. %). While the clinical orthovoltage source used would not qualify as a "benchtop" device, this work has already prompted the upgrade of the XFCT system with a more compact high-power source.

The MC model was also extremely useful in investigating the feasibility of performing simultaneous micro-CT with XFCT as the results clearly elucidated potential technical issues regarding micro-CT scanning with an incident x-ray source spectrum optimized solely for the purpose of benchtop XFCT under the cone-beam geometry. Further optimization efforts and/or development of alternative imaging schemes (e.g., dual-energy scan) would be necessary to improve the micro-CT image quality during simultaneous micro-CT/XFCT scanning. The current MC model may even help identify other unforeseen issues that might hinder seamless integration of the two modalities.

In addition to the exemplary applications presented in this work, there are many other applications of the MC model for further development of the benchtop XFCT system. For example, the model can be used to thoroughly study the effects of higher x-ray tube potentials and different filtration options. It can also be used to optimize other parameters such as beam collimation, detector collimation, and detection/imaging geometry. Especially, the model is an indispensable tool for investigating the approaches that cannot immediately be tested experimentally, due to technical and/or financial difficulties (e.g., quasi-monochromatization using HOPG crystals). Overall, it can serve as a reliable surrogate of time-consuming and potentially expensive experimentation, while producing accurate and realistic results that can be translated to tangible improvements in the experimental benchtop XFCT system.

CHAPTER 3
EXPERIMENTAL INVESTIGATIONS OF DIRECT *L*-SHELL XRF IMAGING

3.1 Background and Objective

This investigation aimed to demonstrate the feasibility of performing *L*-shell XRF imaging of GNPs with an ordinary benchtop polychromatic x-ray source and relatively simple experimental setup, while achieving a detection limit comparable to that associated with synchrotron-based systems. Due to the small size of samples for which gold *L*-shell XRF analysis is inherently suitable for, a direct XRF imaging technique (i.e., planar imaging) appeared to be more advantageous than a tomographic technique (i.e., *L*-shell XFCT) and, therefore, direct 2D mapping of properly corrected XRF signals was attempted.

3.2 Experimental Demonstration of Direct *L*-shell XRF Imaging

The proof-of-principle experimental system for 2D planar XRF imaging consisted of a cylindrical phantom, a benchtop x-ray source, source collimator, an energy-resolving x-ray detector system, detector collimator, and imaging stages (**Figure 3.2.1**).

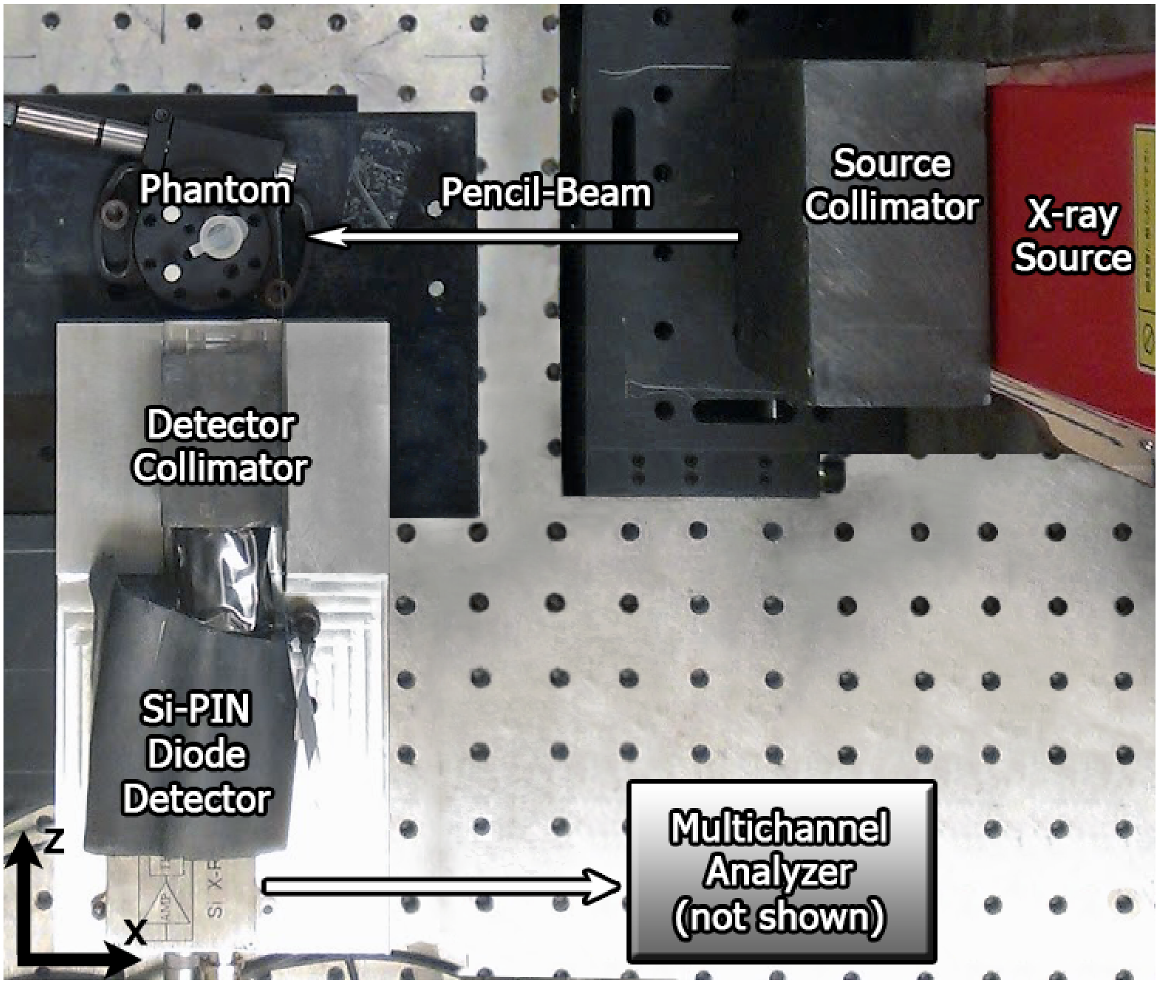

Figure 3.2.1 Components of experimental *L*-shell XRF imaging system to image a GNP-containing phantom. Top-down photograph (in x-z plane) of the current imaging geometry showing all components: low-power x-ray source, source collimator, GNP-containing phantom, Si-PIN diode detector, and detector collimator. A pencil-beam of x-rays was incident onto the phantom along the negative x-axis.

3.2.1 Benchtop X-ray Source and XRF Detection System

The x-ray source was the same low-power (~50 W) tungsten-target microfocus x-ray source (L9631, Hamamatsu Photonics K.K.) used for the initial *K*-shell XFCT system. After performing a set of optimization studies at various tube potentials, 62 kVp was found to maximize *L*-shell XRF production from gold (9.71 and 11.4 keV) under the given experimental geometry. Therefore, the source was operated at 62 kVp and 0.8 mA of beam current. A pencil-beam was generated with the aid of a 4-cm-thick Pb collimator with a 2.5-mm-diameter aperture. The beam was then filtered through 1 mm of Al in order to suppress the tungsten L_β peak (9.67 keV) from the source which would overlap the gold L_α peak (9.71 keV) used for imaging. Due to a slight divergence, the beam diameter was 3 mm at the location of the phantom, as measured using radiochromic film (Gafchromic EBT, ISP Inc.) and shown in **Figure 3.2.3(b)**.

A silicon (Si)-PIN photodiode detector (XR-100CR, Amptek Inc.), placed at 90° with respect to the beam direction, was used to detect the XRF/scatter spectra from each phantom. The detector view was restricted using a 4-cm-thick Pb collimator with an aperture diameter of 2.5 mm.

3.2.2 Calibration Phantoms

In order to determine the detection limit (i.e., the lowest detectable amount of GNPs), 12-mm-diameter plastic calibration phantoms containing water and GNPs (Aurovist™, Nanoprobes Inc.) at a wide range of concentrations (20, 10, 5, 0.5, 0.05, and 0.005 mg/cm^3) were prepared using serial dilution and a precision balance. An additional phantom was filled with water only (i.e., 0 mg/cm^3 GNP concentration). This range of GNP concentrations was chosen based on biologically-attainable concentrations, on the order of mg to μg GNPs per cm^3 [14, 48], depending on GNP-specific pharmacokinetics and targeting strategies.

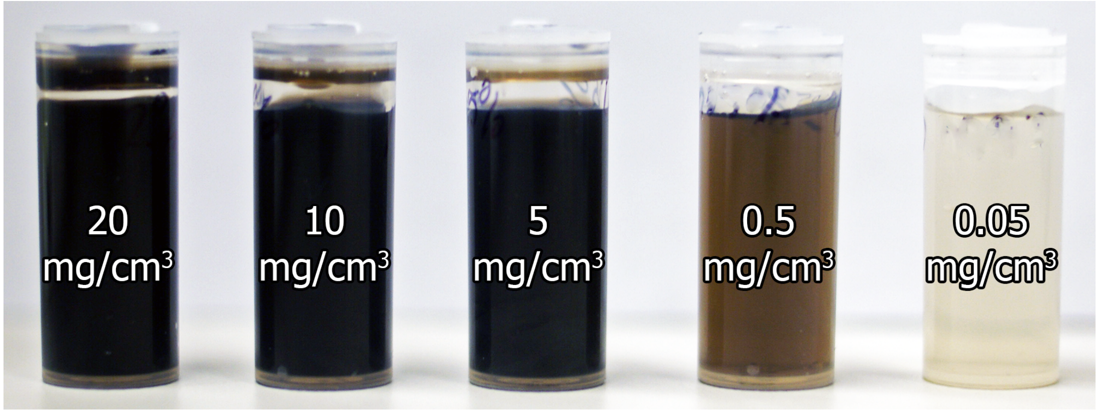

Figure 3.2.2 Photograph of water/GNP-containing calibration phantoms used for detection limit determination. (left to right): 20, 10, 5, 0.5, 0.05 mg/cm^3 (2, 1, 0.5, 0.05, 0.005 wt. %). Not pictured: 0.005 mg/cm^3 and water-only phantoms.

Each phantom was irradiated using the pencil-beam at a source-to-phantom distance of 22 cm (16 cm from the collimator exit to the phantom surface). The resulting XRF/scatter spectra were detected at a phantom-to-detector distance of 7 cm (3 cm from the phantom surface to the detector collimator entry). The acquisition time was fixed at 10 minutes for each calibration phantom. The physical voxel size created by the pencil-beam and detector collimator aperture for direct XRF imaging was determined to be 1.73×10^{-2} cm^3 by calculating the volume created by the intersection of two cylinders of diameters, 3 mm (pencil-beam) and 2.5 mm (detector collimator aperture), respectively. Thus, the mass of GNPs presented in a voxel imaged by the current experimental setup was estimated to be 350, 175, 87.5, 8.75, and 0.875, 0.0875, and 0 µg for the calibration phantoms, under the reasonable assumption that GNPs were uniformly distributed throughout the phantoms, corresponding to the respective GNP concentrations of 20, 10, 5, 0.5, 0.05, 0.005, and 0 mg/cm^3.

3.2.3 Imaging Phantom

An imaging phantom (**Figure 3.2.3**) was prepared by filling a plastic container of the same diameter as the calibration phantoms (12 mm) with a gelatin-based, tissue-equivalent gel [49]. After the gel solidified, a water solution containing GNPs at a concentration of 20 mg/cm^3 (2 wt. %) was slowly injected into the gel, while pulling the needle from the bottom to the top of the phantom, to create a continuous volume containing the solution. Injection of a larger amount of solution at the approximate center of the phantom, compared to the bottom and top, allowed that region to mimic a GNP-laden tumor with a volume of approximately 1 cm^3 with simulated blood vessels leading into and out of it.

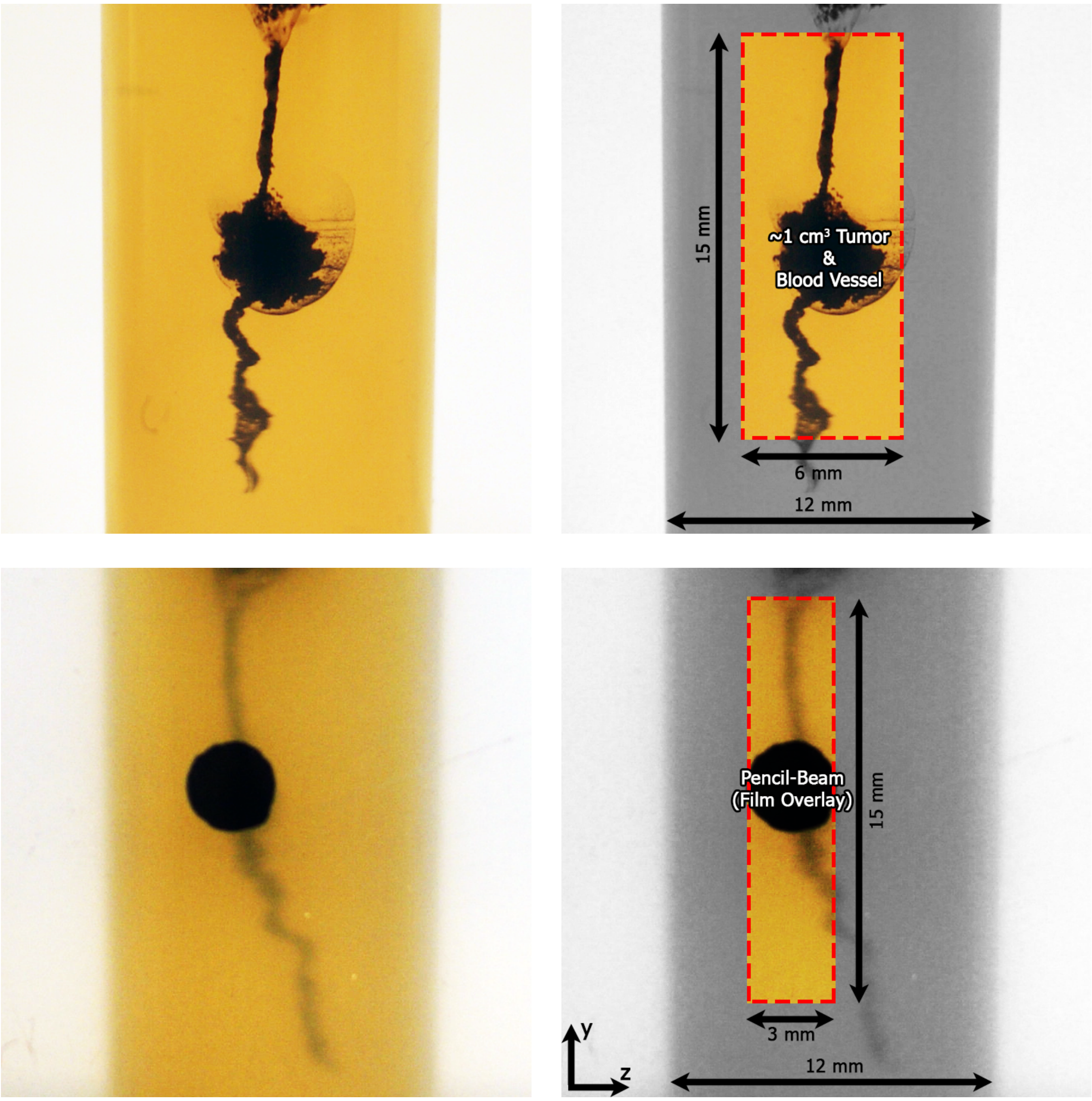

Figure 3.2.3 Close-up photographs of imaging phantom with simulated GNP-laden blood vessel and ~1 cm^3 tumor. Box shows the region of interest that was imaged. (top row) The detector's eye view of the phantom (in x-y plane) used for imaging. The pencil-beam of x-rays propagated along the negative x-axis. (bottom row) Beam's eye view (in z-y plane) with overlaid radiochromic film image showing incident pencil-beam of x-rays at one particular vertical (y) position. The detector was located at the left side of the image (along the negative z-axis).

The imaging phantom was aligned such that the pencil-beam impinged on the approximate center of the simulated tumor region, as shown in **Figure 3.2.3(b)**. Then, keeping the source and detector stationary, the phantom was translated horizontally (along the beam direction) and vertically, in steps of 0.3 mm, to acquire data from the region of interest (ROI), a 6 mm (horizontal) by 15 mm (vertical) area within the phantom containing the simulated tumor and blood vessels, shown in **Figure 3.2.3(a)**. The imaging step size of 0.3 mm resulted in oversampling across the ROI, producing an effective voxel size of 2.70×10^{-4} cm^3 in the final image (~5.5 μg of GNPs within each voxel at the maximum concentration of 20 mg/cm^3). The ROI within the imaging phantom was covered by a total of 1000 voxels during XRF measurements, with an acquisition time of 30 s per voxel.

3.2.4 XRF Signal Extraction and Processing

The spectra obtained from all measurements were corrected for detection efficiency (ε), accounting for the probability of transmission through the Be window of the detector and the probability of interaction within the Si detector crystal at a given energy (E):

$$\varepsilon(E) = \left(e^{-\mu_{Be}(E)\times t_{Be}}\right)\left(1 - e^{-\mu_{Si}(E)\times t_{Si}}\right)$$

where μ and t are, respectively, the linear attenuation coefficient and the thickness of each material. The total signal from the gold XRF peaks of interest (9.71 and 10.4 keV) was then extracted from the background using linear fits based on their respective energy windows and added together to extract the net XRF signal P_{net} (**Figure 3.2.4**).

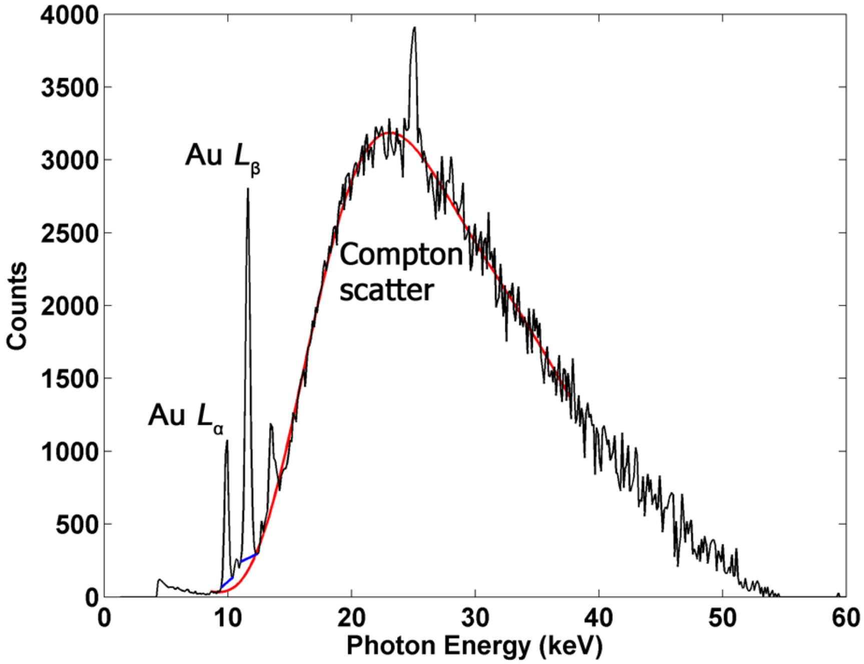

Figure 3.2.4 Typical XRF/scatter spectrum acquired from Si-PIN detector, after corrections for detection efficiency. The prominent gold *L*-shell XRF peaks from GNPs, as well as the Compton scatter background are visible. Additional peaks shown in this figure were due to other impurities presented in the current experimental setup. The linear fits used to extract XRF signal are shown in addition to the 10th order polynomial fit applied to the Compton scatter used for correcting the signal.

The absorption of source and XRF photons within the phantom should be taken into account to accurately determine the amount of GNPs within the ROI. The degree of Compton scatter measured by the detector can be taken as an internal gauge of the attenuation properties of the sample and used to correct for self-absorption of XRF photons and also for attenuation of source photons as they travel through the sample [50]. Specifically, as implemented in previous XRF studies [38, 51], the signal from the Compton scatter peak is used to take the ratio of net XRF signal to Compton scatter to correct for attenuation:

$$P_{FS} = \frac{P_{net}}{P_C}$$

where P_{FS} is the corrected XRF signal, P_{net} is the net XRF peak signal and P_C is the Compton peak signal. This normalization corrects for loss of source photon fluence in the beam direction and also for in-phantom attenuation of XRF photons. This method takes advantage of the fact that the Compton scatter is approximately independent of the medium's Z in this energy range. In order to implement this technique, an empirical 10th order polynomial fit was applied to the entire Compton scatter background. This fit was used to generate the Compton peak signal P_C by adding the total signal in the energy windows containing the Compton peak. Note the Compton scatter background could alternatively be fit to at least a semi-empirical function reasonably accounting for the expected angular scatter profile of incident x-rays. Although not attempted in the current feasibility study, this approach may be pursued in future investigations.

3.2.5 Detection Limit Determination

The data from the calibration phantom measurements were used to generate a plot showing the corrected XRF signal as a function of GNP concentration. **Figure 3.2.5** shows the result of the calibration phantom measurements demonstrating the linearity ($r^2 = 0.9999$) between XRF signal and GNP concentration. The inset shows the data points at very low GNP concentrations: 0 (water), 0.005 and 0.05 mg/cm^3. As shown, no statistically significant XRF signals were detected from the water and 0.005 mg/cm^3 phantoms, suggesting that the detection limit of the system was somewhere between 0.05 and 0.005 mg/cm^3. The shaded region in the inset of **Figure 3.2.5** illustrates levels of signal that cannot be interpreted as true signal (at the 95% confidence level) above the background noise, σ_b. The intersection of the upper limit of the shaded region and the line of best fit represents the detection limit of the system, which was calculated to be ~0.35 μg of GNPs per imaged voxel within the calibration phantom. At such a low concentration of GNPs (0.02 mg/cm^3), the statistical noise blurs the XRF signal below the 95% confidence level (i.e., the signal would be less than $1.96\sigma_b$).

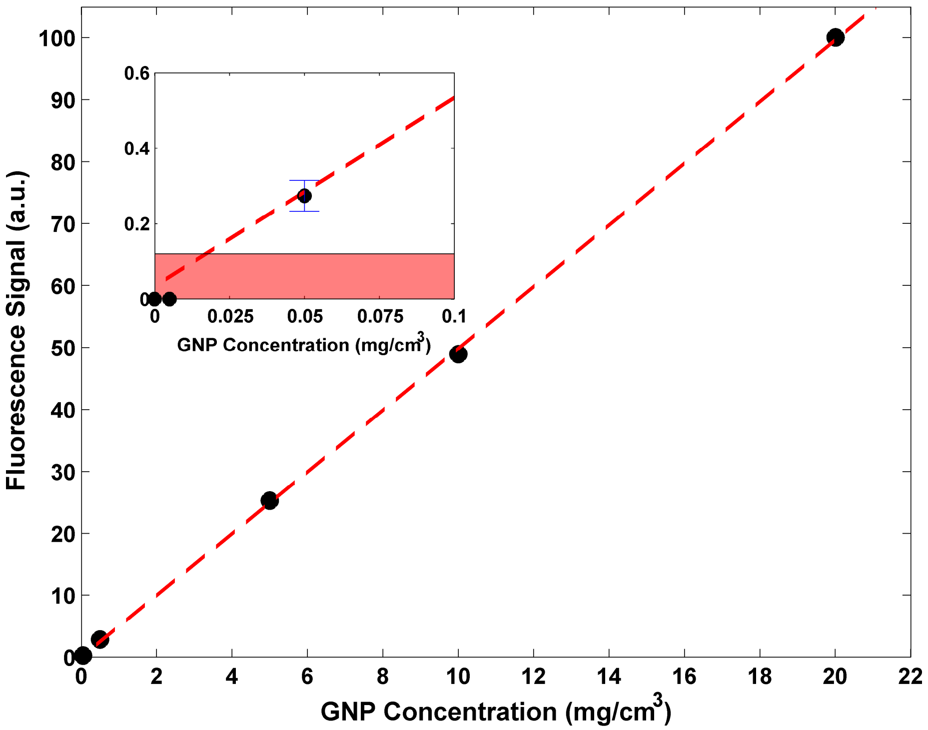

Figure 3.2.5 Calibration curve for determining the detection limit of the *L*-shell XRF system with the low-power x-ray source. The detection limit was found to be 0.02 mg/cm^3 (20 ppm). Data show a linear relationship between XRF signal and GNP concentration. The corresponding GNP mass per 1.73×10^{-2} cm^3 voxel for each data point (20, 10, 5, 0.5, 0.05, 0.005, and 0 mg/cm^3) was approximately 350, 175, 87.5, 8.75, 0.875, 0.0875, and 0 µg assuming uniform distribution of GNPs. Error bars for data points are much smaller than the size of the data symbols. (inset) The intersection of the best-fit line and the border of the shaded region highlights the detection limit of the system (GNP concentration of ~0.02 mg/cm^3, corresponding to ~0.35 µg of GNP within the 1.73×10^{-2} cm^3 voxel).

3.2.6 2D XRF Mapping of Imaging Phantom

In order to demonstrate the ability to image and quantify the amount of GNPs within the ROI, a 2D XRF map (**Figure 3.2.6**) was generated using the imaging phantom. Unlike the optical images shown in **Figure 3.2.3**, the varying GNP concentration within the phantom is apparent in this 2D XRF image. With the reasonable assumption that an imaging voxel containing a maximum GNP concentration of 20 mg/cm^3 would be responsible for the brightest pixel in the image, the estimated mass of GNPs within the ROI ranged from 0.5 to 5.5 μg per imaged voxel. Overall, the image shows a highly heterogeneous GNP distribution within the phantom, indicating diffusion of the injected GNP solution throughout the gel. The highest levels of GNPs were present around the central region of the mimicked tumor and the GNP concentration levels were at the lowest around the tumor periphery and the mimicked blood vessels.

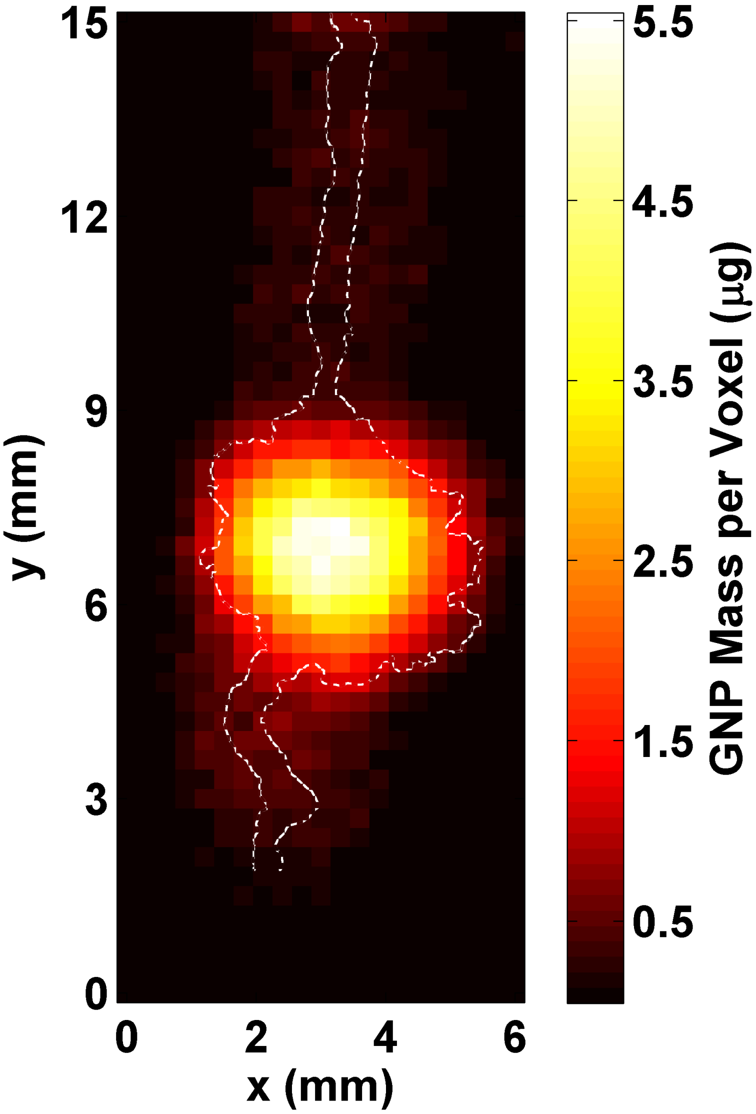

Figure 3.2.6 2D XRF map of GNPs within imaging phantom simulating a GNP-laden tumor and blood vessels. The GNP distribution (in mass per 2.70×10^{-4} cm^3 voxel) within the simulated tumor region and blood vessels is shown, with the maximum value of ~5.5 μg corresponding to a GNP concentration of 20 mg/cm^3. The outline of the irradiated GNP-containing structures is overlaid on the XRF map, showing that there was a reasonable match between the images around the tumor region whereas there was a worsening of the spatial resolution for low concentration regions (the simulated blood vessels) primarily due to increased uncertainty in XRF signal (i.e., insufficient data acquisition time).

3.3 Performance Increase of *L*-shell XRF Imaging System

In order to image and quantify the distribution of GNPs within an object (by translating the detector horizontally and vertically) with both high resolution (sub-millimeter) and high sensitivity (ppm level), the scanning time becomes prohibitively long. For example, while the original proof-of-principle *L*-shell XRF imaging system based on the low-power x-ray source was capable of detecting GNPs at concentrations as low as 0.02 mg/cm^3 (20 ppm) for an acquisition time of 10 minutes, it was not practical to perform the 2D mapping of the imaging phantom at such a lengthy acquisition time per 0.3 mm × 0.3 mm pixel (i.e., it was done at a shorter acquisition time of 30 s per pixel).

3.3.1 High-Power X-ray Source and Silicon Drift Detector

To address this obstacle, the experimental setup was revised by replacing the low-power x-ray source with a new high-power x-ray source (XRS-160, COMET Technologies USA, Inc.) with approximately 60 times the power (i.e., ~3 kW) when operated at 62 kVp and 45 mA. As the Si-PIN diode detector would become overloaded at such high photon flux, it was replaced by a silicon drift detector (SDD) (XR-100SDD, Amptek Inc.). The SDD can not only handle much higher count rates but is also capable of better energy resolution which would facilitate separation of the XRF peaks from background.

3.3.2 Detection Limit Determination

The detection limit with the current configuration was determined using the same analysis as with the low-power configuration, albeit with two changes in addition to the source and detector retrofits. First, calibration phantoms were prepared with lower concentrations of GNPs than before: 10, 5, 1, 0.1, 0.01, 0.001, 0.0001, and 0 mg/cm^3. The other change was that the acquisition time was set to 10 s, a factor of 60 shorter compared to the original configuration, in order to maintain approximately the same overall x-ray fluence and dose. Under these conditions, the detection limit was found to be 0.007 mg/cm^3 (7 ppm), a three-fold improvement; the calibration curve is shown in **Figure 3.3.1**. The detection limit was also determined for an acquisition time of 5 minutes and found to be 0.005 mg/cm^3 (5 ppm) and is shown in **Figure 3.3.2**.

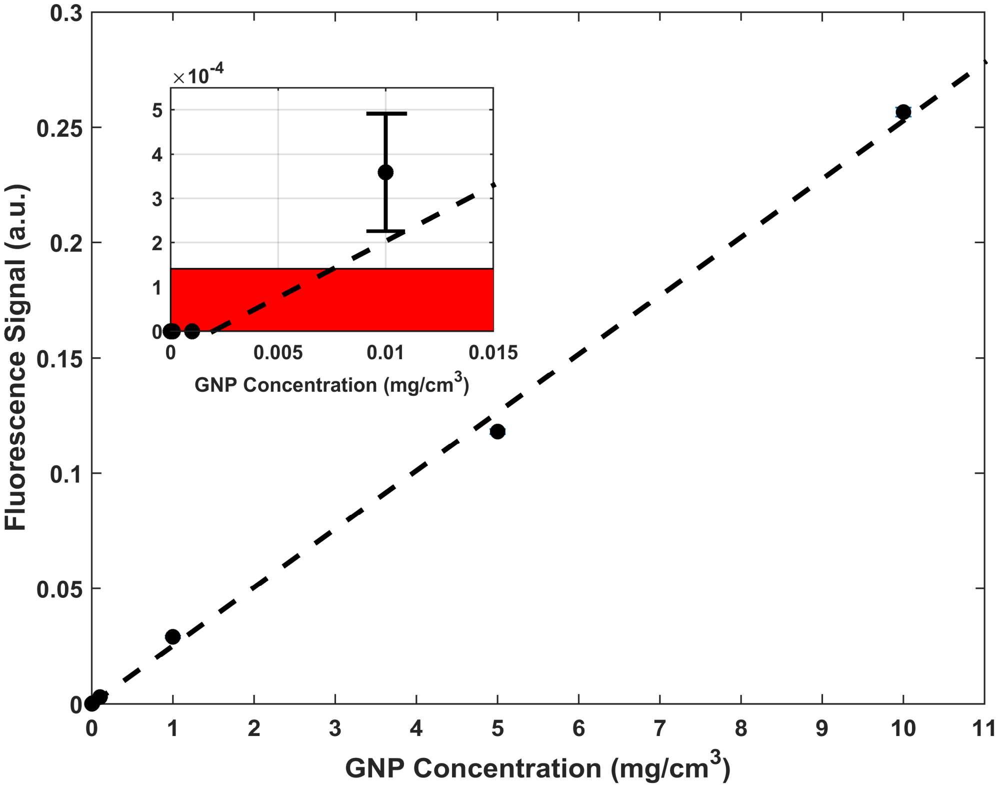

Figure 3.3.1 Calibration curve for determining detection limit of GNPs for the *L*-shell XRF system with high-power x-ray source for an acquisition time of 10 s. The detection limit was found to be 0.007 mg/cm^3 (7 ppm).

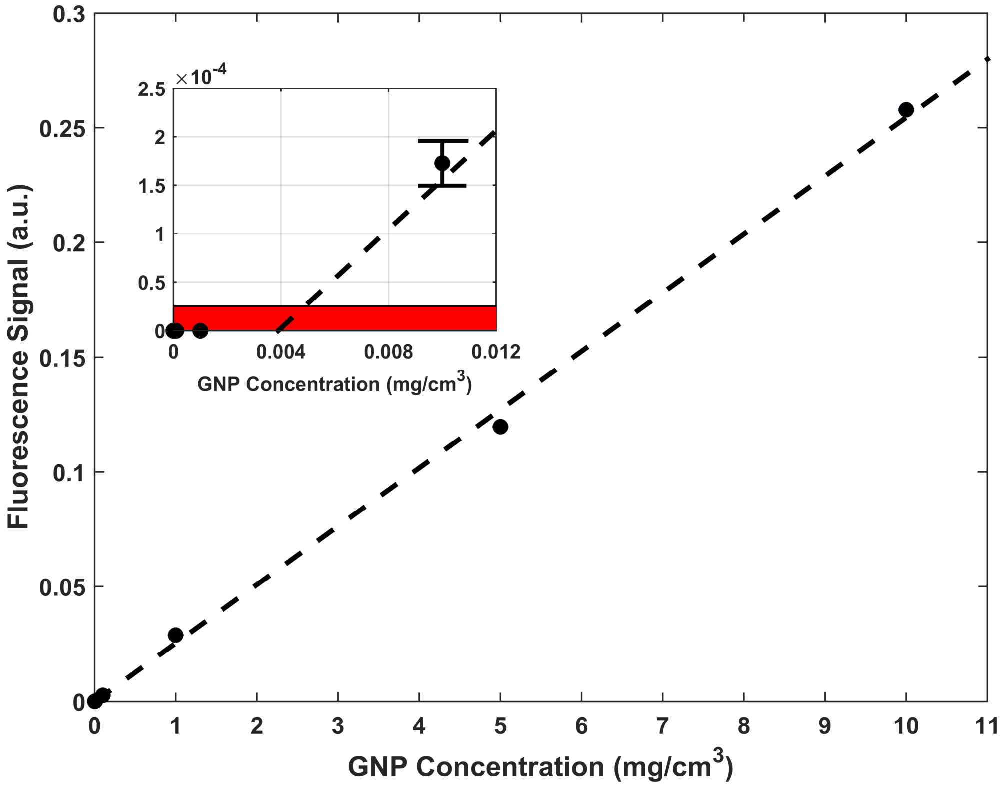

Figure 3.3.2 Calibration curve for determining detection limit of GNPs for the *L*-shell XRF system with high-power x-ray source for an acquisition time of 5 minutes. The detection limit was found to be 0.005 mg/cm^3 (5 ppm).

3.3.3 2D XRF Mapping of Calibration Phantoms

Characterization of the new configuration was performed by performing a 2D mapping of the 12-mm-diameter calibration phantoms. The phantoms were oriented vertically and a 14 mm × 14 mm ROI was imaged (1 mm horizontal buffer on each side of the phantom). The imaging step size was 1 mm for a total of 196 pixels. The acquisition time per pixel was 10 s for a total scan time of around 45 minutes per phantom including the overhead needed for stage translations. Noting that the entire diameter of the phantom was imaged, unlike previously when only a small portion in the center was imaged, an *a priori* attenuation correction using the attenuation coefficient of water for ~10-keV photons was applied. This was required to properly account for the wide range of path lengths, from the detector's perspective, due to the cylindrical shape of the phantom (i.e., the path length varied from ~0 to ~6 mm). After correction, the images showed a uniform distribution of GNPs for the calibration phantoms that were imaged. Dark pixels represent pixels for which either no signal was detected or the detected signal was not higher than 1.96 times the background noise; most of the dark pixels in the image of the 0.01 mg/cm^3 phantom (a concentration just above the detection limit of 7 ppm) were due to the latter.

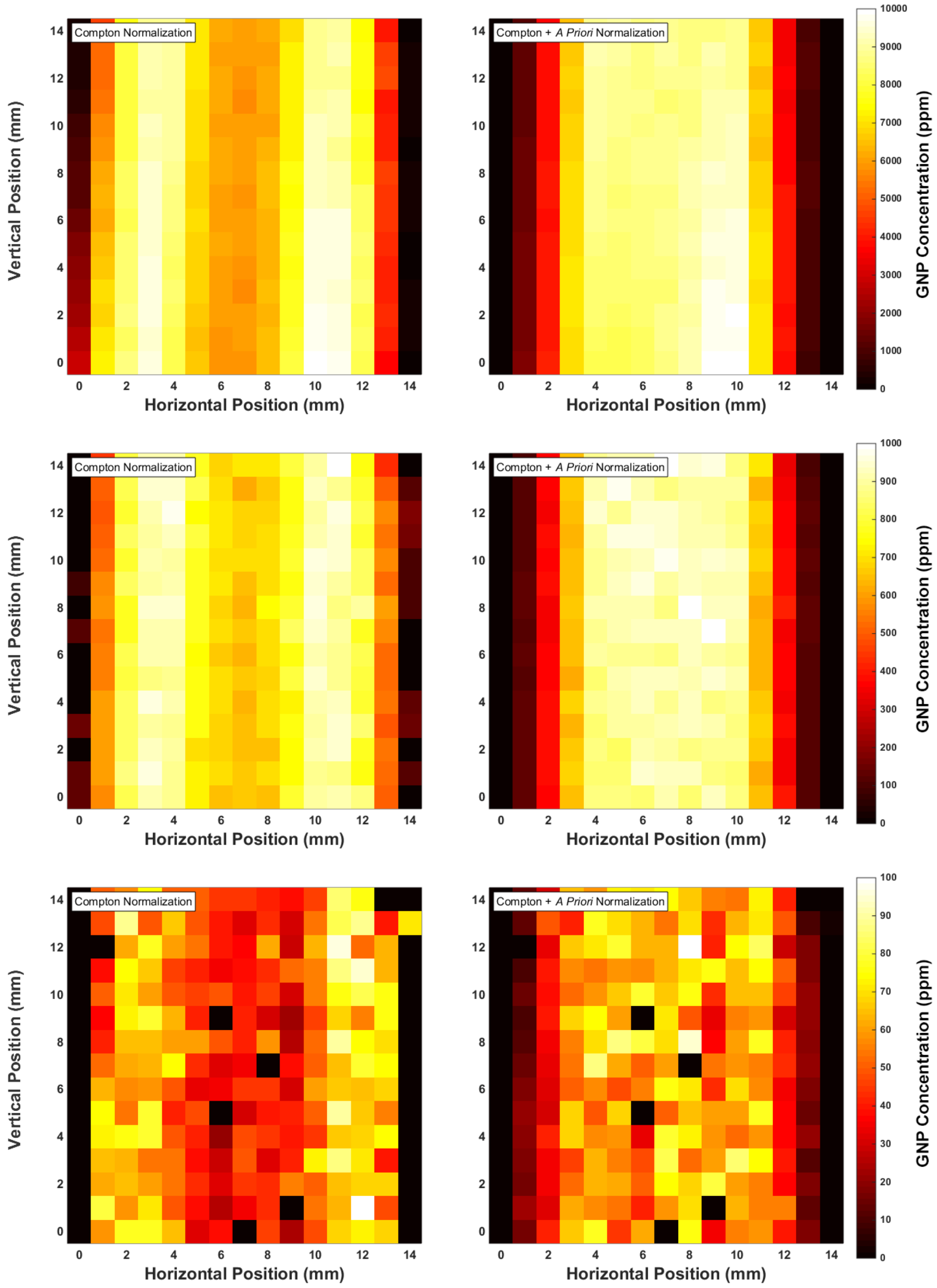
Compton Normalization
Compton + *A Priori* Normalization
Vertical Position (mm)
Horizontal Position (mm)
0
2
4
6
8
10
12
14
GNP Concentration (ppm)
10000
9000
8000
7000
6000
5000
4000
3000
2000
1000
0
1000
900
800
700
600
500
400
300
200
100
0
100
90
80
70
60
50
40
30
20
10
0

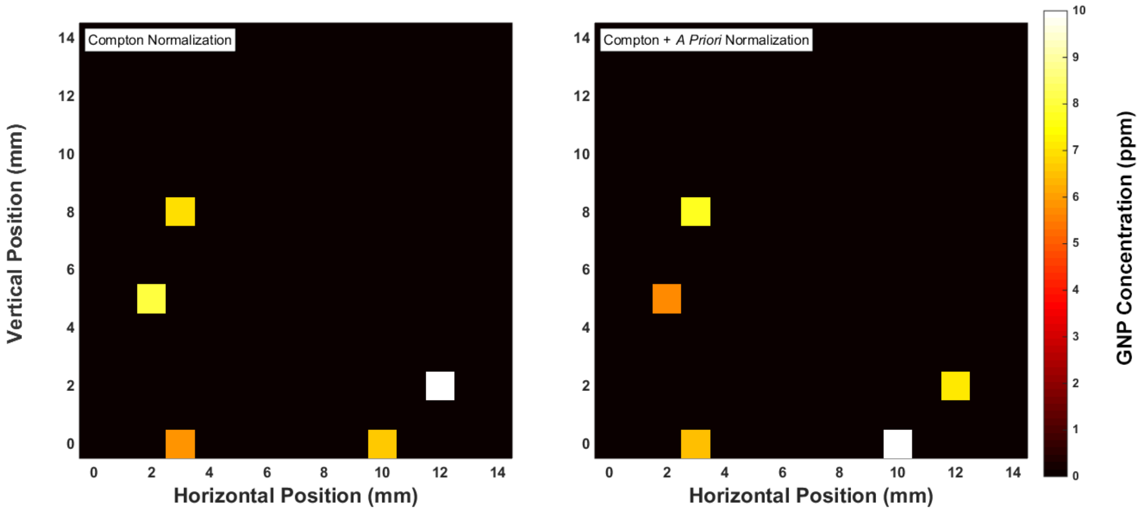

Figure 3.3.3 2D XRF maps of selected calibration phantoms. (top to bottom): 10, 1, 0.1, and 0.01 mg/cm^3 (1, 0.1, 0.01, and 0.001 wt. %). The GNP concentration within each image is quantified in ppm. Dark pixels represent pixels for which either no signal was detected or the detected signal was not higher than 1.96 times the background noise. The region of interest was 14 mm × 14 mm with a pixel size of 1 mm × 1 mm. Under these conditions, no signal was acquired when GNP concentration was below 0.01 mg/cm^3. Note that the scale bar is different for every set of images.

3.4 Discussion

Since its aim was to demonstrate only the feasibility, the initial investigation with the low-power source was performed with a somewhat restricted and preliminary imaging setup which had some room for further improvement with regard to scan time, detection limit, and image resolution. Subsequently, the adoption of the high-power x-ray source (and its factor of 60 higher photon flux) and the SDD (and its ability to process the higher flux, lower inherent noise, and improved energy resolution) were instrumental. Under the new conditions, the detection limit was found to be 0.007 mg/cm^3 (7 ppm) for an acquisition time of 10 s, ~3 times lower than the detection limit of the previous set-up (20 ppm) for the same overall x-ray fluence and dose in both cases. As the photon flux is now 60 times higher, a longer acquisition time can be used if tolerable to lower the detection limit even further (e.g., 5 ppm for an acquisition time of 5 minutes). All in all, considerably shorter imaging times can be expected while still taking advantage of increased sensitivity.

Tailoring of the incident x-ray spectrum via filtration can possibly improve the sensitivity even further. Alternatively, since it is relatively easy to create a low energy quasi-monochromatic x-ray beam (e.g., 10-20 keV) using various crystals, the incident x-ray source spectrum could be tailored to contain most of photons in the spectrum just above the *L*-edge of gold. Another potential issue hampering accurate localization of GNPs is the production of secondary XRF due to scattered photons. As mentioned before, a pencil-beam setup with tighter collimation can minimize this to a certain extent.

Clearly, this would almost completely eliminate the issue, as most of the scattered photons would have energies below the *L*-edge and would not be able to induce XRF production from GNPs. A smaller pencil-beam would improve image resolution and potentially lower the detection limit as well so long as it helps increasing the XRF signal-to-background ratio. The image resolution can also be improved by using detector collimation with a smaller aperture, although precise machining would be required. When pursuing optimization work such as these, it would be important to consider the interplay among scan time, detection limit, and image resolution.

Due to the nature of 2D planar imaging, as opposed to rotational CT, there are a few fundamental drawbacks that prevent the current experimental setup from accomplishing a more effective acquisition of some spatial information. To overcome these difficulties, a stereoscopic detection system may be implemented with two opposing detectors. That way, for example, the locations of XRF photon sources (i.e., GNPs) can be determined with better accuracy and efficiency, enabling the implementation of more sophisticated attenuation correction schemes for more precise quantification and imaging. To obtain more detailed images of the sample (e.g., 3D image), it is also technically feasible to perform a full XFCT scan of the sample using a cone-beam source without any considerable increase in the scan time [31] but at the expense of resolution, as opposed to pencil-beam-based direct XRF imaging.

L-shell XRF imaging, as shown in this study using a benchtop x-ray source, appears to be a feasible method for imaging and quantification of GNPs and also likely other high-*Z* probes (e.g., iodine, platinum, bismuth, etc.) presented in sub-centimeter-sized biological samples, offering orders of magnitude more sensitivity than its *K*-shell counterpart. Such an imaging system may offer advantages in various aspects (e.g., accessibility, imaging cost, sample handling, multiplexed imaging, etc.) over its synchrotron-based counterpart and/or other optical and x-ray imaging tools.

CHAPTER 4
COMPUTATIONAL INVESTIGATIONS OF NANOSCOPIC DOSE ENHANCEMENT

4.1 Background and Objective

Once GNP distributions are imaged and quantified, calculating the nanoscopic dose enhancement due to the presence of GNPs can reveal important information and can hopefully be used to predict biological outcomes. In spite of a recent computational study [52], there is still a lack of understanding, in many aspects, of the dose enhancement on a nanoscopic or subcellular scale. This research aimed to quantify, in particular, the dose enhancement characteristics around GNPs using computational methods.

4.2 Nanoscopic Dose-Point Kernels

Other researchers have performed macroscopic dose enhancement simulations using the EGSnrc code [53], simulating a tumor loaded with gold (0.7 wt. %) irradiated by various photon spectra (e.g., Yb-169, 250 kVp, 6 MV, etc.) [16]. Subsequently, using a modification to EGSnrc, they have separately extracted the average secondary electron spectra originating from gold atoms and water molecules to perform microscopic dose enhancement calculations [52, 54]. Since the computations were done for a gold concentration of 0.7 wt. %, a correction (multiplicative factor) was applied to account for the abundance of water molecules as compared to gold atoms; at this concentration, there are approximately 142 times as many water molecules as there are gold atoms. The corrected spectra represent the average number of electrons of each energy that originate from a single gold atom or water molecule, per photon, when irradiated by a particular spectrum. In this work, the resulting secondary electron spectra for Yb-169, 250 kVp, and 6 MV photon sources [44, 55] were imported and used for further analyses. The fact that gold atoms are more efficient than water molecules at producing secondary electrons is evident by the higher total number of secondary electrons per incident photon, as shown in **Table 4.2.1**. Also, the lower energy photon sources are more effective at producing secondary electrons, as expected due to the larger photoelectric interaction cross sections of lower energy photons.

Table 4.2.1 Ratio of number of secondary electrons produced in a gold atom to that produced in a water molecule when irradiated by photons of each source (Yb-169, 250 kVp, and 6 MV).

Photon Source	**Ratio of Number of Secondary Electrons Produced in Gold Atom vs. Water Molecule**
Yb-169	70.3
250 kVp	69.8
6 MV	4.47

4.2.1 Dose-Point Kernels from NOREC

Following the existing methodology, these secondary electron spectra, assumed to represent a point source of electrons, were input into the NOREC code [56] to compute the radial energy deposition per source electron in an infinite, homogeneous medium of water. The energy deposition per incident photon was recorded up to a distance of 30 μm, in 1-nm-thick spherical shells, for each electron spectrum. Noting that NOREC is only capable of simulating electrons up to a maximum energy of 1 MeV, the 6 MV spectra were truncated at 1 MeV. Since the results were output per source electron, they were multiplied by the total number of secondary electrons per photon for each material (water or gold) to obtain the energy distribution per incident photon. Division by the mass of each scoring shell yielded the relative dose-point kernels (DPKs) [57], which represent the dose at any point as a function of its radial distance from the point source of electrons.

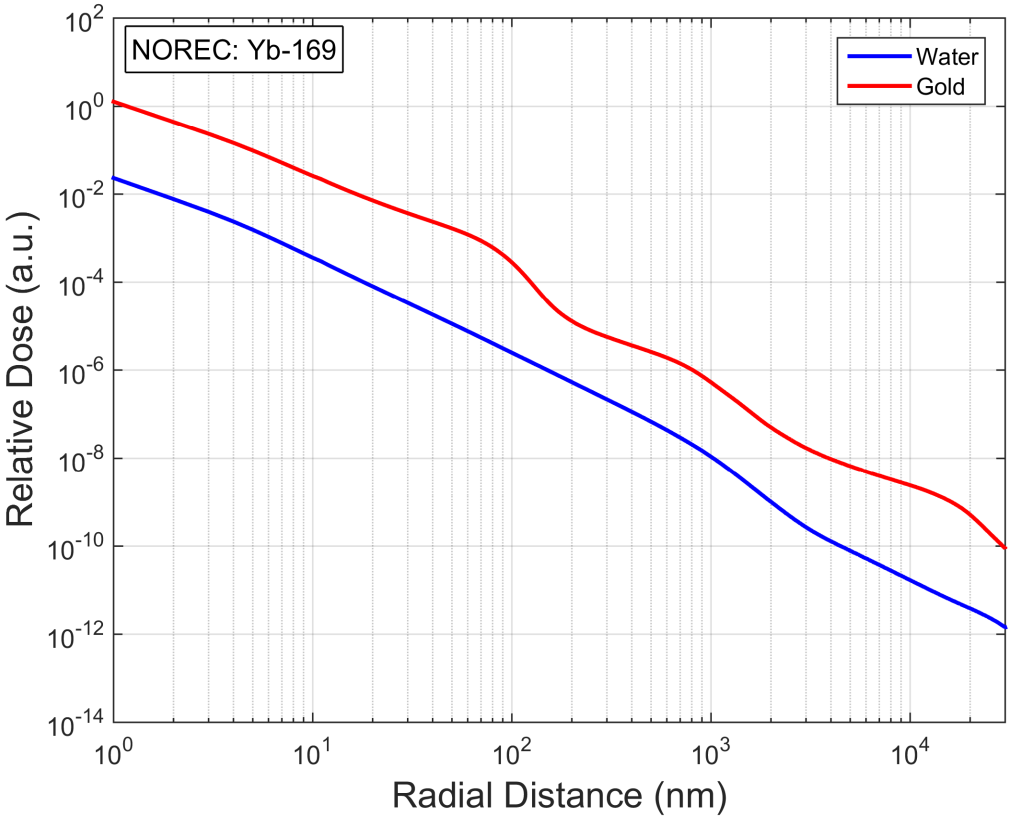

Figure 4.2.1 Nanoscopic DPKs (from NOREC) around a water molecule and a gold atom when irradiated by an Yb-169 photon source.

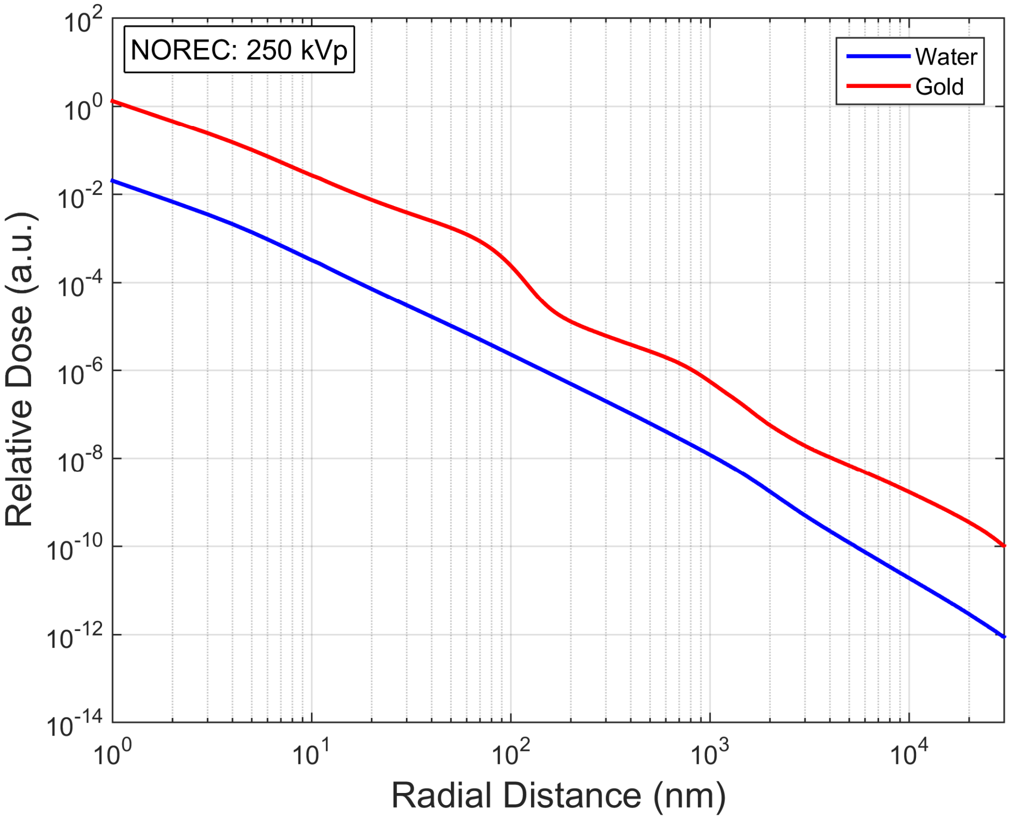

Figure 4.2.2 Nanoscopic DPKs (from NOREC) around a water molecule and a gold atom when irradiated by a 250 kVp photon source.

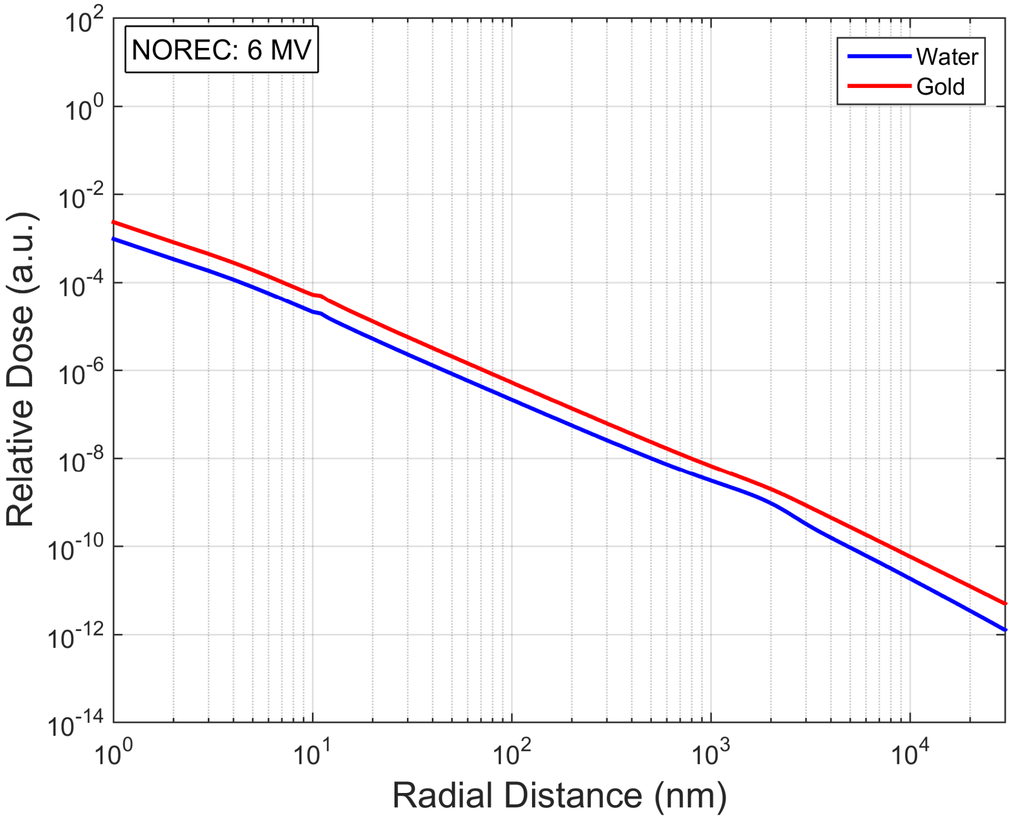

Figure 4.2.3 Nanoscopic DPKs (from NOREC) around a water molecule and a gold atom when irradiated by a 6 MV photon source.

4.2.2 Dose-Point Kernels from Geant4

The Geant4 toolkit [58] is a very powerful and versatile software package capable of simulating the passage of particles through matter. The Geant4-DNA project [59] is an extension of Geant4 that allows event-by-event (detailed history) physics treatment and other simulations at the nanoscale realm. It includes cross-sections for very low-energy physics in liquid water. Particularly for electron transport in liquid water, it is capable of simulating elastic scattering from 7.4 eV to 1 MeV, electronic excitation from 9 eV to 1

MeV, ionization from 11 eV to 1 MeV, vibrational excitation from 2 to 100 eV, and attachment from 4 to 13 eV.

A custom user application was written to be used with the Geant4 toolkit to replicate the dose calculations performed with NOREC for point sources of electrons in liquid water. A hybrid physics list was devised that allowed the Geant4-DNA physics to be used for event-by-event transportation of electrons below 1 MeV in liquid water and the built-in condensed history PENELOPE low-energy physics cross sections to be used for electron energies higher than 1 MeV. An isotropic point source of electrons was placed at the center of a 110-μm-radius sphere of liquid water (the world volume). The radial dose distribution was scored in spherical shells of 1 nm thickness up to a maximum radius of 30 μm for each of the electron spectra detailed earlier. The number of particle histories simulated was 2×10^5 for each case with a computational time of approximately 72 hours each for the Yb-169 and 250 kVp simulations and almost 1 week for the 6 MV simulations on a consumer-grade workstation with an Intel Xeon 8-core processor. As with the NOREC results, these results were multiplied by the total number of secondary electrons per photon for each material (water or gold) to first obtain the energy deposition per incident photon and subsequently, the DPKs.

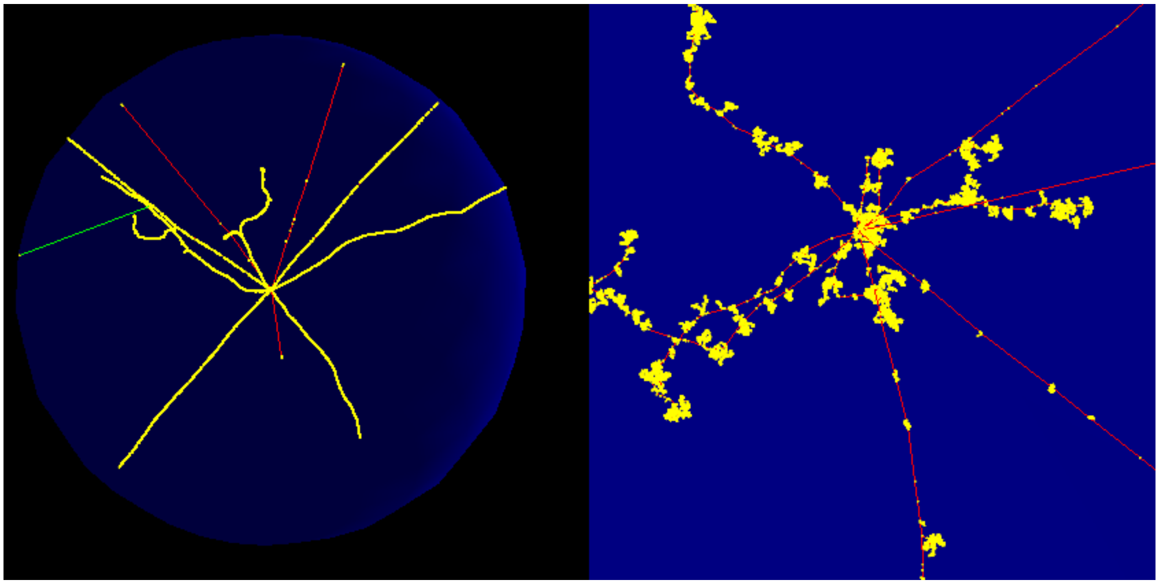

Figure 4.2.4 Exemplary visualization of nanoscopic simulations performed in Geant4 for point sources. (left) Top-level view showing entire scoring volume. (right) Highly zoomed-in view showing detail of event-by-event particle tracking. Red tracks are electrons, green tracks are photons, and yellow points are interaction sites. Approximately 10 electron histories are shown originating from a point source.

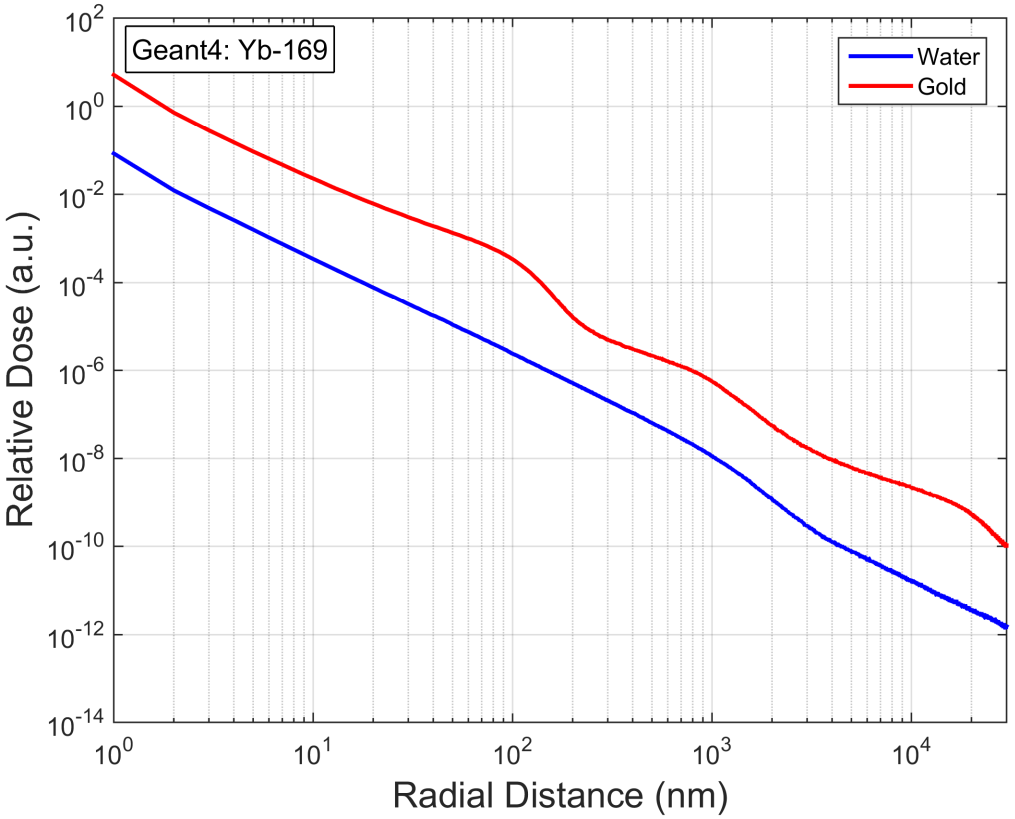

Figure 4.2.5 Nanoscopic DPKs (from Geant4) around a water molecule and a gold atom when irradiated by an Yb-169 photon source.

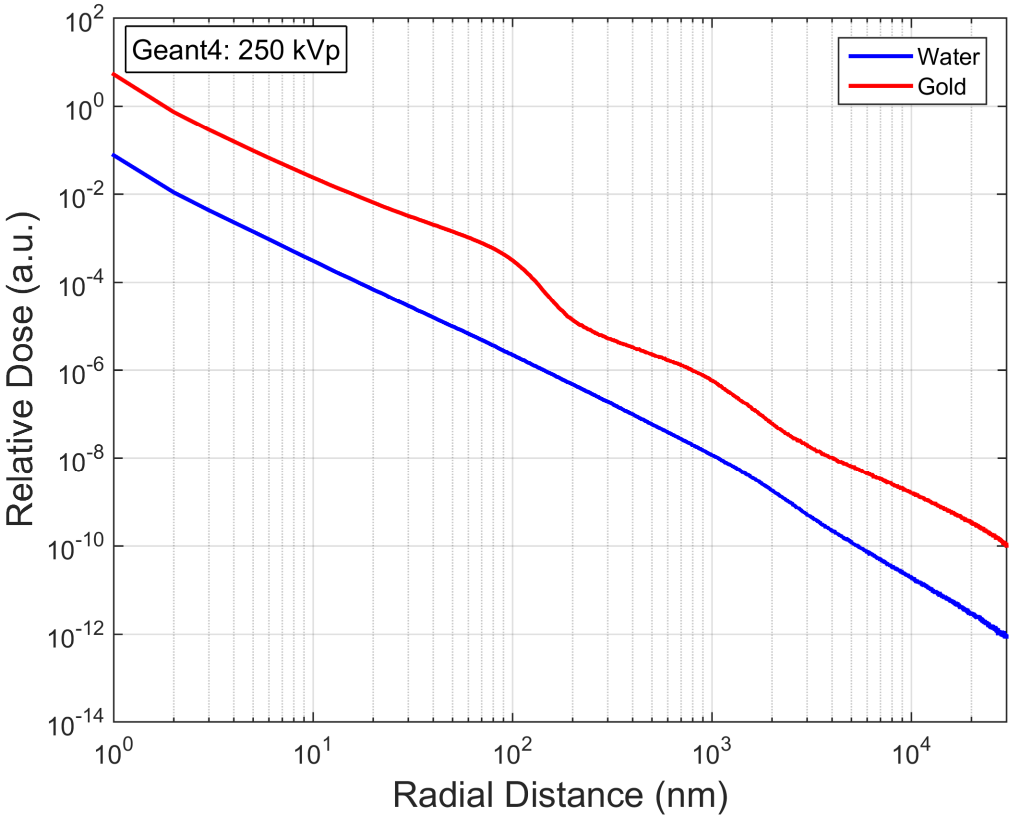

Figure 4.2.6 Nanoscopic DPKs (from Geant4) around a water molecule and a gold atom when irradiated by a 250 kVp photon source.

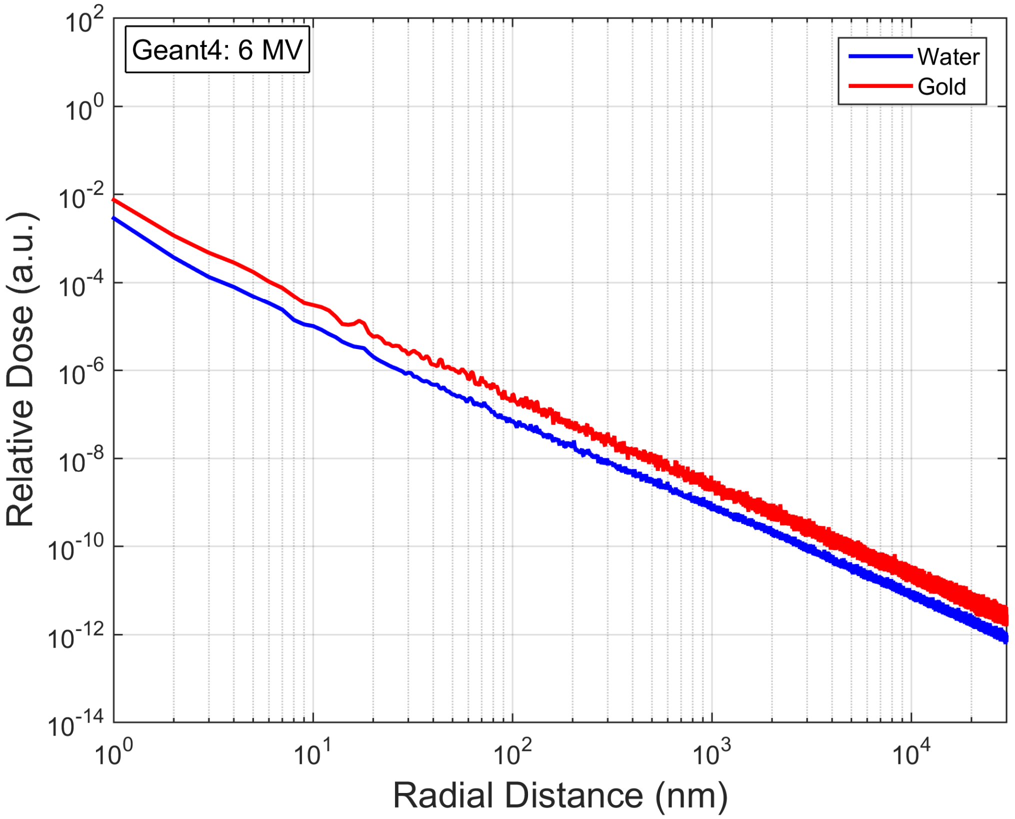

Figure 4.2.7 Nanoscopic DPKs (from Geant4) around a water molecule and a gold atom when irradiated by a 6 MV photon source.

4.2.3 Benchmarking of Geant4 Results

The results from Geant4 were compared against the NOREC results for benchmarking. Although there were minor variations between the NOREC- and Geant4-calculated DPKs, especially at scoring radii close to the point sources, the results matched remarkably well for all other data points. The Pearson product-moment correlation (*r* value) was computed for each pair of results and was very close to 1 for all of them, implying an excellent correlation.

Table 4.2.2 Pearson product-moment correlation coefficient between dose-point kernels obtained from NOREC and Geant4.

Photon Spectrum	Correlation Coefficient (*r*)	
	Water DPK	Gold DPK
Yb-169	0.9755	0.9685
250 kVp	0.9742	0.9687
6 MV	0.9632	0.9711

4.3 Nanoscopic Dimensional Dose Kernels

As the Geant4 calculations were found to match well with NOREC results, the user application was taken to be a valid model that can be used for further computational work. Therefore, the geometry in the user application was modified to simulate GNPs with dimensional extent rather than point sources of electrons. Spheres of either gold or water representing GNPs or hypothetical water nanoparticles (WNPs) of various radii (13, 25, 50, and 1000 nm) were modeled. While cylinders/rods and other shapes could be modeled, the symmetry of the situation, especially considering random orientations of such nanoparticles, could allow them to be represented using equivalent spheres of appropriate radii.

For each case, the point source of electrons was replaced by a spherical volume source with the same radius as the nanoparticle within which it was embedded. The sources were uniformly and randomly sampled, and set to emit electrons isotropically. As Geant4-DNA cross sections were only available for liquid water, a region-selective algorithm was incorporated into the hybrid physics list; specifically, in addition to the features of the list described earlier, the built-in PENELOPE low-energy physics models were used for any gold regions. For each simulation, the radial dose distribution was scored in water up to 30 μm, once again in 1-nm-thick spherical shells. The results were plotted as a function of radial distance from the center of each nanoparticle. The same number of histories were run for these simulations as for the point source simulations; the computational times were marginally longer for these simulations.

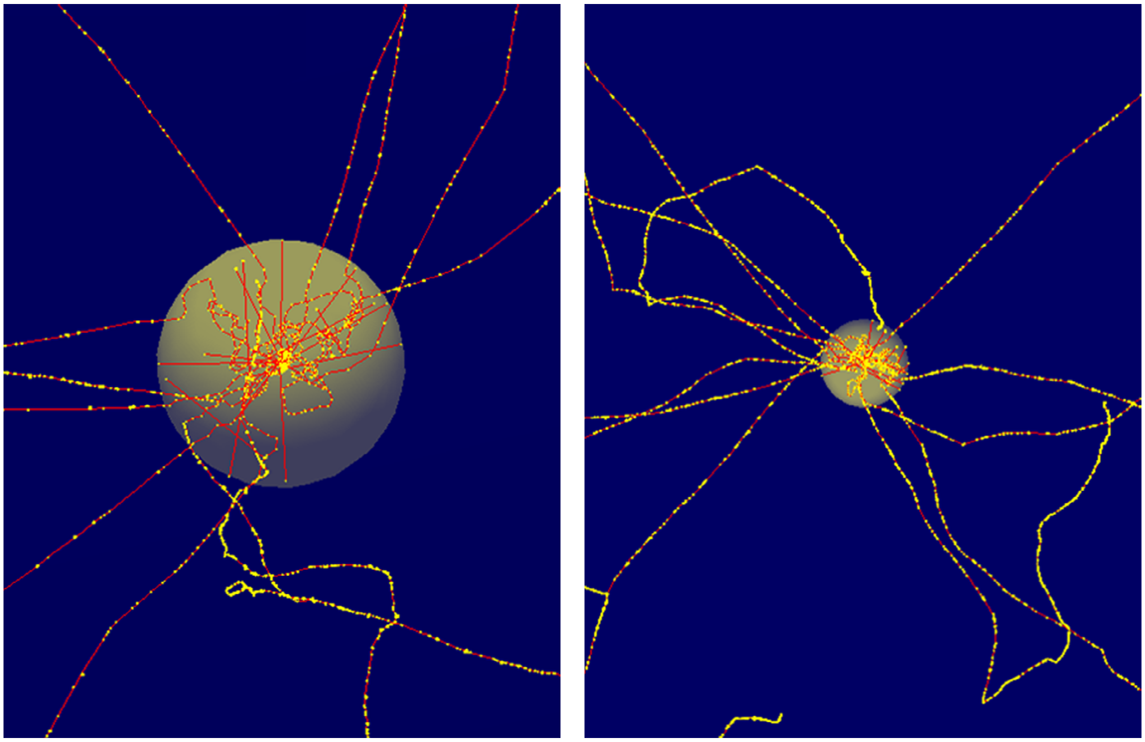

Figure 4.3.1 Exemplary visualizations of nanoscopic dimensional simulations performed in Geant4 for GNPs. Approximately 10 electron histories are shown with the electrons originating within the GNPs (volume sources).

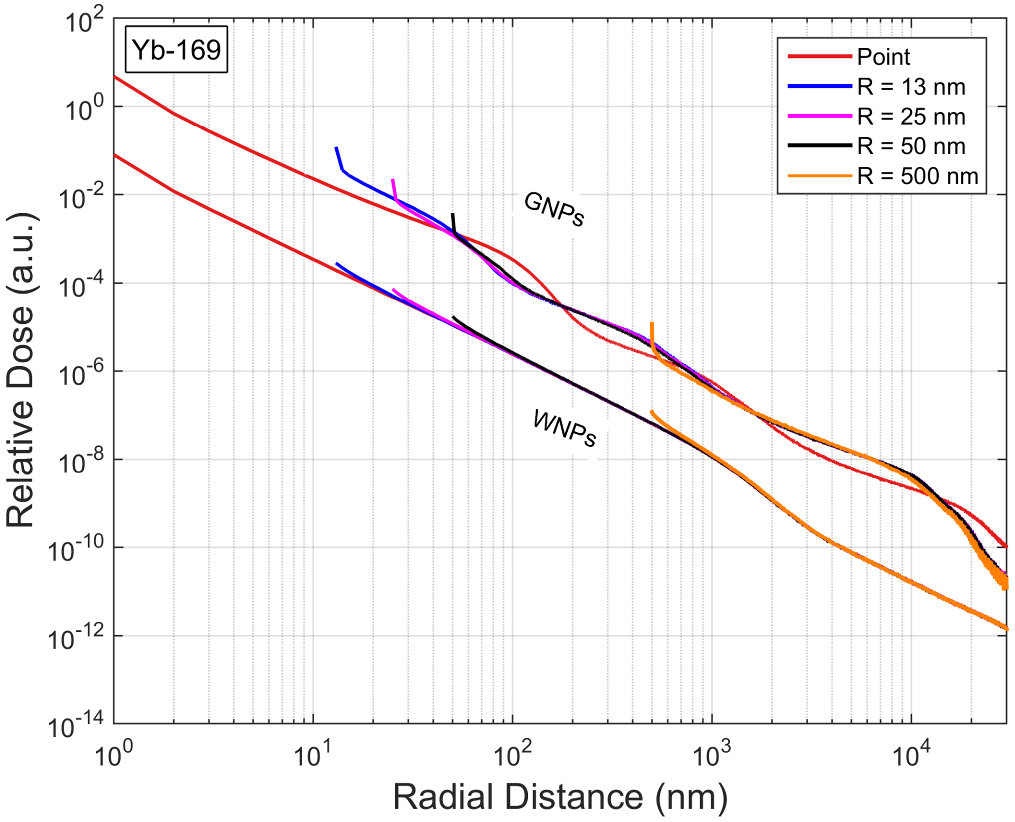

Figure 4.3.2 Nanoscopic dimensional dose kernels around WNPs and GNPs when irradiated by a Yb-169 photon source.

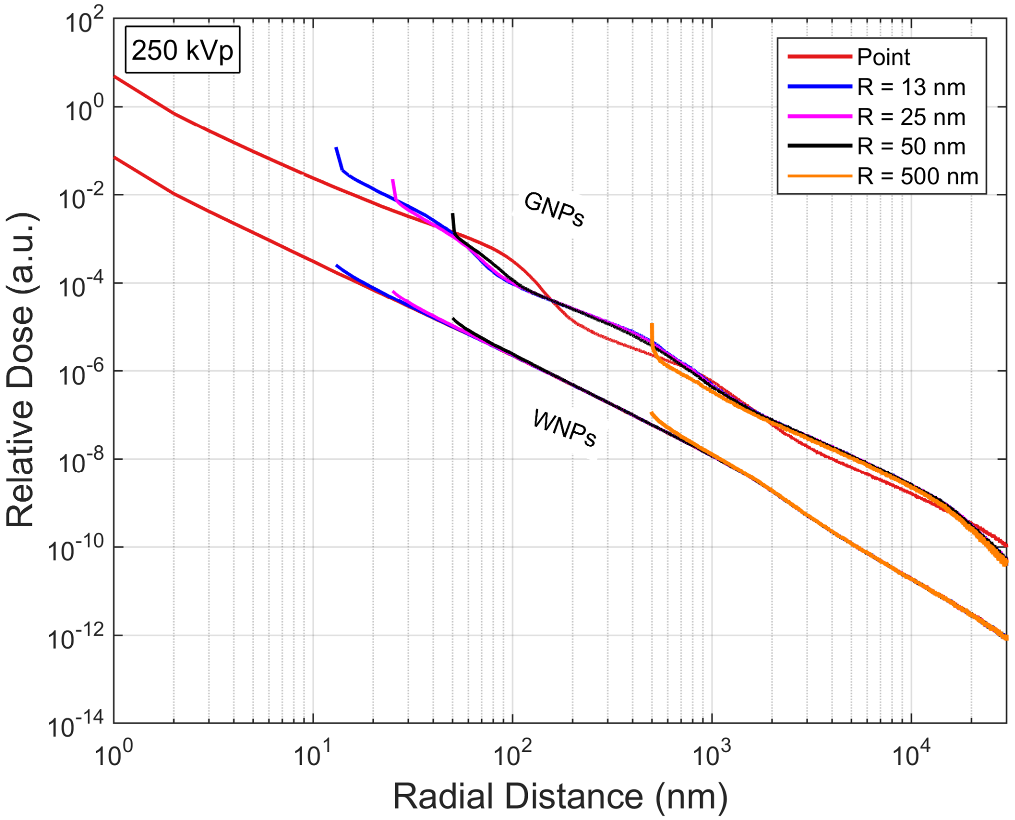

Figure 4.3.3 Nanoscopic dimensional dose kernels around WNPs and GNPs of various radii when irradiated by a 250 kVp photon source.

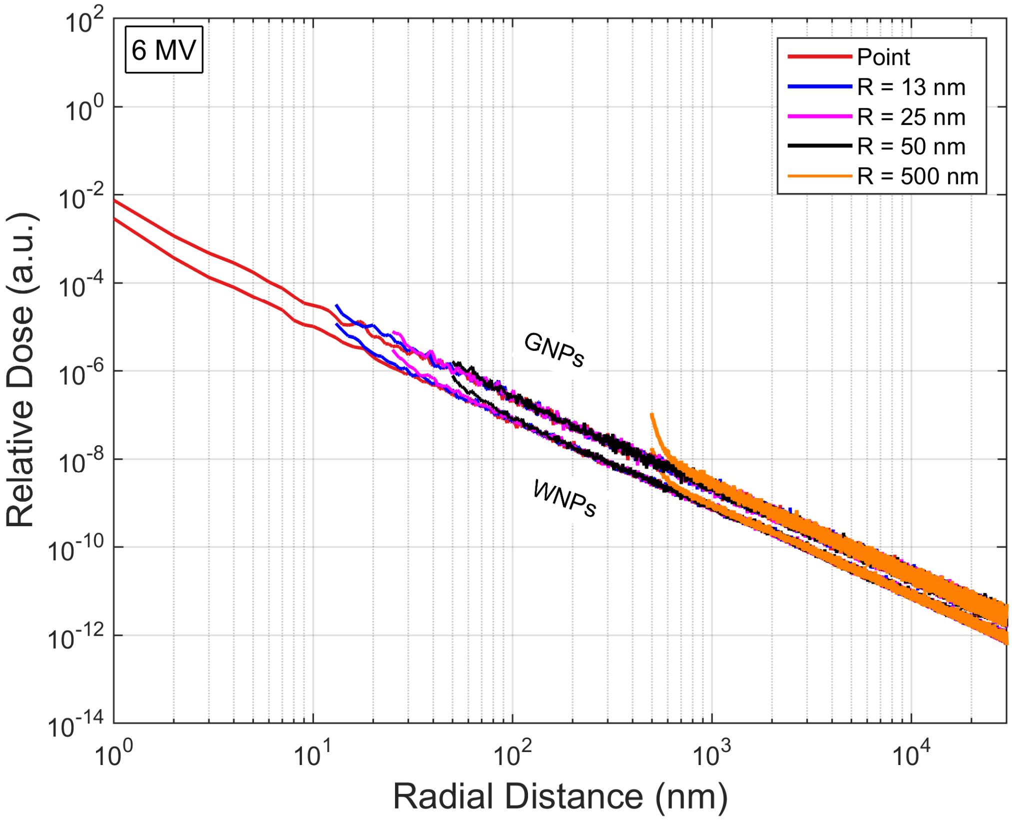

Figure 4.3.4 Nanoscopic dimensional dose kernels around WNPs and GNPs when irradiated by a 6 MV photon source.

4.4 Nanoscopic Dose Enhancement Factors

A nanoscopic dose enhancement factor (nDEF) was computed for the Geant4-generated DPKs and dimensional dose kernels by taking the ratio of the gold dose kernels to the water dose kernels. The nDEF represents the increase in dose deposition, as a function of distance, conferred by replacing a hypothetical WNP with a GNP.

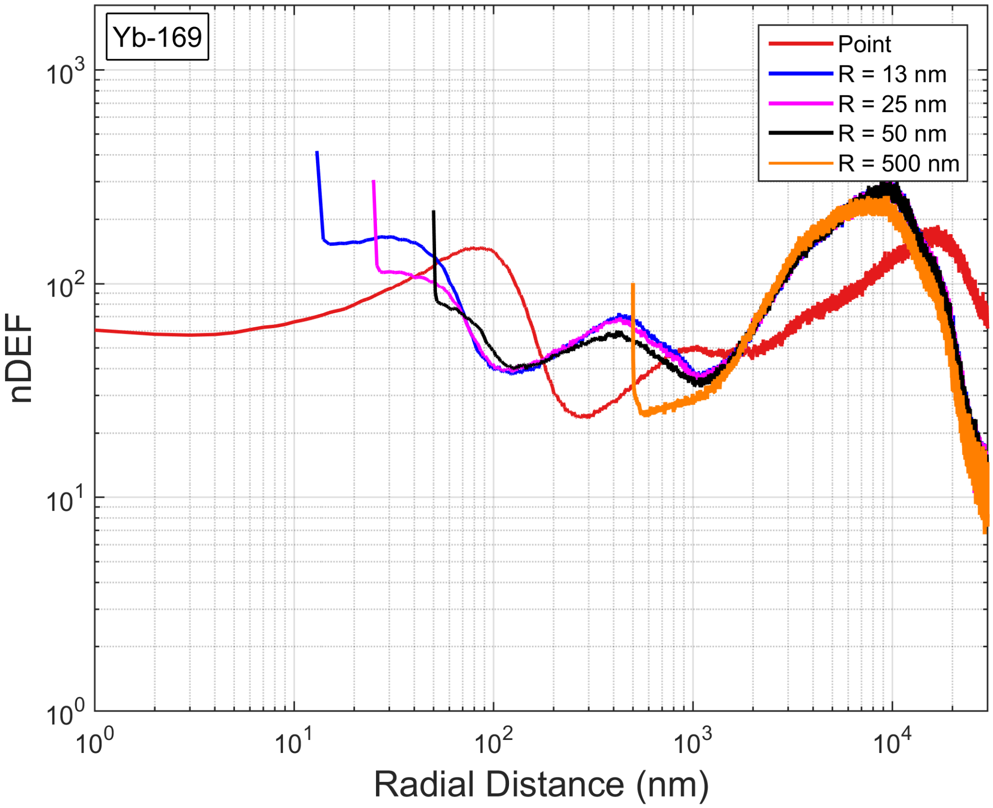

Figure 4.4.1 Corresponding nanoscopic dose enhancement factors for the Yb-169 photon source.

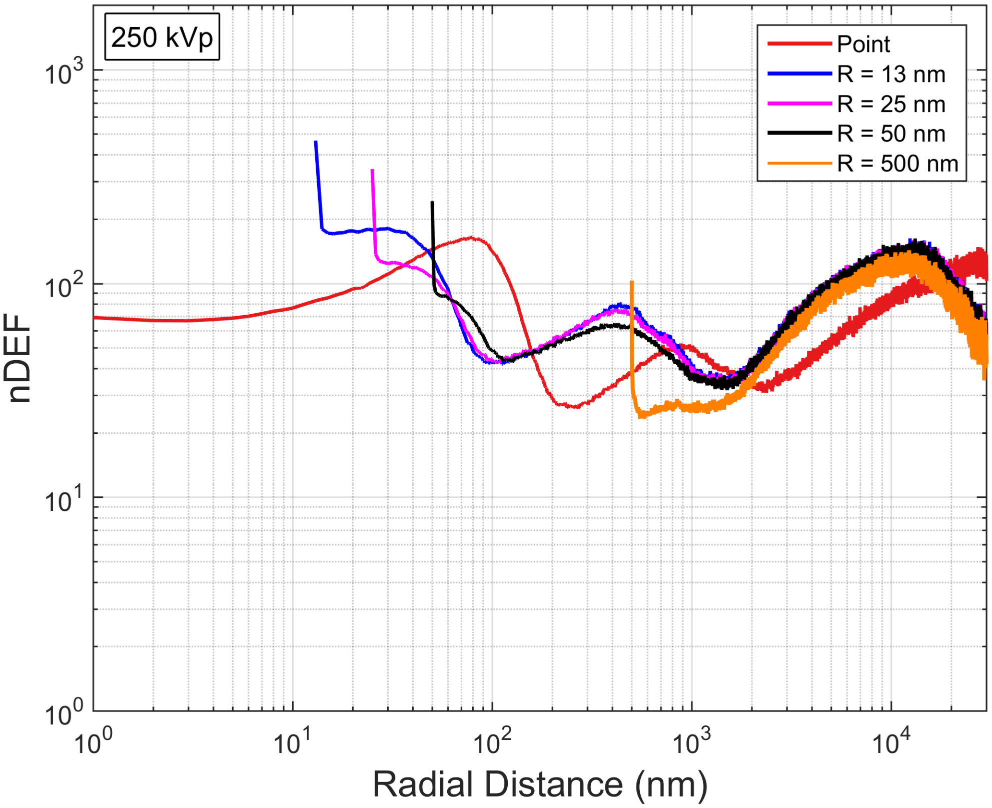

Figure 4.4.2 Corresponding nanoscopic dose enhancement factors for the 250 kVp photon source.

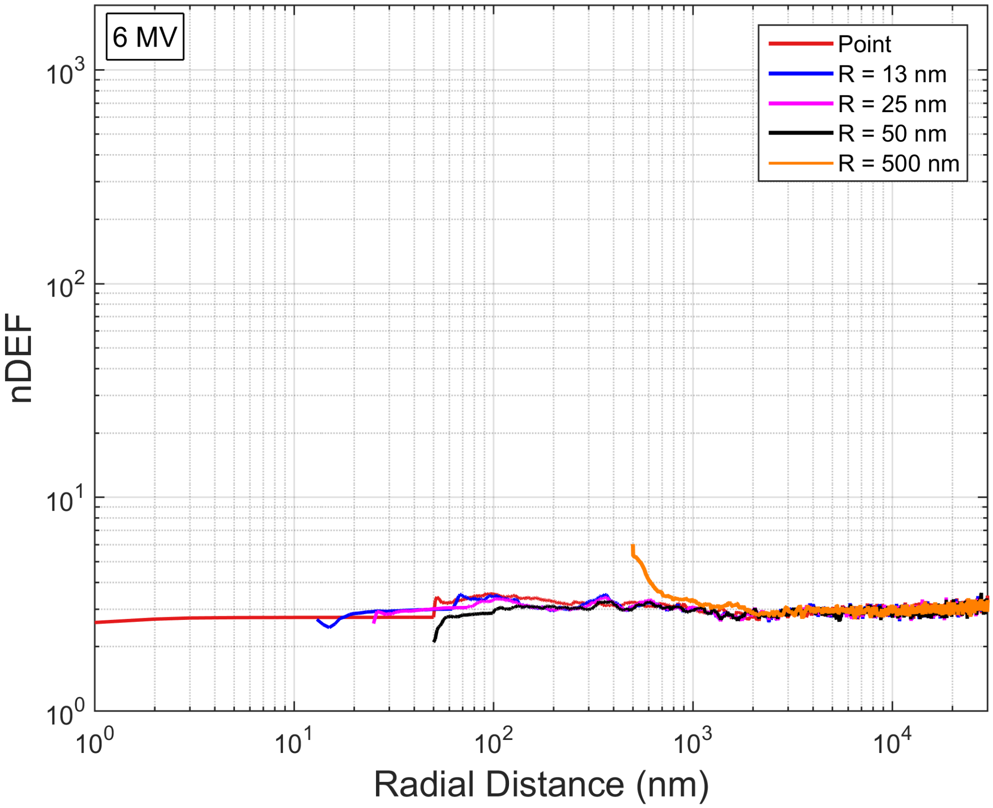

Figure 4.4.3 Corresponding nanoscopic dose enhancement factors for the 6 MV photon source.

4.5 Development of Dose-Point Kernel Scaling Methods

Rather than calculating the dimensional dose kernels for every nanoparticle shape and size, it would be convenient to develop a method of appropriately scaling the DPKs [60] to approximate heterogeneous situations. First a scaling must be applied to account for the dimensionality of the problem (*viz.* "volumetric scaling"). Subsequently, scaling can be applied to account for dose calculations in heterogeneous media (*viz*. "material scaling").

4.5.1 Volumetric Scaling

A nanoparticle of finite size can be represented as a volume source, which itself can be represented as a properly-sampled distribution of point sources. As source points would no longer be located exclusively at the origin, analytical geometry must be used for each source point and scoring point combination to calculate the physical path length. Let $\boldsymbol{P}_0 = (x_0, y_0, z_0)$ be the coordinates of a point (uniformly and randomly sampled) inside a spherical nanoparticle of radius R. Let $\boldsymbol{P}_S = (x_S, y_S, z_S)$ be the coordinates of a scoring point outside the nanoparticle. For any pair of source and scoring point, the physical path length ($PL_{Physical}$) is simply the distance between $\boldsymbol{P}_0$ and $\boldsymbol{P}_S$ given by:

$$PL_{Physical} = \sqrt{(x_S - x_0)^2 + (y_S - y_0)^2 + (z_S - z_0)^2}$$

The generation of source points, scoring points, and calculation of physical path lengths was implemented as a function in MATLAB (Version R2014b, The MathWorks, Inc.) and was applicable to all dimensional WNPs and GNPs. Once the path length is determined, it can be used to integrate the dose contribution to each scoring shell using the DPK for each of the randomly and uniformly sampled points within a dimensional nanoparticle.

4.5.2 Material Scaling

In addition to volume scaling, an additional scaling method must be applied to the gold DPKs to generate the dimensional dose kernels for gold. Considering an example where a point source of electrons in water is compared to the same source embedded within an object of higher Z or density, the dose distribution outside the object would presumably be different due to absorption and other interactions of the electrons with the object as they traverse it. The calculation of the distance traversed through the nanoparticle, denoted $PL_{Nanoparticle}$, was also implemented into the MATLAB function. Along the path from $\boldsymbol{P}_0$ to $\boldsymbol{P}_S$, there exists a unique point $\boldsymbol{P}_R = (x_R, y_R, z_R)$ on the surface of the nanoparticle, satisfying the relation ${x_R}^2 + {y_R}^2 + {z_R}^2 = R^2$. Noting the collinearity of the three points, a system of equations can be set-up and solved analytically using the quadratic formula for the physically valid solution of $\boldsymbol{P}_R$. It follows that $PL_{Nanoparticle}$ is the distance between $\boldsymbol{P}_0$ and $\boldsymbol{P}_R$ given by:

$$PL_{Nanoparticle} = \sqrt{(x_R - x_0)^2 + (y_R - y_0)^2 + (z_R - z_0)^2}$$

In this example, the stopping power (and the closely related linear energy transfer) of the electron should be higher in the object as compared to water. Therefore, it can be assumed that traversing a certain distance through the object is equivalent to a much longer linear distance in water (*viz.*, a “modified path length”). Subsequently, for the case of two materials such as water and gold as in the current investigation, the modified path length can be computed using the following relation:

$$PL_{Modified} = PL_{Physical} + PL_{Nanoparticle} \times (SF - 1)$$

where $PL_{Modified}$ is the modified path length, $PL_{Physical}$ is the physical distance between the source point and the scoring point, $PL_{Nanoparticle}$ is again the distance traversed through the nanoparticle, and SF is a multiplicative scaling factor between the nanoparticle material (in this example, gold) and the material of the scoring volume (water). Note that when the nanoparticle and scoring volume are made of the same material, the scaling factor becomes unity and the modified path length is equal to the physical path length. Once the modified path length is calculated, the dose at a particular scoring point can be estimated by evaluating the DPK at the modified path length rather than the physical path length.

Two of the most common scaling factors are range ratio and physical density ratio [61, 62]. The concept of range-ratio scaling attempts to account for the energy-dependent stopping power of electrons [61]. In this method, the ratio of the continuous slowing-down approximation (CSDA) electron range [63] between a material of interest and water at a certain energy is used to scale the path length traversed through the material. In effect, the distance the electrons travel through a material is equivalent to the distance in water multiplied by the range ratio between the two materials. As an alternative to range-ratio scaling, the physical density ratio scaling method could have been used which uses the ratio of the physical densities of the two materials to calculate the extended path length within a material. For example, in the case of water and gold, the scaling ratio is ~19.32. While this is a straightforward way of scaling, it does not have any energy-dependence and may therefore be more inaccurate.

4.5.3 Scaling for Water Dose-Point Kernels

Note that no material-based scaling is required for the water DPKs as the geometry is homogeneous. Therefore, the only scaling applied was the volumetric scaling. The results matched the Geant4 simulation results quite well, allowing the MATLAB volumetric scaling function to be validated.

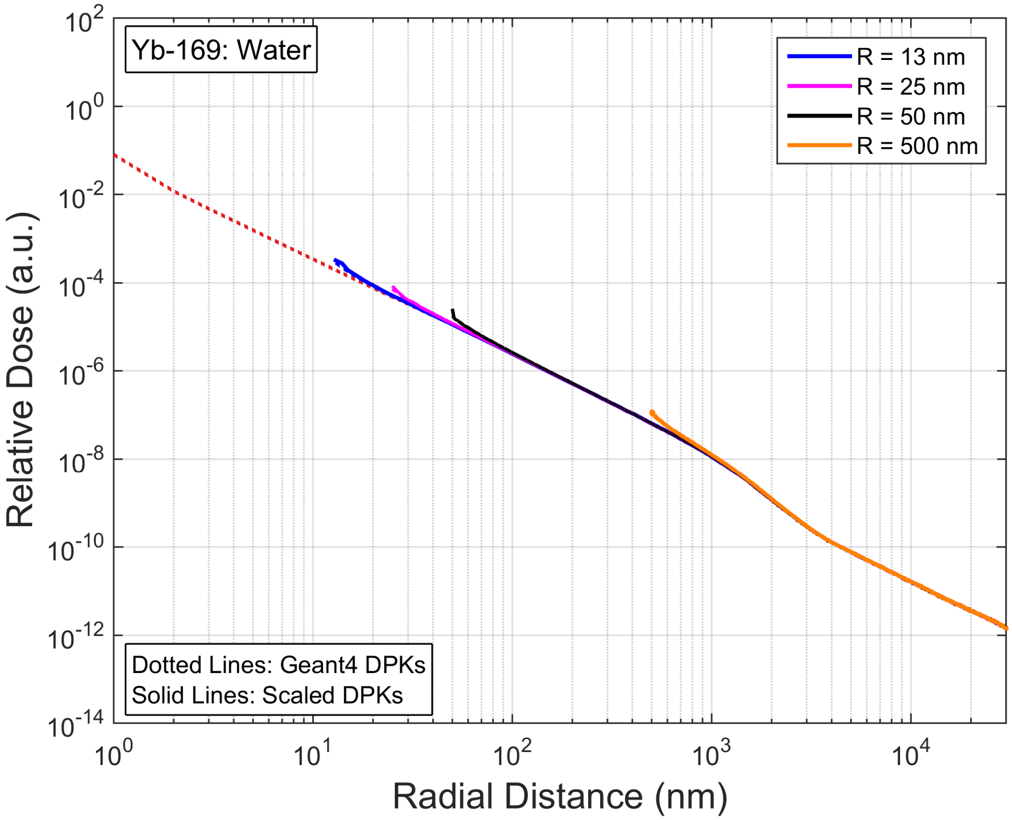

Figure 4.5.1 Volumetric scaling of DPK for WNPs of various dimensions for the Yb-169 source. The red dotted line denotes the DPK that was used as the basis for scaling.

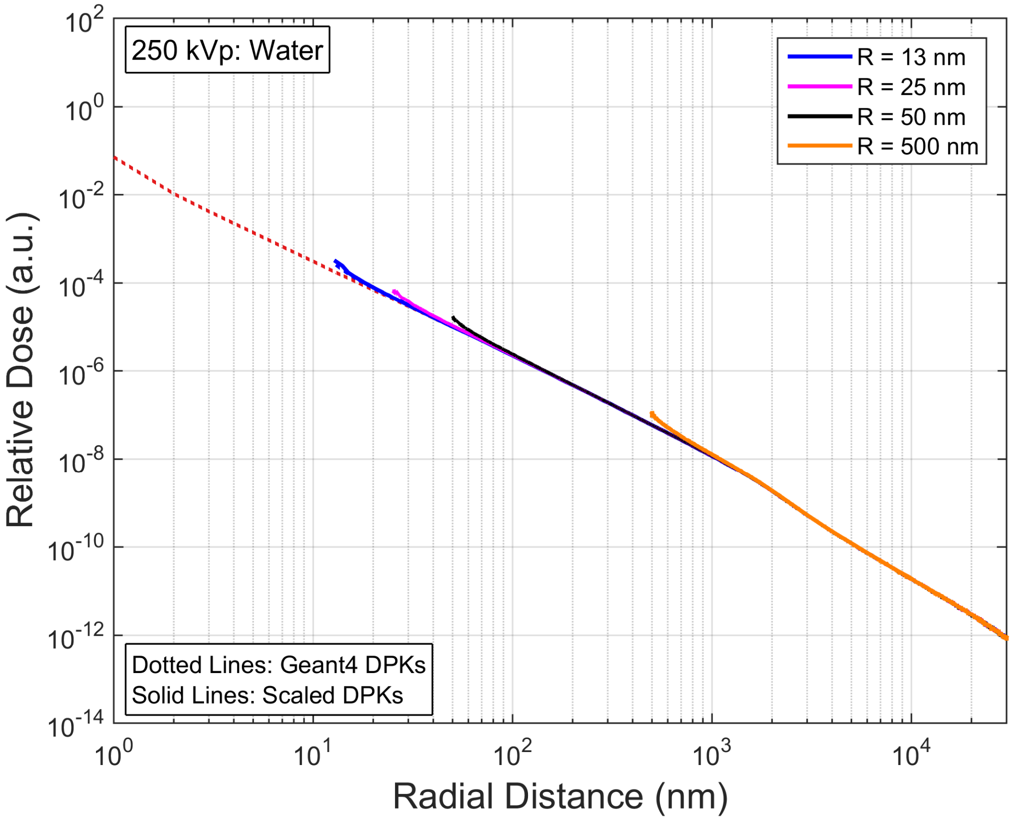

Figure 4.5.2 Volumetric scaling of DPK for WNPs of various dimensions for the 250 kVp source. The red dotted line denotes the DPK that was used as the basis for scaling.

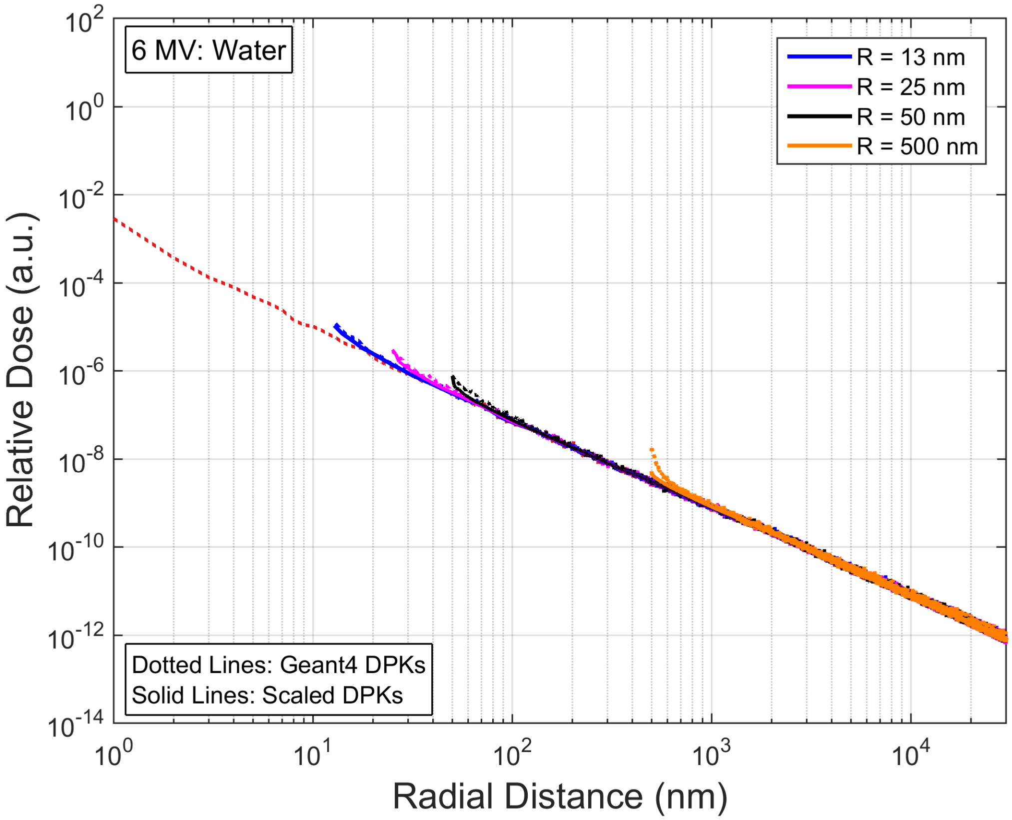

Figure 4.5.3 Volumetric scaling of DPK for WNPs of various dimensions for the 6 MV source. The red dotted line denotes the DPK that was used as the basis for scaling.

4.5.4 Scaling for Gold Dose-Point Kernels

In the case of dimensional GNPs, material scaling would presumably be required in addition to volumetric scaling. Therefore, the range-ratio was computed at the intensity-weighted average energy of the secondary electrons from gold for each photon spectrum (**Table 4.5.1**) and used to scale the DPKs according to the procedure described previously.

Table 4.5.1 Range ratios (water/gold) based on the average energy of secondary electrons originating from gold for each photon spectrum (Yb-169, 250 kVp, and 6 MV).

Photon Spectrum	Average Energy of Secondary Electrons (keV)	CSDA Range Ratio#
Yb-169	17.5	7.10
250 kVp	16.6	7.03
6 MV	194	9.61

#Ratio of CSDA range in water to CSDA range in gold

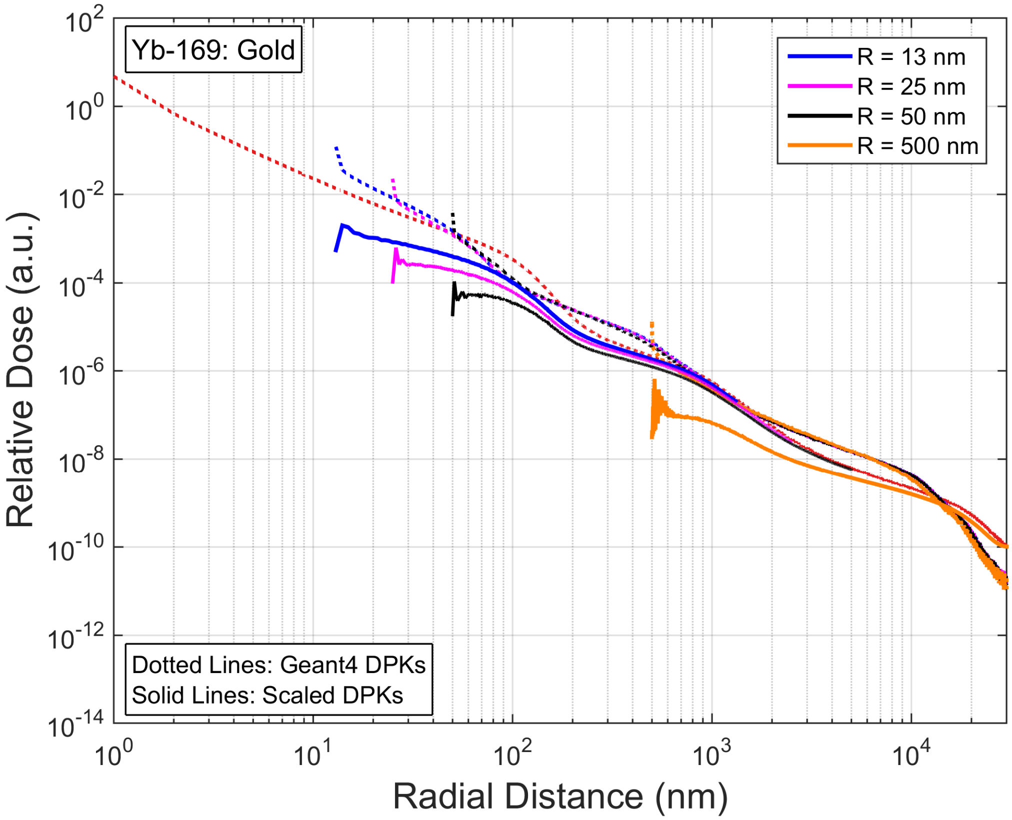

Figure 4.5.4 Range-ratio and volumetric scaling of DPK for GNPs of various dimensions for the Yb-169 source. The red dotted line denotes the DPK that was used as the basis for scaling.

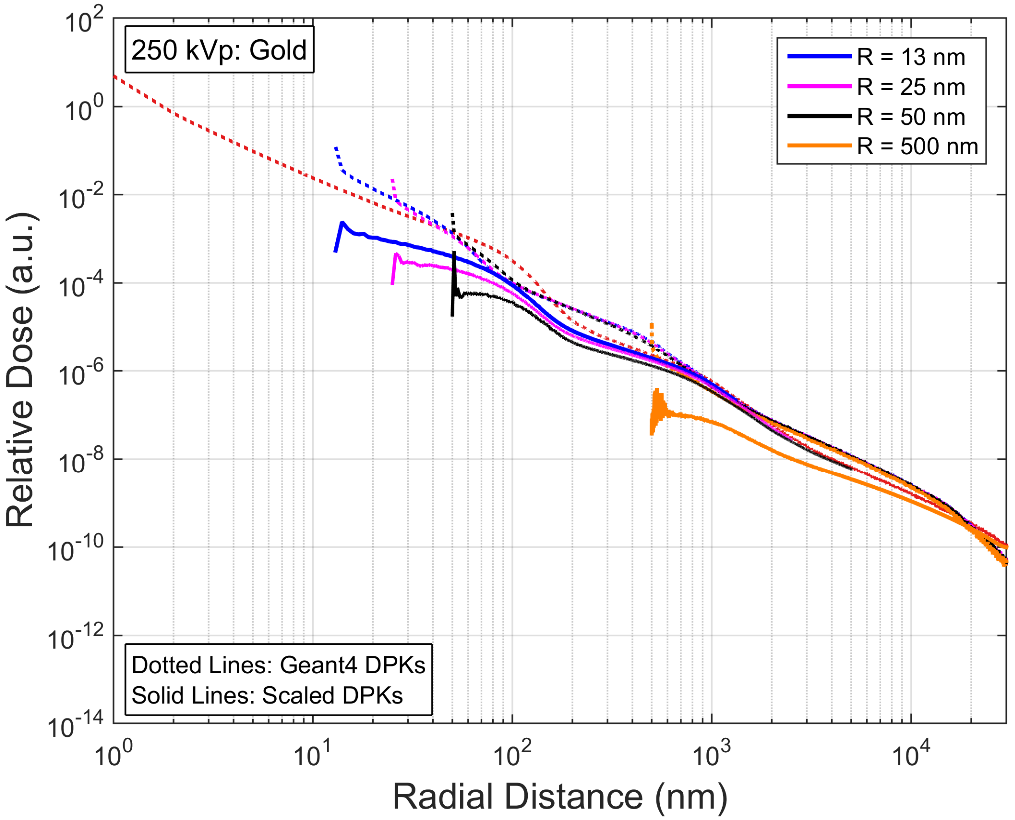

Figure 4.5.5 Range-ratio and volumetric scaling of DPK for GNPs of various dimensions for the 250 kVp source. The red dotted line denotes the DPK that was used as the basis for scaling.

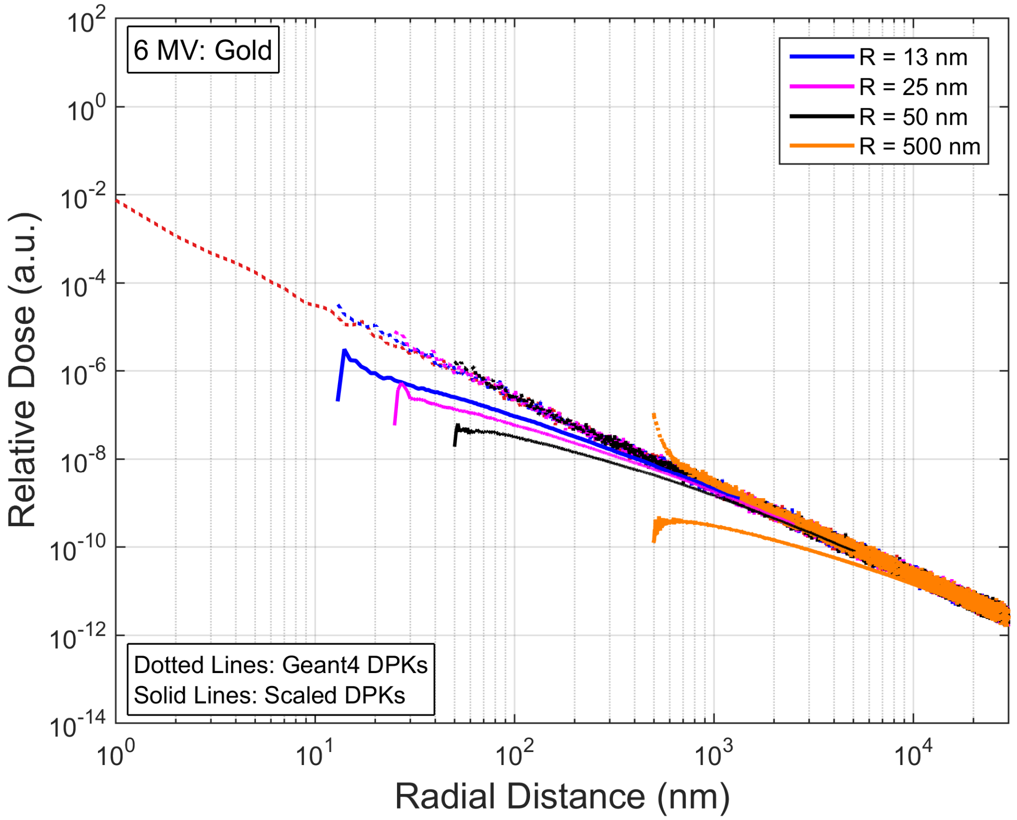

Figure 4.5.6 Range-ratio and volumetric scaling of DPK for GNPs of various dimensions for the 6 MV source. The red dotted line denotes the DPK that was used as the basis for scaling.

The range-ratio scaling method resulted in severe underestimation of the dose for the dimensional GNPs when compared to the Geant4 simulations. Therefore, this prompted an intuitively unrealistic, but still worthwhile, investigation wherein only the volumetric scaling was applied for scaling the gold DPKs. In this case, the results were more similar.

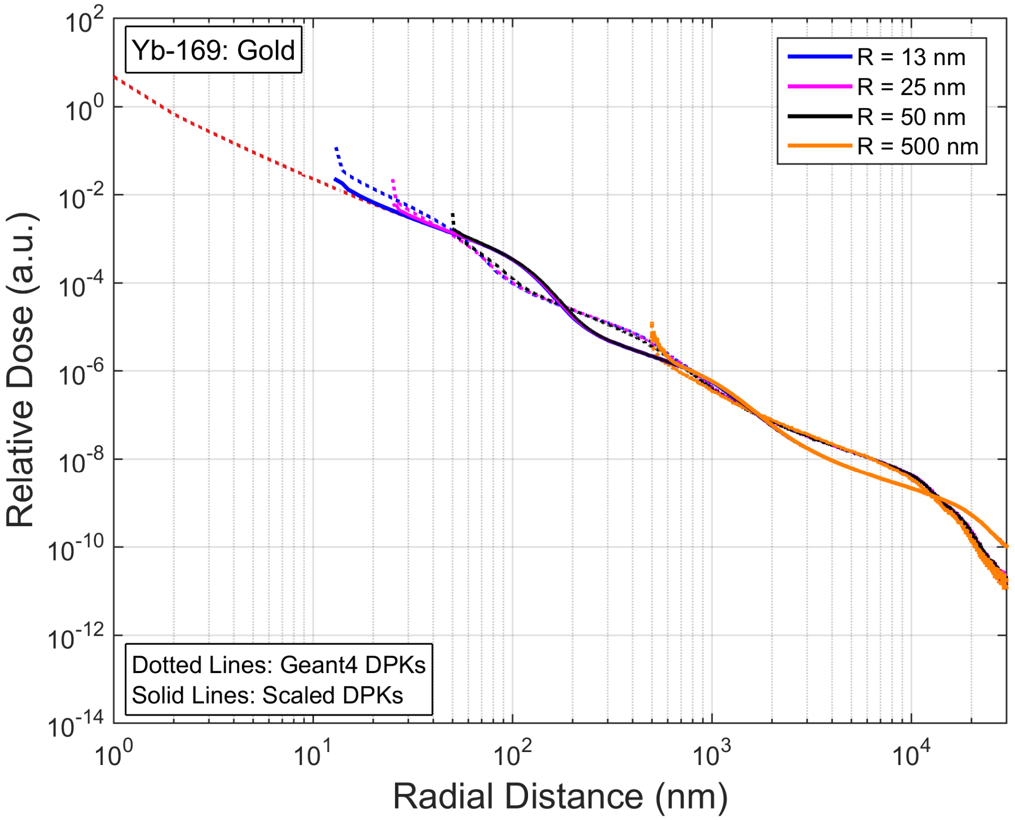

Figure 4.5.7 Volumetric scaling of DPK for GNPs of various dimensions for the Yb-169 source. The red dotted line denotes the DPK that was used as the basis for scaling.

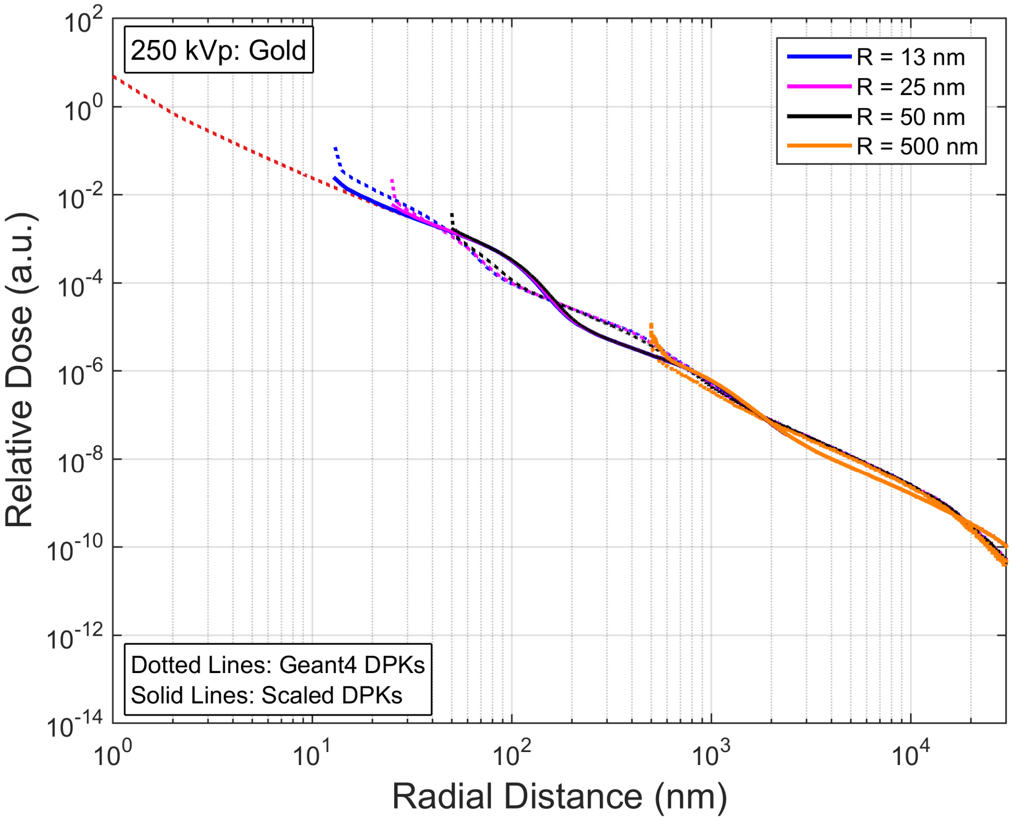

Figure 4.5.8 Volumetric scaling of DPK for GNPs of various dimensions for the 250 kVp source. The red dotted line denotes the DPK that was used as the basis for scaling.

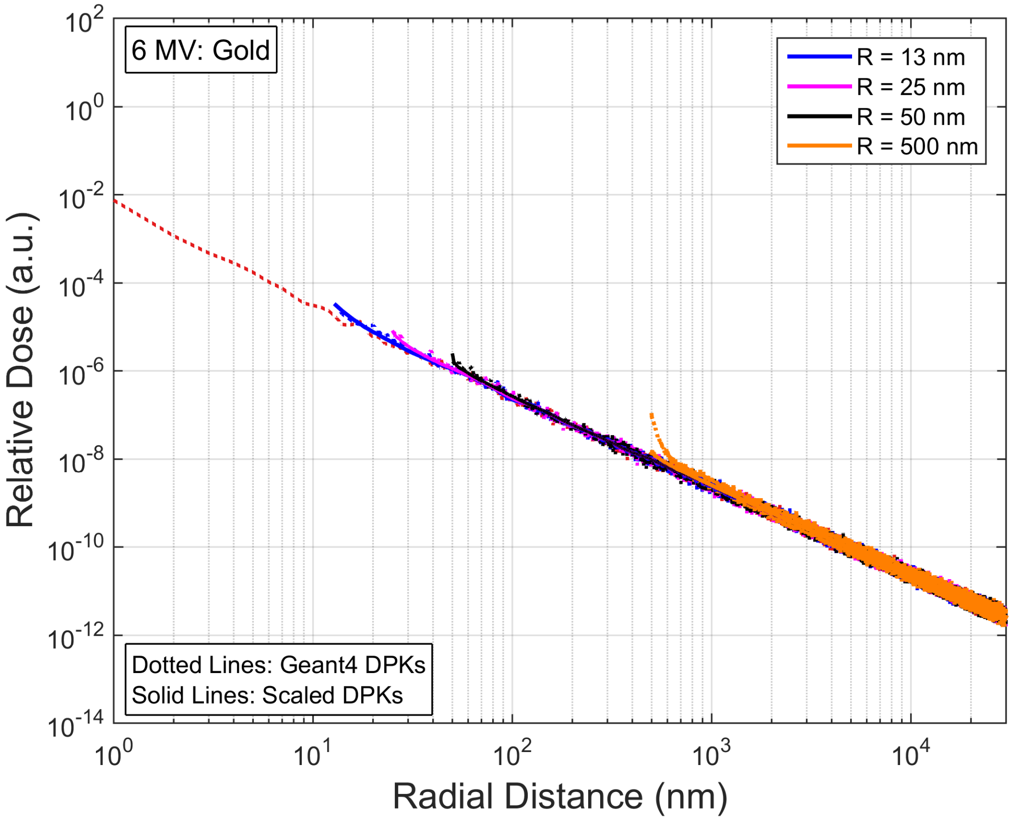

Figure 4.5.9 Volumetric scaling of DPK for GNPs of various dimensions for the 6 MV source. The red dotted line denotes the DPK that was used as the basis for scaling.

4.6 Calculation of Intracellular Dose Enhancement

Based on the fact that just volumetric scaling (and not both volumetric and range-ratio scaling) of the gold DPKs resulted in the best agreement with the dimensional dose kernels, it was adopted as the scaling method of choice for subsequent calculations of dose enhancement for a cellular image.

A 15 μm × 27 μm 2D transmission electron microscopy (TEM) image of a cell with a GNP-filled endosome located ~5 μm from the cell nucleus for 2D dose calculations (**Figure 4.6.1**) was used as the basis for the calculations. The endosome contained approximately 10,000 conjugated gold nanorods (GNRs) with dimensions of 13 nm diameter and 44 nm length. Intracellular dose calculation was performed for the Yb-169, 250 kVp, and 6 MV photon sources using an enhanced version of the calculation procedure described in a previous study [52]. Each pixel (50 nm × 50 nm) in the image was flagged as either containing gold or water using thresholding. For every pixel, the dose contribution to every other pixel was computed using volumetric scaling and ray tracing algorithms in synergy with the DPKs. The dose enhancement factors were overlaid on the TEM image in the form of contour lines (**Figure 4.6.2**). The dose enhancement factors represent the increase in dose conferred by the presence of gold. For example, a 200% increase is denoted by a dose enhancement factor of 3. For the Yb-169 and 250 kVp cases, the dose enhancement to the nucleus ranged from approximately 1.05 (5% increase) to 2 (100% increase) while for the 6 MV source, it ranged from 1.03 (3% increase) to 1.4 (40% increase).

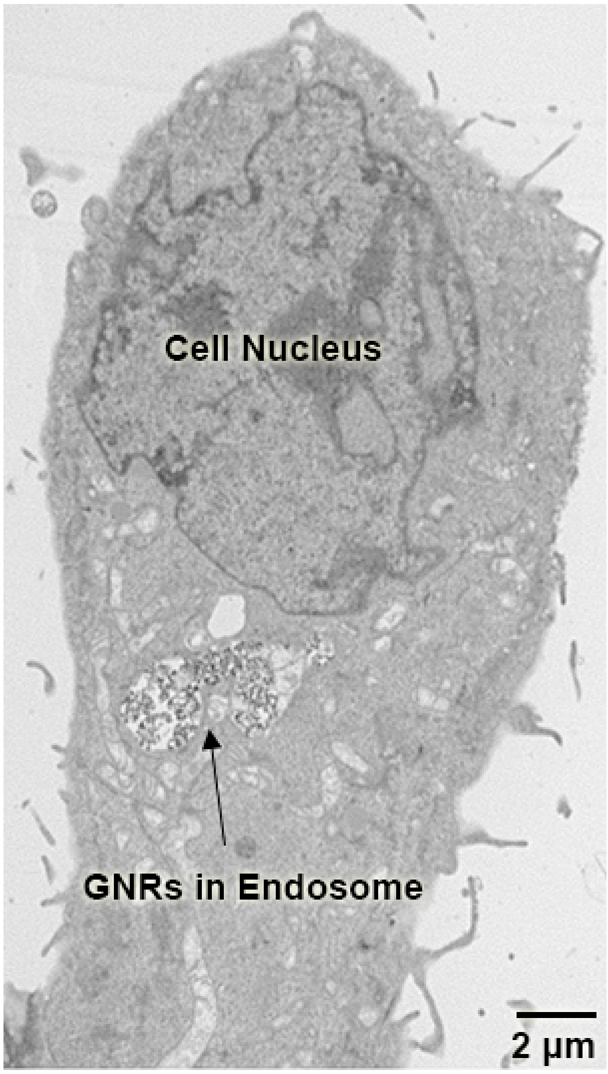

Figure 4.6.1 TEM image of cell, with endosome containing conjugated GNRs, used as the basis for microscopic dose enhancement calculations.

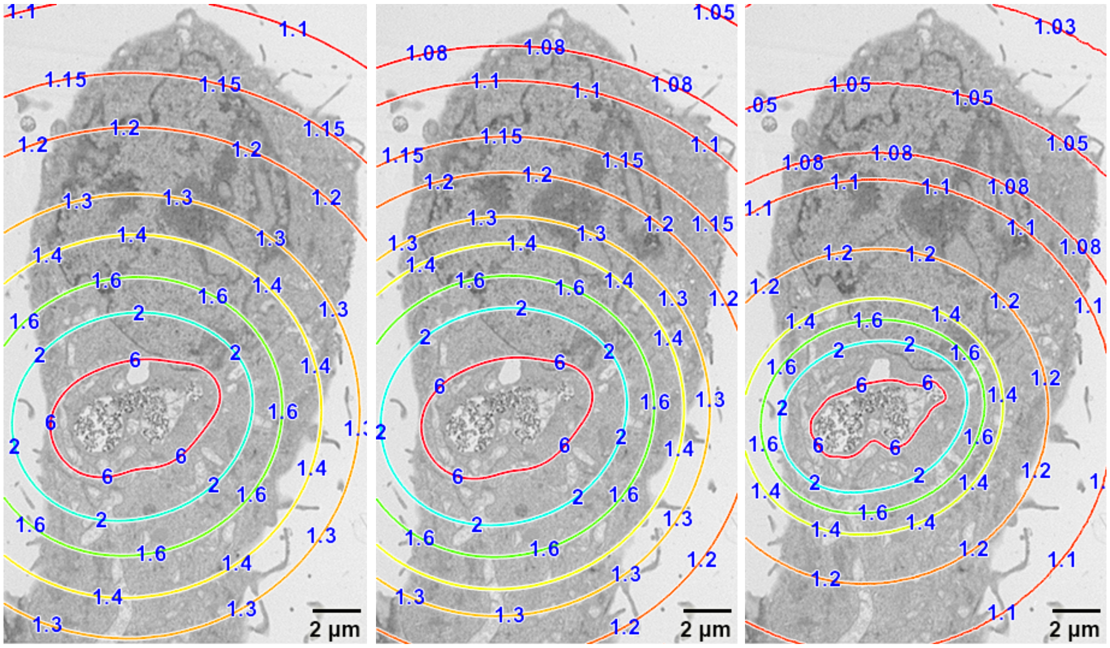

Figure 4.6.2 TEM image of cell overlaid with dose-enhancement contour lines for each photon source. (left) Yb-169. (middle) 250 kVp. (right) 6 MV. Dose enhancement is specified as a ratio here where 1 represents no enhancement.

More quantitative observations about the physical dose enhancement to the nucleus can be made from a cumulative dose-enhancement-area histogram plot (**Figure 4.6.3**). The histogram shows that irradiation using a Yb-169 photon source would result in the highest dose enhancement over the largest area of the cell nucleus, followed by 250 kVp, and finally the 6 MV source.

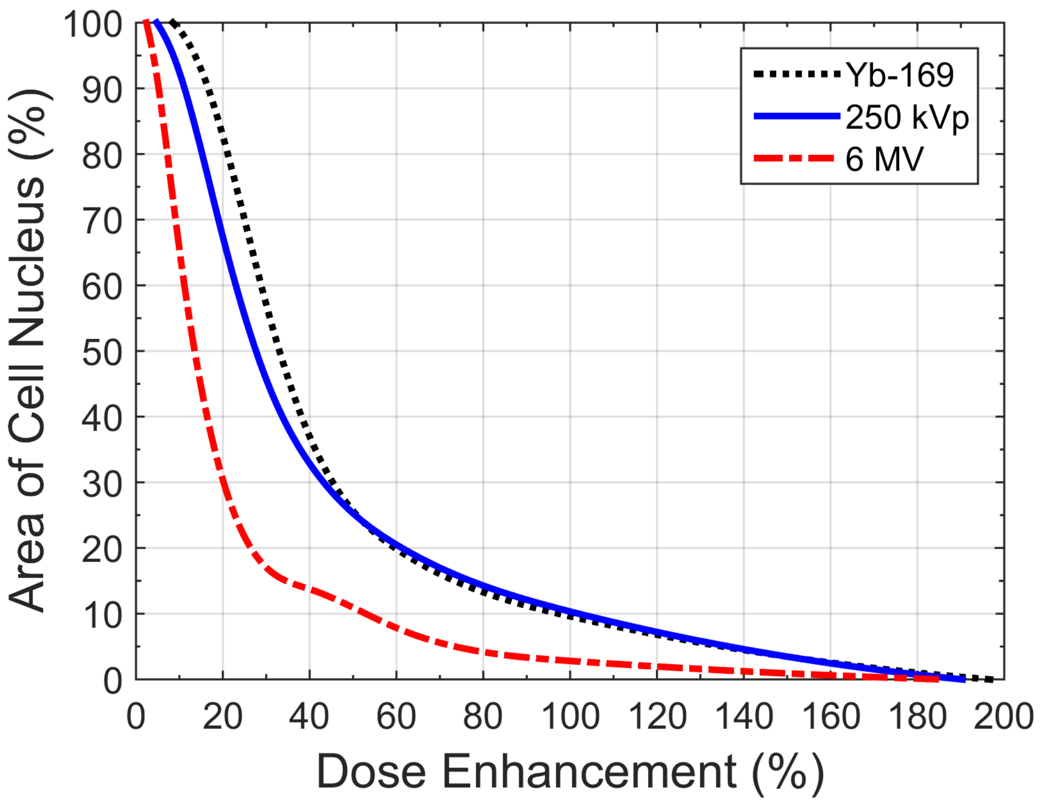

Figure 4.6.3 Dose-enhancement-area histogram for the cell nucleus for Yb-169, 250 kVp, and 6 MV irradiation. The dose enhancement is specified as a percentage here where 0% corresponds to a dose enhancement ratio of 1 (i.e., no enhancement) and 200% corresponds to a dose enhancement ratio of 3 (i.e., 200% increase).

4.7 Discussion

Generation of dimensional dose kernels for gold with Geant4 and subsequent attempts at developing methods to scale gold DPKs to match them revealed a somewhat counterintuitive outcome. While the range-ratio scaling method has been used and validated by several studies [61, 62], it did not work very well for the current situations. In fact, applying only the volumetric scaling to the gold DPKs resulted in a better match with the dimensional gold dose kernels from Geant4. The disparity could be due to the way Geant4 handled the combination of condensed history inside the GNP region and detailed history for the water region. Until low-energy cross sections become available for gold in the Geant4-DNA physics list, this issue may remain unresolved. Another reason for the disparity could be due to bremsstrahlung production in the GNP, which has been partly attributed to the increasing inaccuracy of the range-scaling method with increasing Z [62]. Also, the concept of using the CSDA range ratios for scaling might not be applicable to nanoscopic dimensions as the CSDA ranges for the energies investigated in this study were several orders of magnitude larger than the dimensions of the nanoparticles. Future work must investigate this disparity further, as the range-ratio scaling method has been found by other researchers to be a mostly accurate method, albeit for more macroscopic situations. Alternative solutions could include using the ratio of energy deposition inside and outside GNPs as a function of size to scale the DPKs or taking into account the decrease in electron energies as they traverse matter. However, these solutions would necessitate more convoluted approaches to model and to validate.

Nevertheless, for the time being, by consistently applying the computationally-derived DPKs based on physical principles to biological models, GNP-mediated radiosensitization can be quantified in at least a relative or qualitative fashion. For example, in this work, DPKs from Geant4 were scaled and then applied to a cellular TEM image for three different photon sources (Yb-169, 250 kVp, and 6 MV). The results suggested that while the lower energy sources can be more effective at dose enhancement than higher energy sources, comparable (same order of magnitude) dose enhancement can be seen even with higher energy sources despite the fact that higher energy photons interact primarily through Compton scattering, rather than the photoelectric effect, and therefore are not as efficient at producing secondary electrons in gold. While the overall fluence of low energy secondary electrons is much larger for the Yb-169 and 250 kVp sources, the range of such secondary electrons are shorter than for 6 MV photons and the dose is much more localized. Therefore, it can be concluded that the microscopic localization and/or distribution of radiosensitizers such as GNPs in and around tumor cells can have a remarkable effect on the radiosensitization that can be achieved, in conjunction with photon sources of appropriate energies.

CHAPTER 5
CONCLUSIONS

In the first task, MC and experimental investigations of a benchtop polychromatic cone-beam *K*-shell XFCT system were performed. An accurate and validated MC model was created and used to investigate several aspects of the system pertaining to optimization of the incident x-ray spectra in the context of improving XRF production/detection while considering the interplay between signal-to-dose ratio and scan time. The results prompted the retrofitting of a high-power x-ray source and the subsequent selection of a more optimized incident x-ray spectrum. The upgrade resulted in a lowering of the detection limit of GNPs to 2 mg/cm^3 (0.2 wt. %) while meeting realistic constraints on scan time, with the ability to go even lower with further optimization. Also, the MC model was used to elucidate the difficulty of performing simultaneous micro-CT and XFCT. Overall, the current MC model will greatly facilitate the further development of a benchtop XFCT system (e.g., implementation of array detectors/transmission detector, and optimization of other parameters) for routine pre-clinical molecular imaging applications. This work suggests that the use of XFCT for routine preclinical *ex vivo* or even *in vivo* imaging using GNPs (and other high-*Z* probes) is not only possible, but also practical.

The second task demonstrated the ability to simultaneously determine the spatial distribution and the local concentration of GNPs within sub-centimeter-sized biological samples using an *L*-shell XRF imaging technique implemented with a benchtop polychromatic source. Once feasibility was determined, the implementation of a high-power x-ray source and more advanced detector allowed the detection limit of GNPs to be lowered to the 0.005-0.007 mg/cm^3 (5-7 ppm range), rivaling that of synchrotron-based XRF imaging, while increasing the throughput of the system due to a reduction in scan time. These advances could allow *L*-shell XRF-based imaging to become a simple yet powerful imaging tool for the quantification and localization of GNPs as well as other probes presented within small biological samples such as *ex vivo* tissues and superficial tumors during preclinical small animal studies.

While either method is likely not capable of truly nanoscopic imaging resolution, they can still help reconcile the physical mechanisms of intratumoral dose enhancement with observed biological outcomes by understanding the dose enhancement characteristics from the bottom-up. Therefore, the third task involved computational investigations of nanoscopic dose enhancement. Starting with nanoscopic dose kernel computations for both point-source and dimensional nanoparticles, scaling methods were developed to elucidate dose enhancement characteristics on a nanoscale around GNPs. The methodology was then applied to a TEM image of a cell containing GNPs to estimate the dose enhancement within it. Although experimental confirmation at such small scales does not exist yet and the scaling methods developed were not exhaustively established, consistent and physically-sensible applications of computational models can allow relative comparisons of the biological outcomes from GNP-mediated dose enhancement.

Future research direction would include *ex vivo* or in *vivo* small animal imaging studies with the benchtop *K*-shell XFCT system to establish its feasibility and usefulness as a preclinical molecular imaging tool for GNPs and other high-*Z* probes. Also, the integration of micro-CT capability into the system can be explored experimentally.

Similar studies can be performed with the benchtop *L*-shell XRF system for superficial tumor imaging *in vivo* or for high-resolution, high-sensitivity *ex vivo* imaging of tissue samples from other GNRT studies. Where possible, the quantification capabilities of both modalities can be validated and benchmarked against established methods. The computational work and DPK scaling method can be further refined to investigate the applicability of the conventional range-ratio scaling method to nanoscopic circumstances, and to be able to predict dose distributions in even more heterogeneous media or with various other radiation sources; this would make the methodology more general and applicable to a wider variety of situations. Ultimately, the methods developed herein would greatly aid the understanding and further development of preclinical studies of GNRT.

REFERENCES

[1] W. M. Roberts, "Estimation of strontium in animal bone using x-ray fluorescence analysis," *Nature,* vol. 183, pp. 887-8, 1959.

[2] G. V. Alexander, "An x-ray fluorescence method for the determination of calcium, potassium, chlorine, sulfur, and phosphorus in biological tissues," *Analytical Chemistry,* vol. 37, pp. 1670-4, 1965.

[3] T. Hall, "X-ray fluorescence analysis in biology," *Science,* vol. 134, pp. 449-55, 1961.

[4] R. Mello, H. Callisen, J. Winter, A. Kagan, and A. Norman, "Radiation dose enhancement in tumors with iodine," *Medical Physics,* vol. 10, p. 75, 1983.

[5] K. Iwamoto, S. Cochran, J. Winter, E. Holburt, R. Higashida, and A. Norman, "Radiation dose enhancement therapy with iodine in rabbit VX-2 brain tumors," *Radiotherapy and Oncology,* vol. 8, pp. 161-170, 1987.

[6] A. Mesa, A. Norman, T. Solberg, J. Demarco, and J. Smathers, "Dose distributions using kilovoltage x-rays and dose enhancement from iodine contrast agents," *Physics in Medicine and Biology,* vol. 44, p. 1955, 1999.

[7] J. Robar, S. Riccio, and M. Martin, "Tumour dose enhancement using modified megavoltage photon beams and contrast media," *Physics in Medicine and Biology,* vol. 47, p. 2433, 2002.

[8] H. Maeda, J. Fang, T. Inutsuka, and Y. Kitamoto, "Vascular permeability enhancement in solid tumor: various factors, mechanisms involved and its implications," *International Immunopharmacology,* vol. 3, pp. 319-28, 2003.

[9] D. Regulla, L. Hieber, and M. Seidenbusch, "Physical and biological interface dose effects in tissue due to x-ray-induced release of secondary radiation from metallic gold surfaces," *Radiation Research,* vol. 150, pp. 92-100, 1998.

[10] L. R. Hirsch, R. J. Stafford, J. A. Bankson, S. R. Sershen, B. Rivera, R. E. Price, *et al.*, "Nanoshell-mediated near-infrared thermal therapy of tumors under magnetic resonance guidance," *Proceedings of the National Academy of Sciences of the United States of America,* vol. 100, pp. 13549-54, 2003.

[11] K. Sokolov, M. Follen, J. Aaron, I. Pavlova, A. Malpica, R. Lotan, *et al.*, "Real-time vital optical imaging of precancer using anti-epidermal growth factor receptor antibodies conjugated to gold nanoparticles," *Cancer Research,* vol. 63, p. 1999, 2003.

[12] G. F. Paciotti, L. Myer, D. Weinreich, D. Goia, N. Pavel, R. E. McLaughlin*, et al.*, "Colloidal gold: a novel nanoparticle vector for tumor directed drug delivery," *Drug Delivery,* vol. 11, pp. 169-83, 2004.

[13] S. H. Cho, "Estimation of tumour dose enhancement due to gold nanoparticles during typical radiation treatments: a preliminary Monte Carlo study," *Physics in Medicine and Biology,* vol. 50, pp. N163-73, 2005.

[14] J. F. Hainfeld, D. N. Slatkin, and H. M. Smilowitz, "The use of gold nanoparticles to enhance radiotherapy in mice," *Physics in Medicine and Biology,* vol. 49, pp. N309-15, 2004.

[15] J. F. Hainfeld, F. A. Dilmanian, D. N. Slatkin, and H. M. Smilowitz, "Radiotherapy enhancement with gold nanoparticles," *Journal of Pharmacy and Pharmacology,* vol. 60, pp. 977-85, 2008.

[16] S. H. Cho, B. L. Jones, and S. Krishnan, "The dosimetric feasibility of gold nanoparticle-aided radiation therapy (GNRT) via brachytherapy using low-energy gamma-/x-ray sources," *Physics in Medicine and Biology,* vol. 54, pp. 4889-905, 2009.

[17] L. H. Nie, S. Sanchez, K. Newton, L. Grodzins, R. O. Cleveland, and M. G. Weisskopf, "In vivo quantification of lead in bone with a portable x-ray fluorescence system—methodology and feasibility," *Physics in Medicine and Biology,* vol. 56, p. N39, 2011.

[18] M. Estevam and C. R. Appoloni, "Use of portable x-ray fluorescence (PXRF) in vivo as an alternative technique for the assessment of iron levels in patients with thalassemia and hemochromatosis," *Health Physics,* vol. 104, pp. 132-8, 2013.

[19] H. Matsukiyo, M. Watanabe, E. Sato, A. Osawa, T. Enomoto, J. Nagao*, et al.*, "X-ray fluorescence camera for imaging of iodine media in vivo," *Radiological Physics and Technology,* vol. 2, pp. 46-53, 2009.

[20] P. Boisseau, "Determination of three dimensional trace element distributions by the use of monochromatic x-ray microbeams," ed. Massachusetts Institute of Technology: PhD Dissertation, 1986.

[21] T. Takeda, K. Ito, K. Kishi, T. Maeda, T. Yuasa, J. Wu*, et al.*, "Preliminary experiment of the fluorescent X-ray computed tomography with synchrotron radiation," *Japanese Journal of Medical Imaging Technology,* vol. 12, pp. 537-538, 1994.

[22] R. Cesareo and S. Mascarenhas, "A new tomographic device based on the detection of fluorescent x-rays," *Nuclear Instruments and Methods in Physics Research Section A,* vol. 277, pp. 669-672, 1989.

[23] J. P. Hogan, R. A. Gonsalves, and A. S. Krieger, "Fluorescent computer tomography: a model for correction of x-ray absorption," *IEEE Transactions on Nuclear Science,* vol. 38, pp. 1721-1727, 1991.

[24] T. Yuasa, M. Akiba, T. Takeda, M. Kazama, A. Hoshino, Y. Watanabe*, et al.*, "Reconstruction method for fluorescent x-ray computed tomography by least-squares method using singular value decomposition," *IEEE Transactions on Nuclear Science,* vol. 44, pp. 54-62, 1997.

[25] A. Simionovici, M. Chukalina, C. Schroer, M. Drakopoulos, A. Snigirev, I. Snigireva*, et al.*, "High-resolution x-ray fluorescence microtomography of homogeneous samples," *IEEE Transactions on Nuclear Science,* vol. 47, pp. 2736-2740, 2000.

[26] C. Schroer, "Reconstructing x-ray fluorescence microtomograms," *Applied Physics Letters,* vol. 79, pp. 1912-1914, 2001.

[27] P. J. La Rivière, "Approximate analytic reconstruction in x-ray fluorescence computed tomography," *Physics in Medicine and Biology,* vol. 49, p. 2391, 2004.

[28] G. F. Rust and J. Weigelt, "X-ray fluorescent computer tomography with synchrotron radiation," *IEEE Transactions on Nuclear Science,* vol. 45, pp. 75-88, 2005.

[29] S. K. Cheong, B. L. Jones, A. K. Siddiqi, F. Liu, N. Manohar, and S. H. Cho, "X-ray fluorescence computed tomography (XFCT) imaging of gold nanoparticle-loaded objects using 110 kVp x-rays," *Physics in Medicine and Biology,* vol. 55, pp. 647-62, 2010.

[30] B. L. Jones and S. H. Cho, "The feasibility of polychromatic cone-beam x-ray fluorescence computed tomography (XFCT) imaging of gold nanoparticle-loaded objects: a Monte Carlo study," *Physics in Medicine and Biology,* vol. 56, p. 3719, 2011.

[31] B. L. Jones, N. Manohar, F. Reynoso, A. Karellas, and S. H. Cho, "Experimental demonstration of benchtop x-ray fluorescence computed tomography (XFCT) of gold nanoparticle-loaded objects using lead- and tin-filtered polychromatic cone-beams," *Physics in Medicine and Biology,* vol. 57, pp. N457-67, 2012.

[32] M. Bazalova, Y. Kuang, G. Pratx, and L. Xing, "Investigation of x-ray fluorescence computed tomography (XFCT) and K-edge imaging," *IEEE Transactions on Medical Imaging,* vol. 31, pp. 1620-7, 2012.

[33] Y. Kuang, G. Pratx, M. Bazalova, B. Meng, J. Qian, and L. Xing, "First demonstration of multiplexed x-ray fluorescence computed tomography (XFCT) imaging," *IEEE Transactions on Medical Imaging,* vol. 32, pp. 262-7, 2013.

[34] Y. Kuang, G. Pratx, M. Bazalova, J. Qian, B. Meng, and L. Xing, "Development of XFCT imaging strategy for monitoring the spatial distribution of platinum-based chemodrugs: instrumentation and phantom validation," *Medical Physics,* vol. 40, p. 030701, 2013.

[35] L. Vincze, K. Janssen, and F. Adams, "A general Monte Carlo simulation of energy-dispersive X-ray fluorescence spectrometers—I: Unpolarized radiation, homogeneous samples," *Spectrochimica Acta Part B: Atomic Spectroscopy,* vol. 48, pp. 553-573, 1993.

[36] T. Schoonjans, L. Vincze, V. A. Solé, M. Sanchez del Rio, P. Brondeel, G. Silversmit*, et al.*, "A general Monte Carlo simulation of energy dispersive X-ray fluorescence spectrometers — Part 5: Polarized radiation, stratified samples, cascade effects, M-lines," *Spectrochimica Acta Part B: Atomic Spectroscopy,* vol. 70, pp. 10-23, 2012.

[37] G. Jost, S. Golfier, R. Lawaczeck, H. J. Weinmann, M. Gerlach, L. Cibik*, et al.*, "Imaging-therapy computed tomography with quasi-monochromatic x-rays," *European Journal of Radiology,* vol. 68, pp. S63-S68, 2008.

[38] K. Ricketts, A. Castoldi, C. Guazzoni, C. Ozkan, C. Christodoulou, A. P. Gibson*, et al.*, "A quantitative x-ray detection system for gold nanoparticle tumour biomarkers," *Physics in Medicine and Biology,* vol. 57, pp. 5543-55, 2012.

[39] N. Manohar, F. Reynoso, and S. H. Cho, "Feasibility of direct L-shell fluorescence imaging of gold nanoparticles using a benchtop x-ray source," *Medical Physics,* vol. 39, pp. 3987-3988, 2012.

[40] D. Wu, Y. Li, M. D. Wong, and H. Liu, "A method of measuring gold nanoparticle concentrations by x-ray fluorescence for biomedical applications," *Medical Physics,* vol. 40, pp. 051901-10, 2013.

[41] X-5 Monte Carlo Team, "MCNP - A General Purpose Monte Carlo N-Particle Transport Code, Version 5," *LA-UR-03-1987,* 2003.

[42] N. Manohar, "Effect of source x-ray energy spectra on the detection of fluorescence photons from gold nanoparticles," ed. Georgia Institute of Technology: MS Thesis, 2011.

[43] G. Jost, T. Mensing, S. Golfier, R. Lawaczeck, H. Pietsch, J. Hütter*, et al.*, "Photoelectric-enhanced radiation therapy with quasi-monochromatic computed tomography," *Medical Physics,* vol. 36, p. 2107, 2009.

[44] B. L. Jones, "Development of dosimetry and imaging techniques for pre-clinical studies of gold nanoparticle-aided radiation therapy," ed. Georgia Institute of Technology: PhD Dissertation, 2011.

[45] G. Poludniowski, G. Landry, F. DeBlois, P. M. Evans, and F. Verhaegen, "SpekCalc: a program to calculate photon spectra from tungsten anode x-ray tubes," *Physics in Medicine and Biology,* vol. 54, pp. N433-8, 2009.

[46] A. A. Michelson, *Studies in Optics*: U. of Chicago Press, 1927.

[47] F. Liu, "Monte Carlo modeling of an x-ray fluorescence detection system by the MCNP code," ed. Georgia Institute of Technology: MS Thesis, 2009.

[48] X. Qian, X. H. Peng, D. O. Ansari, Q. Yin-Goen, G. Z. Chen, D. M. Shin*, et al.*, "In vivo tumor targeting and spectroscopic detection with surface-enhanced Raman nanoparticle tags," *Nature Biotechnology,* vol. 26, pp. 83-90, 2008.

[49] P. M. Fong, D. C. Keil, M. D. Does, and J. C. Gore, "Polymer gels for magnetic resonance imaging of radiation dose distributions at normal room atmosphere," *Physics in Medicine and Biology,* vol. 46, pp. 3105-13, 2001.

[50] G. Andermann and J. W. Kemp, "Scattered x-rays as internal standards in x-ray emission spectroscopy," *Analytical Chemistry,* vol. 30, pp. 1306-1309, 1958.

[51] C. Bui, L. Confalonieri, and M. Milazzo, "Use of Compton scattering in quantitative XRF analysis of stained glass," *International Journal of Radiation Applications and Instrumentation. Part A, Applied Radiation and Isotopes,* vol. 40, pp. 375-380, 1989.

[52] B. L. Jones, S. Krishnan, and S. H. Cho, "Estimation of microscopic dose enhancement factor around gold nanoparticles by Monte Carlo calculations," *Medical Physics,* vol. 37, pp. 3809-16, 2010.

[53] I. Kawrakow and D. Rogers, "The EGSnrc code system," *NRCC Report PIRS-701,* 2003.

[54] B. L. Jones, "Monte Carlo calculations of microscopic dose enhancement for gold nanoparticle-aided radiation therapy," ed. Georgia Institute of Technology: MS Thesis, 2009.

[55] F. J. Reynoso, "Design of an ytterbium-169 brachytherapy source for gold nanoparticle-aided radiotherapy," ed. Georgia Institute of Technology: PhD Dissertation, 2014.

[56] V. Semenenko, J. Turner, and T. Borak, "NOREC, a Monte Carlo code for simulating electron tracks in liquid water," *Radiation and Environmental Biophysics,* vol. 42, pp. 213-217, 2003.

[57] M. J. Berger, "Distribution of absorbed dose around point sources of electrons and beta particles in water and other media," *Journal of Nuclear Medicine,* pp. Suppl 5:5-23, 1971.

[58] S. Agostinelli, J. Allison, K. Amako, J. Apostolakis, H. Araujo, P. Arce*, et al.*, "Geant4—a simulation toolkit," *Nuclear Instruments and Methods in Physics Research Section A: Accelerators, Spectrometers, Detectors and Associated Equipment,* vol. 506, pp. 250-303, 2003.

[59] S. Incerti, A. Ivanchenko, M. Karamitros, A. Mantero, P. Moretto, H. N. Tran*, et al.*, "Comparison of GEANT4 very low energy cross section models with experimental data in water," *Medical Physics,* vol. 37, pp. 4692-708, 2010.

[60] M. Berger, "Improved point kernels for electron and beta-ray dosimetry," *Report NBSIR,* pp. 73-107, 1973.

[61] D. E. Charlton, "Energy dissipation near an interface: a more realistic approach to electron range and stopping power," *Radiation Research,* vol. 44, pp. 575-93, 1970.

[62] S. H. Cho, W. D. Reece, and C.-H. Kim, "Validity of two simple rescaling methods for electron/beta dose point kernels in heterogeneous source–target geometry," *Radiation Physics and Chemistry,* vol. 69, pp. 265-272, 2004.

[63] M. J. Berger, J. S. Coursey, M. A. Zucker, and J. Chang. (2010, Dec.). *Stopping-Power and Range Tables for Electrons, Protons, and Helium Ions*. Available: http://www.nist.gov/pml/data/star/